THESIS FOR THE DEGREE OF DOCTOR OF PHILOSOPHY

Near Atomic Scale Analysis of Biomaterials and Proteins

GUSTAV ERIKSSON

Department of Chemistry and Chemical Engineering

CHALMERS UNIVERSITY OF TECHNOLOGY

Gothenburg, Sweden 2024

Near Atomic Scale Analysis of Biomaterials and Proteins
GUSTAV ERIKSSON
ISBN 978-91-8103-125-6

Acknowledgements, dedications, and similar personal statements in this thesis, reflect the author's own views.

© GUSTAV ERIKSSON, 2024.

Doktorsavhandlingar vid Chalmers tekniska högskola
Ny serie nr 5583
ISSN 0346-718X

Department of Chemistry and Chemical Engineering
Chalmers University of Technology
SE-412 96 Gothenburg
Sweden
Telephone + 46 (0)31-772 1000

Cover:
An illustration of a bone integrating biomaterial and proteins together with 3D reconstructions of atom probe tomography data. Data to the right shows the interface between hydroxyapatite nanoparticles, embedded in chromium, and titanium (top), as well as a green fluorescent protein embedded in silica (bottom).

Chalmers Digitaltryck
Gothenburg, Sweden 2024

Near Atomic Scale Analysis of Biomaterials and Proteins
GUSTAV ERIKSSON
Department of Chemistry and Chemical Engineering
Chalmers University of Technology

Abstract

Modern analytical techniques have greatly advanced our understanding of the smallest building blocks of materials and biological systems. In materials science, the structure and composition at the nanoscale directly influence a material's properties, while in biology, the three-dimensional structure of proteins is intimately tied to their function. Biomaterials, designed to interact with biological systems, have significantly contributed to healthcare and improved quality of life by aiding in the treatment of diseases and alleviating injuries. The 3D structure of proteins is key to their function, and to determine this structure is essential for developing therapeutics that address current healthcare challenges.

The structure of biomaterials, as well as proteins at the atomic scale, is crucial to their functionality, necessitating analysis at this size level. This thesis explores the use of Atom Probe Tomography (APT) for various biomaterials used in medical devices as well as protein structures. APT is a powerful characterization technique employed in various domains of materials science, providing near-atomic-resolution analysis of the chemical composition of materials in 3D with high sensitivity.

Biomaterials are often used in medical devices for therapeutic purposes. Despite their success, challenges remain, including difficulties in integrating with the body, hard-to-treat bacterial infections, and mechanical failures. Different design strategies for implantable biomaterials were studied to improve integration with bone, antibacterial properties, and mechanical performance. These materials are analysed using correlative electron microscopy and APT to investigate their microstructures and how these affect the desired material properties.

To study proteins using APT, they must be embedded in a matrix that can withstand the conditions required for analysis while retaining the molecules in their native state. Silica synthesized via a sol-gel process is one such material and is studied in this work. Proteins embedded in silica, either directly in solution or after adsorption to a nanostructured surface, allow for specimen preparation for nanoscale analysis from the obtained material. By utilizing new atom probe instrumentation, where atoms are field evaporated by a deep-UV laser, isotope-labelled proteins are unambiguously detected and studied in quantities previously unattained by APT.

Keywords: Biomaterials, Implanted devices, Nanomaterials, Structural Biology, Proteins, Silica Embedding, Electron Microscopy, Laser Assisted Atom Probe Tomography

Included works

The thesis is based on the work contained in the following papers, referred to by Roman numerals in the text.

I. **Atomically Resolved Interfacial Analysis of Bone-Like Hydroxyapatite Nanoparticles on Titanium**
Gustav Eriksson, Mats Hulander, Mattias Thuvander, Martin Andersson
Published in Advanced NanoBiomed Research. 2023;3(10): 2300051.

II. **Photothermal Properties of Supported Gold Nanorods**
Maja Uusitalo, Michal Strach, Gustav Eriksson, Tetiana Dmytrenko, John Andersson, Andreas Dahlin, Mats Hulander, Martin Andersson
Published in Nano Letters. 2024;24(40): 12529-12535.

III. **Oxidation of a Zirconium Nitride Multilayer Covered Knee Implant after Two Years in Clinical Use**
Julia S. Rau, Gustav Eriksson, Per Malmberg, Ana Laura Puente Reyna, Jens Schwiesau, Martin Andersson, Mattias Thuvander
Accepted in Acta Biomaterialia.

IV. **Silica-embedded Gold Nanoparticles Analyzed by Atom Probe Tomography**
Gustav Eriksson, Mats Hulander, Mattias Thuvander, Martin Andersson
Published in Microscopy and Microanalysis. 2024: ozae024.

V. **Silica Analysis using Deep-UV Laser Assisted Atom Probe Tomography**
Gustav Eriksson, Mats Hulander, Mattias Thuvander, Martin Andersson
Manuscript in preparation.

VI. **Evaporation of cations from non-conductive nano-samples using single cycle THz pulses: an experimental and theoretical study**
Matteo De Tullio, Giovanni Novi Inverardi, Michella Karam, Jonathan Houard, Marc Ropitaux, Ivan Blum, Francesco Carnovale, Gianluca Lattanzi, Simone Taioli, Gustav Eriksson, Mats Hulander, Martin Andersson, Angela Vella, Tommaso Morresi
Manuscript to be submitted.

VII. **Enhanced Throughput and Near Atomically Resolved 3D Protein Structures Analysis using Atom Probe Tomography**
Gustav Eriksson, David Mayweg, Mats Hulander, Mattias Thuvander and Martin Andersson
Manuscript in preparation.

Contribution report

My contributions to the articles on which this thesis is based on are as follows:

I. Main author. Performed TEM and APT specimen preparation, measurements and data analysis. Wrote the first draft and was responsible for the manuscript.

II. Co-author. Did TEM imaging and analysis. Contributed to the related part of the manuscript.

III. Co-author. Did TEM imaging and analysis. Assisted with parts of APT analysis. Contributed to the related part of the manuscript.

IV. Main author. Performed all the sample synthesis, TEM and APT specimen preparation, measurements and data analysis. Wrote the first draft and was responsible for the manuscript.

V. Main author. Performed all the sample synthesis, APT specimen preparation, measurements and data analysis. Wrote the first draft and was responsible for the manuscript.

VI. Co-author. Performed silica sample synthesis. Wrote the related part of the manuscript.

VII. Main author. Performed all the sample synthesis, most of the APT specimen preparation, measurements and data analysis. Wrote the first draft and was responsible for the manuscript.

Contents

1. Introduction 1
1.1. Purpose and Objectives 2
2. Background 4
2.1. Biomaterials 4
2.2. Biomolecules 6
2.2.1. Basis and role of proteins 6
2.2.2. Structure and characterization of proteins 7
2.3 Nanoparticles 9
2.3.1. Nanoparticle surface interactions 11
2.3.2. Nanoparticle biological interactions 11
2.4. Characterization Techniques 12
2.4.1. Electron Microscopy 12
2.4.2. Atom Probe Tomography 17
2.5. Silica 23
2.5.1. Synthesis 23
2.5.2. Protein immobilization and encapsulation 24
3. Experimental Methods 25
3.1. Biomaterial specimen preparation and characterization 25
3.2. Silica synthesis and protein embedding 25
3.3. Silica embedding of nanostructured surfaces with proteins 28
3.4. Specimen preparation 30
3.5. Characterization 32
4. Results and Discussion 34
4.1. Biomaterial characterization 34

4.1.1. Interfacial analysis of nanoHA on titanium 34
4.1.2. Photothermal gold nanorods 37
4.1.3. Oxide formation on ZrN multilayered implant material 38
4.2. Silica embedded gold nanostructured surfaces 42
4.3. Deep-UV and THz laser assisted analysis of bulk silica 45
4.4. APT analysis of silica embedded proteins 53
5. Conclusions 57
5.1. Future perspectives 58
Acknowledgements 61
References 62

1. Introduction

Since the early days of civilization, different materials have been used to deal with injuries and illnesses. There are examples of various materials used to close large wounds and as replacement for teeth in early civilization using materials often, but not always, from biological sources [1]. While done without today's detailed understanding of how materials interact with living systems, this historical use demonstrates the drive to use whatever tools that were available to restore health and bodily functionality.

With advances in material sciences, increasingly sophisticated medical devices have been developed for use as implants. One example is prosthetic hip and knee replacements, which today represent some of the most common surgical procedures, a trend that is increasing with aging population and the prevalence of arthritis [2]. Such procedures are generally successful and contribute to improved quality of life for patients. However, in some cases, mechanical failure of the implant can occur, requiring revisional surgery to address. These procedures are associated with discomfort, health risks for the individual patient, and societal costs. Surgical insertion of implanted medical devices is also associated with risk of bacterial infections. As the implants are designed to interact favourably with the body, they can inadvertently also be a favourable environment for bacterial adhesion. Such bacterial infections can be hard to treat and have severe consequences. Current strategies for treating bacterial infections generally include the use of antibiotics, which have made remarkable contribution to human health and life quality since their introduction. However, they are less effective when bacterial biofilms have formed as a result of colonisation [3]. The use of antibiotics is also associated with development of resistance in bacteria, which is an emerging healthcare crisis [4]. There is therefore a need for new, antibacterial strategies based on other mechanisms for prevention and treatment of bacterial infections.

The biological systems themselves are of equal interest to the man-made materials that interact with them, both to further our understanding of how life works, but also to be able to treat and prevent various diseases. One of the most fundamental components of life is proteins, the biomolecules that perform most of the functions in all living cells and organisms. The structure of all proteins are primarily determined by the DNA sequence, genes, that code for each protein's specific amino acid sequence [5]. However, the function of a protein is dependent on how it folds into a three-dimensional structure, and this cannot always be easily inferred from its amino acid sequence. For this reason, the experimental determination of a protein's 3D structure has been a long withstand and major question in biology.

Proteins are involved in many diseases, either by errors in folding or as targets for viruses to attack cells. For this reason, understanding protein structures is key to

effective development of new pharmaceuticals to address current healthcare challenges. Several experimental methods have emerged in the last half century to provide insight into the 3D structure of proteins, namely X-ray diffraction, nuclear magnetic resonance, and most recently, cryo-electron microscopy. In the last few years, computational methods have also improved and contributed to the understanding of protein structures. Despite this, one large class of proteins that are elusive to study with these methods are membrane proteins, which are often identified as targets for pharmaceuticals. Furthermore, proteins are often dynamical, and their structure, as obtained by conventional methods, might not be representative for their structure in action when interacting with other compounds. There is therefore a need for new, complementary methods to study the 3D structure of proteins, especially those that can allow for studies of transmembrane proteins in realistic environments and protein interactions. Atom Probe Tomography has been proposed as a possible analytical technique that can contribute to understanding of proteins [6], owing to its ability to provide 3D mapping of materials with sub-nanometre spatial resolution [7][8]. However, challenges in preparation of suitable samples have yet to be fully overcome for the technique to contribute to the field of structural biology.

1.1. Purpose and Objectives

In the work on which this thesis is based, one of the overall objectives was to explore the use of high-resolution characterization techniques to study the structure of materials used for implants as well as the biological materials themselves. By investigating the structure of materials at the smallest scale, it can be related to the properties of the material and information of this type is valuable for the design of new materials where the desired properties are improved. For bone integrating medical devices, some properties of importance are compatibility and the ability for bone to integrate with the implant, the ability to prevent or manage with bacterial infections, and lowest possible risk of mechanical failure during the intended lifetime of the implant.

In the first three papers on which the thesis is based on, biomaterials intended for implanted medical devices are investigated. **Paper I** addresses a proposed material, where titanium is surface modified with nanostructured synthetic hydroxyapatite. The purpose of this modification is to obtain a bone-like implant surface, with the goal of speeding up the integration process. In **Paper II,** a strategy to introduce triggered antimicrobial functionality in implanted medical devices is explored. Gold nanorods with a specific shape and size are able to absorb light with wavelengths that pass through the body and heat up locally by electron plasmon resonance. It is proposed that by localized heating, bacteria at the implant surface could be killed after the implant has been introduced into a patient. In this paper, the structure of these nanorods and the mechanism of heating are studied. **Paper III** studies the formation of oxide by bio-corrosion and tribology on a zirconium implant after two years of use in a patient. Oxide

formation is one reason for mechanical failure of implanted medical devices and the consequential need for revision surgery. By comparing the oxide formed on the implant with that on a new material and a tested sample, it is possible to gain insight into designing implant materials with reduced risk of mechanical failure.

The other four papers in this thesis explore strategies to study some of the fundamental biomolecules in living organisms, namely proteins, using APT. In **Paper IV**, a previously developed concept of embedding proteins in a silica matrix to retain them in their native state while forming a solid material for APT analysis is further developed. To circumvent problems related to analysis of silica materials using APT due to their dielectric nature, a surface was nanostructured with gold nanoparticles and then embedded in a thin silica film. By this, a platform for the binding of proteins to the nanoparticles and embedding in a defined, smaller volume of silica, designed to avoid the challenges associated with studying bulk specimens of silica using APT.

The challenges of analysing a dielectric material such as silica using APT could also be tackled by changes to the APT instrumentation, specifically, the laser source used to trigger evaporation of ions from the specimen. In **Paper V**, the possibility of analysing silica material using state-of-the-art deep-UV laser assisted APT was explored.

Other laser sources and mechanisms for enabling APT measurements are also of interest, and **Paper VI** explores an experimental new instrumentation utilizing THz laser assisted APT to study the silica material.

In **Paper VII**, the study of silica embedded proteins using APT is enabled by isotopic labelling of the carbon in a protein. Green Fluorescent Proteins were expressed with ^{13}C and embedded in bulk silica, providing a material that, when analysed with deep-UV laser assisted APT, gave unambiguous data on the presence and distribution of the proteins in the sample. Within a single measurement, a large number of proteins could be detected. This opens the way for improved throughput of protein analysis using APT and paves the way for the development of methods to use the data to determine the 3D structure of proteins with higher resolution than previously possible.

2. Background

In this chapter, background information on the materials studied and motivation for using higher resolution microscopy methods are provided. Contemporary challenges regarding biomaterials used for implanted medical devices are presented, as well as proposed solutions, for which further understanding of material microstructure is essential will be introduced. The role, function, and structure of proteins along with the currently used characterization techniques, are key to identifying areas where new methods can make an important contribution. Furthermore, the use of nanomaterials for these purposes is presented. Later on in the chapter, the characterisation techniques used to study these materials will be introduced. To study proteins using APT, a silica matrix is used, and background information on silica is presented in the final section of this chapter.

2.1. Biomaterials

Man-made materials that come in contact and interact with biological systems, such as living tissue and microorganisms, are called biomaterials [9]. One important group of biomaterials is surgically inserted medical implants, such as prosthetic joints and internal fixation devices. They are routinely used, improving health and quality of life for many individuals around the world [10][11]. While generally successful, failure of implanted medical devices caused by poor tissue integration or biomaterial-associated infections (BAIs) can occur. Such complications may require the use of antibiotics or revision surgery [12][13]. Biomaterials are often designed to have favourable interactions with the intended biological system for their applications, such as interacting with cells and macromolecules in the body when used as implanted medical devices. However, these properties can also provide a favourable environment for potentially harmful bacteria. Current strategies for prevention and treatment of these types of infections are the use of conventional antibiotics and, if necessary, revision surgery. The use of antibiotics is associated with the risk of increased tolerance of bacteria to such compounds and the eventual development of antibiotic resistance in pathogens, which is an emerging healthcare crisis. Revision surgery, on the other hand, is also associated with discomfort for the patient, high costs, and considerable risk of new infections afterwards.

A commonly used metal for implants is titanium, partly due to its native surface oxide having a natural affinity for direct binding to the bone, thus integrating through a process called osseointegration [14]. This property can be improved further by altering the topography of the surface through various techniques, such as acid etching, blasting, and anodic oxidation [15]. The surface of a titanium implant can also be coated with a more bioactive material, such as hydroxyapatite, which is chemically similar to the mineral component of bone [16][17]. However, such coatings are associated with a risk of

delamination of the hydroxyapatite layer, preventing successful tissue integration [18]. The risk of delamination is related to the thickness of the coated layer, and consequently, thinner layers are pursued [19]. One such method is the application of hydroxyapatite nanoparticles (nanoHA) to the titanium implant surface. The nanoparticles have a high resemblance to bone mineral and have been shown to improve osseointegration without increased risk of bacterial infections.

While faster and stronger osseointegration lowers the risk for BAIs by reducing the opportunities for bacteria to cultivate on the implants, the need for new strategies to prevent and treat BAIs remains. One such approach is to design biomaterials with antibacterial properties. Examples of such strategies include contact-killing surfaces, coatings that release antimicrobial substances, and non-adhesive surfaces. Advances in nanotechnology and the development of nanomaterials have opened new avenues for designing antibacterial biomaterials. One strategy is photothermal therapy (PTT), where a photothermal agent converts the energy from photons into heat, treating a medical condition [20]. For photothermal therapy to treat BAIs, near-infrared (NIR) light is ideal, as photons with such wavelengths (650-900 nm) exhibit optimal tissue penetration as the absorption by water and haemoglobin is minimal in this range [21].

Another common use for implanted biomaterials is in total knee arthroplasty [22], where a knee damaged, for example, by arthritis is resurfaced by using metals and plastics to cap the ends of the bones forming the knee joint with the knee cap. To prevent failure of the implant by tribological degradation, or aseptic loosening caused by ions released from the implant triggering an immune response, surface modifications or coatings are employed [23]. One such surface coating that is commonly used is a multilayer system with an outer layer of ZrN [24]. It has been observed that this type of coating can oxidize, indicated by a colour change [25]. Oxidation beyond the native oxide formation can occur as a consequence of bio-corrosion as well as tribological loading or a combination of these factors [26]. While often observed and potentially a factor for implant failure, the mechanisms of oxidation in the different regions of a knee replacement are not yet fully understood.

2.2. Biomolecules

While the importance of biomaterials for the advances in modern healthcare can hardly be overstated, understanding the biological system itself and using active substances to interact with it are of at least equal importance. All living organisms are built of different compounds of various types. The fundamental macromolecular components that make up living cells are divided into four categories, glycans or polysaccharides, lipids or fatty acids, nucleic acids (such as DNA), and proteins [27].

2.2.1. Basis and role of proteins

Proteins are the largest [28] and most diverse group of the fundamental macromolecules of life and carry out a wide range of functions in living organisms, such as transporting other molecules, responding to stimuli, facilitating (catalysing) chemical reactions where one compound is converted into another, movement, and providing structure to cells. To perform all of these roles, a vast number of different proteins are required, yet they are all made from the same limited number of building blocks, the 20 naturally occurring amino acids. These can be combined in countless variations into linear polymers, often hundreds of amino acids long, by peptide bonds. The sequence of each protein is determined by its corresponding gene in the organism's DNA, which acts as a blueprint and is transcribed to RNA in the nucleus of cells and transported out to the ribosomes where it is translated into a protein through a process called the central dogma of biology [5]. These processes are schematically illustrated in Figure 2.1.

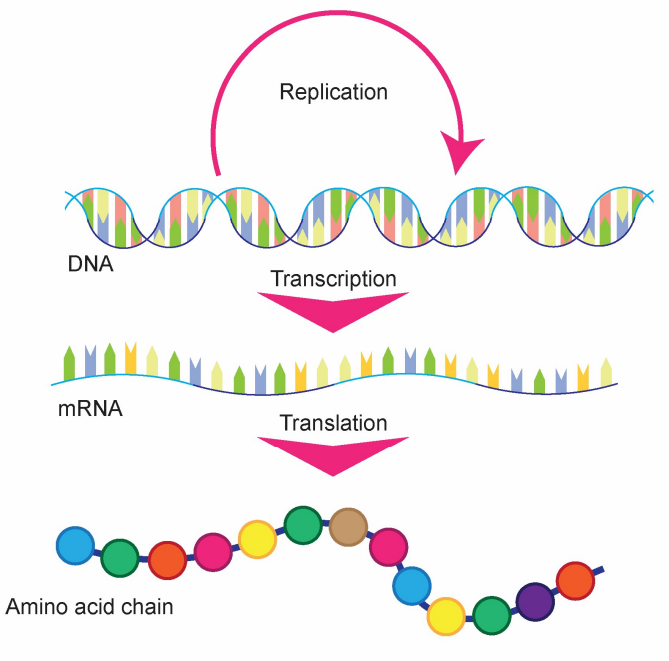


Figure 2.1: Schematic overview of the central dogma of molecular biology. DNA can be replicated as well as transcribed into mRNA, which in turn can be translated into a corresponding polypeptide.

2.2.2. Structure and characterization of proteins

The amino acid sequence of proteins can routinely be determined using established methods to study the nucleic acid sequence of the gene coding for the specific protein in question. However, the linear amino acid sequence represents only the primary structure of the protein. After the protein has been synthesized into its predetermined amino acid sequence through translation of the RNA in the ribosome, it folds into a three-dimensional structure that determines its biological functionality. The levels of protein structure are schematically illustrated in Figure 2.2. For example, catalytic properties of proteins and their ability to specifically bind to other proteins or molecules are strongly dependent on their 3D structure and active or binding sites on the molecular surface [29].

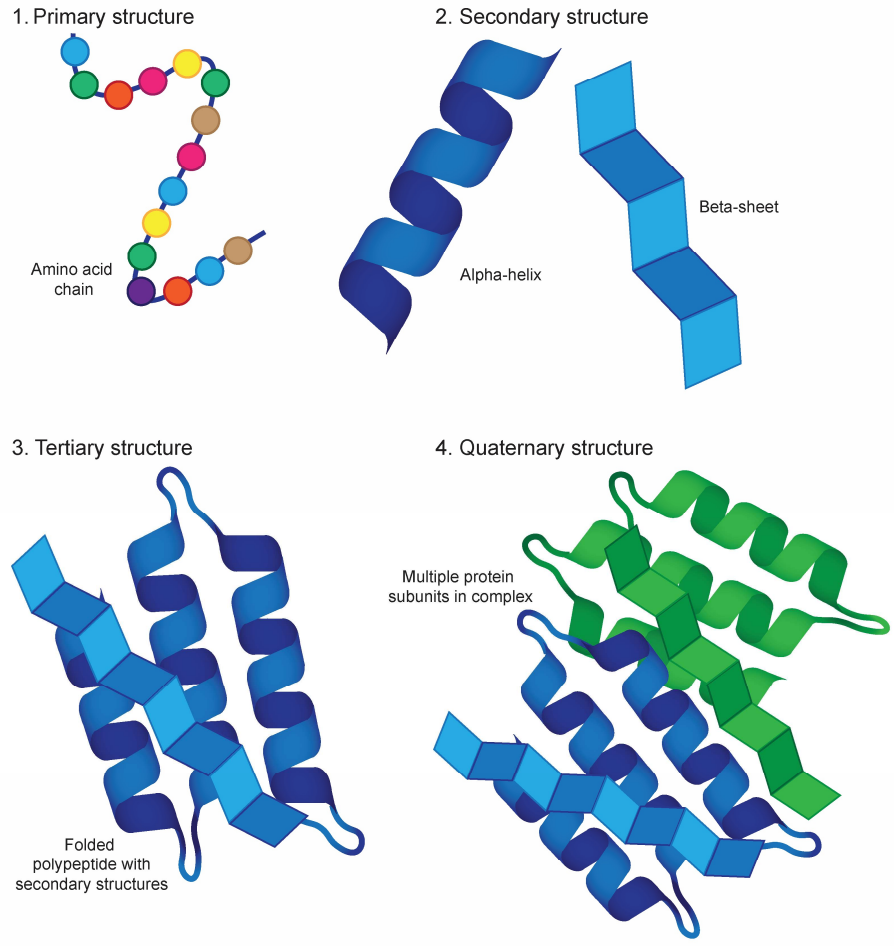


Figure 2.2: Schematical illustration of the hierarchy of protein structures. 1: The amino acid sequence is the primary structure of the protein. 2: Sections of the amino acid sequence is folded into secondary structures, such as, α-helices or β-sheets. 3: The amino acid chain is folded into a 3D structure. 4: Several folded amino acid chains can acts as subunits in a complex protein.

Determining how a protein will fold from its amino acid sequence alone has historically proven challenging, raising the need for experimental techniques to study and ascertain the 3D structure of proteins. The first protein structures to be experimentally characterised were determined using X-ray diffraction [30][31]. While successful and a methodology that has proven very valuable in determining the 3D structure of proteins, the technique has inherent limitations. To study proteins using X-ray diffraction, the biomolecules must be organized in larger crystal structures [32], which is a time-consuming process and not suitable for many proteins as they do not retain their native structure under the required conditions to form crystals. Furthermore, the dynamic and environmentally dependent nature of proteins [33] is lost when crystallized to larger, solid structures.

Another technique that has provided valuable insights into proteins is Nuclear Magnetic Resonance (NMR) spectroscopy, revealing information about the chemical environment of the constituent atoms of the molecules [34]. NMR utilizes the magnetic properties of the nucleus of atoms with spin, which reorient themselves in an external magnetic field at specific resonance frequencies depending on their isotopic nature and chemical environment. Atomic nuclei with even numbers of protons and neutrons have spin number zero and are not NMR-active [35]. A consequence of this is that the most naturally abundant carbon isotope, ^{12}C, is not NMR-active and proteins have to be enriched with ^{13}C to be studied with NMR spectroscopy. NMR studies of proteins are generally limited to smaller proteins or fragments of proteins, but progress is being made to enable characterization of larger proteins. Isotopically labelled proteins are generally obtained by expression from bacteria, and not all proteins can be expressed this way, limiting the number of compounds that can be analysed with NMR.

The latest revolution in experimental studies of protein structures is the introduction of cryogenic transmission electron microscopy (CryoEM) [36]. In traditional TEM, the scattering of high energy electrons is used to image a sample on the nanometer scale. This requires that the sample is in a high vacuum environment and is resistant to damage from the electron beam, which historically excluded biological materials from being studied with the technique. Many of these limitations can be avoided by CryoEM, where a protein solution is frozen by vitrification into amorphous ice and visualized under cryogenic conditions. By imaging a large number of proteins, that are assumed to be randomly oriented in the ice, a high-resolution reconstruction of the 3D structure can be obtained by a computational method known as single particle analysis.

Modern computational techniques have also been emerging as a powerful tool for protein characterization, as the folded 3D structure can be predicted from the amino acid sequence with good accuracy using machine learning tools based on neural network-based models [37]. While the first models were limited to isolated protein structure, newer network architectures allow for predictions of protein interactions with

ligands, DNA, and other proteins [38]. However, the model is still limited with regard to protein dynamics as the training data in protein databases (PBD) is lacking, as well as antibody-antigen interactions.

One class of proteins that are of great interest for healthcare purposes are transmembrane receptor proteins, as they are the largest class of targets for pharmaceuticals [39]. They are inherently more challenging to study than water soluble proteins, as their native structure is dependent on the integration into the membrane lipid bilayer. In recent years, progress has been made towards enabling the current experimental techniques to studies of membrane proteins, such as crystallization for XRD [40], analysis of membrane proteins in lipid nanodiscs using NMR [41][42], and the use of detergents as well as nanodiscs to enable cryo-EM studies [43][44]. However, due to the significant importance of membrane proteins, new methods that are especially suitable to study such biomolecules would be of great value. One method that could contribute to this pursuit is atom probe tomography, which is described in a later section of this chapter.

2.3. Nanoparticles

Nanoparticles are defined as particles with dimensions between 1 and 100 nm (0.1 μm), regardless of shape [9]. Owing to this small size, they have a high surface to volume ratio, and consequently display remarkably different properties from the same material in a larger bulk form [45]. They have been used since antiquity, despite a lack of complete understanding, to obtain desired properties in various materials [46]. In more recent times, advances in material sciences have led to rapid growth in development, understanding and commercialization of these materials. Nanoparticles are currently being applied in various areas, such as electronics, energy conversions, and catalysis. They are also used in biological applications, mainly for sensing and transport. As a consequence of the found uses of these systems in several different fields, it is not surprising that the synthesis and characterization of nanoparticles have been well explored areas of research.

Nanoparticles can be formed through two main pathways, top-down and bottom-up. Top-down synthesis refers to making larger objects of the material of interest smaller through the sequential use of various methods, until they are in the nanometer regime. Methods used are mechanical processes, such as grinding, and lithography methods using electrons or ions. Bottom-up synthesis methods are based on the assembly of even smaller components, such as individual molecules, to form nanoparticles of a desired size and shape. One well-known example of a bottom-up synthesis is the Turkevich method, where spherical gold nanoparticles are obtained by the reduction of a chloroauric acid solution ($HAuCl_4$) by citrate in boiling water [47]. This can yield a nanoparticle suspension with narrow size distribution. The citrate act as both a reducing

agent for the $HAuCl_4$ and as a stabilizing agent for the eventual nanoparticles formed by the gold ions. The size of the obtained nanoparticles can be controlled by adjusting the citrate and $HAuCl_4$ ratio [48]. The obtained particles can later be used as seeds to form larger nanoparticles with varying shapes by seed-growth formation through addition of a growth solution [49]. The growth solutions used in such cases can for example contain the same chloroauric acid as used to form seed particles, together with stabilizing compounds and shape directing agents, which when growing gold nanoparticles often is a silver compound [50]. Silver has an affinity to certain facets of the crystal structure of gold, reducing particle growth on those specific facets. This causes the nanoparticles to grow faster in the direction of the remaining facets, promoting the emergence of specific particle shapes.

The limited size of metal nanoparticles causes unique properties to emerge, compared to the same material in bulk, with regard to the interaction with light, as observed by Faraday in the mid-19th century [51]. One such property for especially gold nanoparticles is the possibility for the conduction band electrons to oscillate in resonance with an oscillating electromagnetic field of light [52][53]. In nanoparticles smaller than the wavelength of the incident light, the oscillating resonance of the conduction band electron cloud is distributed over the whole particle volume, an effect called localized surface plasmon resonance (LSPR). This occurs at specific wavelengths of incident light, called the resonance frequency, which is dependent on properties of the nanoparticle in question. The oscillations eventually decay through photon or heat emission [54]. Spherical gold nanoparticles exhibit one LSPR frequency due to their symmetrical shape, which is in water around 500 nm. A rod-shaped gold nanoparticle, however, will have two resonance frequencies, one associated with oscillations along the short axis and one along the long axis [54]. The longitudinal resonance frequency is dependent on the nanorod's aspect ratio and increases when the length-to-width ratio increases.

Gold nanorods with controllable aspect ratios can be synthesized by a bottom-up wet-chemical seed-growth process, where a seed suspension is made by reducing chloroauric acid in the presence of hexadecyltrimethylammonium bromide (CTAB) and sodium borohydride [55]. The seed particles are added to a growth solution containing $HAuCl_4$, CTAB, silver nitrate, ascorbic and hydrochloric acid. Ascorbic acid reduces the $HAuCl_4$ in the presence of the gold seed particles [54] while CTAB and silver ions have a shape directing role, preferentially binding to certain facets and promoting growth into the desired rod-shape [55]. The aspect ratio of the rods can be tuned by adjusting the ascorbic acid and silver nitrate concentrations.

2.3.1. Nanoparticle surface interactions

To use nanoparticles in practical applications, it is often desired to attach them to a surface of a material and several protocols have been developed to conduct such surface modifications with desired degrees of coverage. The methods used can be divided in two general categories, by using electrostatic interactions and by using chemisorption. When utilizing electrostatic interactions to cover a surface with nanoparticles, the surface charge of the particles should be considered, and the surface charge of the substrate should be chosen or modified to the opposite sign. Nanoparticles are generally stabilized by capping agents or ligands to use electrostatic repulsion to prevent aggregation. If these are positively charged, a negatively charged surface can be modified with nanoparticles using electrostatic interactions.

Chemisorption, on the other hand, utilizes covalent binding of the nanoparticles to immobilize them to a substrate surface. One strategy to achieve this is by modification of the substrate surface containing a terminating group that has a high affinity to the nanoparticles at hand and that will be exposed to the surrounding medium. Examples of such terminating groups are amino-groups and thiol-groups, which both have been used to immobilize inorganic nanoparticles to surfaces [56][57].

2.3.2. Nanoparticle biological interactions

Both inorganic and organic nanoparticles have seen a variety of biological applications. Several inorganic nanoparticles, mainly those of gold, silica, and iron oxide, have biocompatible properties and are as such used in different biological applications [58][59]. They can for example be used for drug delivery, as therapeutics, imaging agents, and for sensing [60]. Another example of therapeutical use of gold nanoparticles, is photothermal therapy (PTT), where heat released from the particles after excitation with resonant light can treat medical conditions [20][61] or have an antibacterial effect [62].

Organic nanoparticles that are of biological origin or character, such as lipid nanoparticles, have in recent years had an increased interest. The use of such particles for drug delivery, as used for mRNA vaccines, has been especially impactful [63]. Lipid nanoparticles are spherical particles made out of phospholipids or liposomes, meaning vesicles of lipid bilayers, meaning membranes usually made of phospholipids.

Hydroxyapatite nanoparticles, made from the same material forming the mineral component of bone, are another example of nanoparticles of biological relevance as they can be used in biomaterials designed to integrate with bone [64]. This has been demonstrated as a surface coating on implant materials, increasing the biocompatibility of the implant to the bone [65][66]. The bone growth onto the implant material is promoted, improving osseointegration and the risk for BAIs are reduced as the time required for proper adhesion is decreased.

As nanoparticles have been used in more biological applications and proposed for therapeutic use, concerns have been raised about their possible toxicity. However, there is no general answer to the question whether nanoparticles are toxic or not, it will depend on the properties of the particle, as well as the dose and exposure pathways [67][68]. Due to their small size, they can not only enter the body and organs, but also into individual cells and even organelles in the cells. There are therefore many ways they can negatively affect the functionality of cells, by mechanisms such as formation of reactive oxygen species, damage to cell membranes, disturbing functionality, and triggering of the immune systems. To ensure safe use of nanoparticles, where their potential as therapeutics is enabled, methods to study toxicology in relevant ways are needed. The need to study the toxicity of nanoparticles is not only important to enable their use as therapeutics, but also as inadvertent exposure is unavoidable due to widespread use and abundance.

2.4. Characterization Techniques

Natural sciences are fundamentally based on the observation and measurement of natural phenomena. As such, the progress of these fields throughout history has driven the need for more and more detailed and accurate methods of measurement. With the development of technology, increasingly sophisticated instruments have become available for researchers to study physical phenomena and materials in increasing detail. While we perceive and experience the world at the macroscale, the micro- and nanoscale are crucial for understanding phenomena and designing new materials that can contribute to improved quality of life. For studies at the nanoscale, an array of methods is applied, each relying on different probes and providing complementary information. In this section, the main techniques used in this thesis are described.

2.4.1. Electron Microscopy

The invention of the optical microscope enabled studies of materials at a more detailed scale than what is possible with the naked eye. Using lenses to spread the light reflected from the sample studied, magnifications as high as 1000x are possible, revealing features as small as 0.2 µm. The lower limit is defined by the wavelength of light in the visible range, 400-700 nm. To visualize even smaller features, one commonly used technique is electron microscopy, developed in the 1930s [69][70], where an electron beam accelerated at voltages high enough to reach far shorter wavelengths than visible light is utilized [71]. The electron beam is extracted from a source, generally a field emission gun (FEG) in modern electron microscopes, using strong electric fields and accelerated by an anode. It is then focused through a series of electromagnetic lenses to form a probe that interacts with the sample in the desired manner. When the electron beam interacts with the sample, several types of scattering events occur, generating different signals that can be collected to obtain information about the material. These types of

signals can be sorted in two general categories, scattered electrons and X-rays. The electrons will in general provide structural information about the sample, while the X-rays give chemical information. The X-rays are generated by the incident electrons exciting electrons in the sample, and the formed electron hole is in turn filled by an electron with higher energy. The difference in energy is emitted as a photon with an energy characteristic for the difference between the two electron shells and the specific element. The X-rays can be collected with an energy dispersive spectrometer and used to form a spectrum from which the chemical composition can be determined, both qualitatively and quantitatively. By collecting the X-ray spectrum from various parts of the analysed sample, chemical mapping can be performed.

Electron microscopy is generally required to be performed under high vacuum, in order to prevent the electron beam from being deflected or otherwise disturbed by gases in the analysis chamber. This places a requirement on the sample being studied to remain stable and keep its structure under vacuum conditions, generally preventing the study of liquid materials.

Scanning electron microscopy

The most commonly used type of electron microscopy is Scanning Electron Microscopy (SEM), in which the electron beam raster scan over the surface of the material studied. The electron beam is focused into a small spot using electromagnetic lenses and is scanned over the sample surface using scanning coils [72]. From each position during the scan, electrons generated from scattering events are collected by a detector and from the relative numbers of detected electrons, a contrast-based micrograph can be formed. By collecting secondary electrons (SEs), a micrograph with topographical information about the sample surface is obtained, as a higher number of SEs escape the sample at edges compared to flat surfaces. If, on the other hand, back scattered electrons (BSEs) are collected, an atomic number contrast micrograph will be obtained, as atoms with higher atomic number has a higher probability to scatter the incident electrons. The region in the sample from which the signals are generated is called the interaction volume of the incident electrons, which generally is pear-shaped. SEs are generated in the first few nanometres below the surface due to their shallow escape depth, while BSEs have a higher energy and can escape from a slightly larger region. The generated X-rays can travel even further through the material, often a few µm. This defines the spatial resolution of the different types of signals. In Figure 2.3, the SEM instrument is schematically illustrated, together with interaction volume of the incident electron beam and origin of the different signals detected.

As the sample is being scanned by the incident electron beam, poor conductivity can cause so-called charging effects, as the electrons are not readily transported away from the surface and will cause distortions and loss of resolution in the generated micrograph

[73]. This is generally circumvented by coating non-conductive samples with a thin layer of a conductive material, such as gold, prior to SEM analysis.

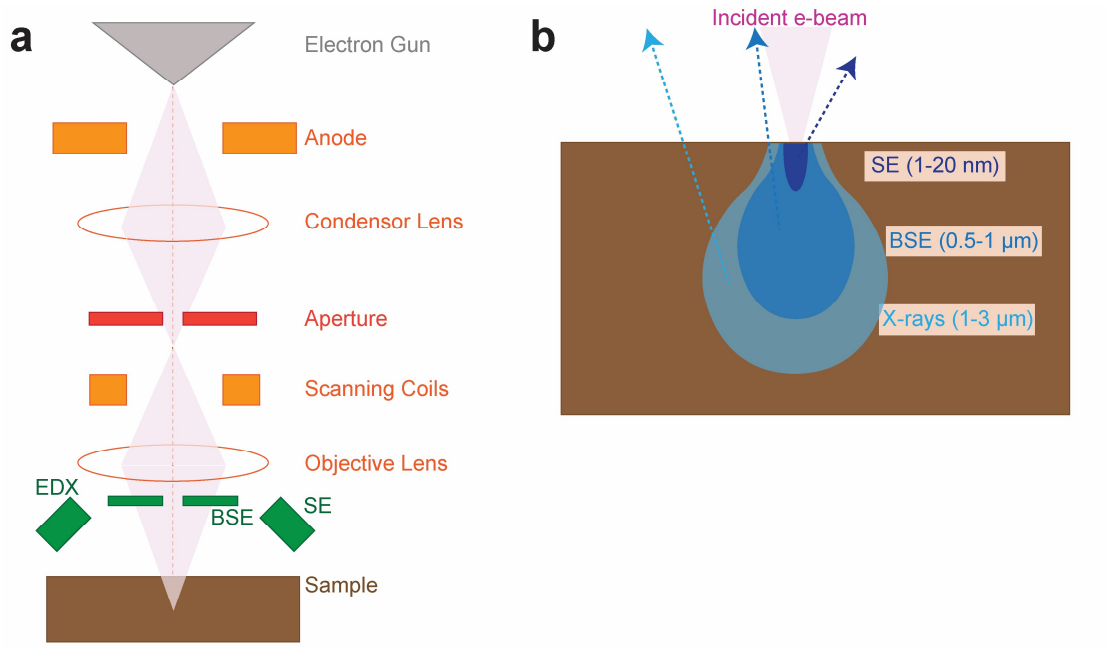


Figure 2.3: ***(a)*** *Schematic overview of the SEM instrument with the electron beam formation and manipulation, as well as the detectors.* ***(b)*** *Schematic overview of incident electron beam interaction with the sample and origin of the different types of signals that can be detected in SEM.*

Focused ion beam SEM dual beam systems

Combining a conventional SEM with a Focused Ion Beam (FIB), to make a FIB/SEM dual beam system, opens up expanded opportunities for material analysis and manipulation [74]. The FIB source is based on similar principles as the FEG but emits ions that are far heavier than electrons. Traditionally Ga^+ is used due to its low melting point but newer instruments may use Xe^+ generated by plasmas. By aligning the sample so the same region can be imaged by electrons emitted from scattering of both the incident electron beam as well as the focused ion beam, the high energetic ions can be used to mill away selected areas of the sample by scanning the FIB in defined patterns on the microscale. This allows for both depth profile imaging by making cross sections in the sample surface, as well as enables site specific specimen preparation for other analytical techniques [75]. By tilting the stage with regard to the ion-beam, milling can be used to cut the material at different angles, as seen in Figure 2.4. This is crucial for lifting out selected areas for further analysis. Other accessories can be attached to the dual beam system, such as a sharp micromanipulator needle needed for lift-outs, as well as a gas injection system (GIS) that can be used to introduce a metallic precursor gas

near the sample that enables deposition of structures in well-defined microscale patterns using the ion beam.

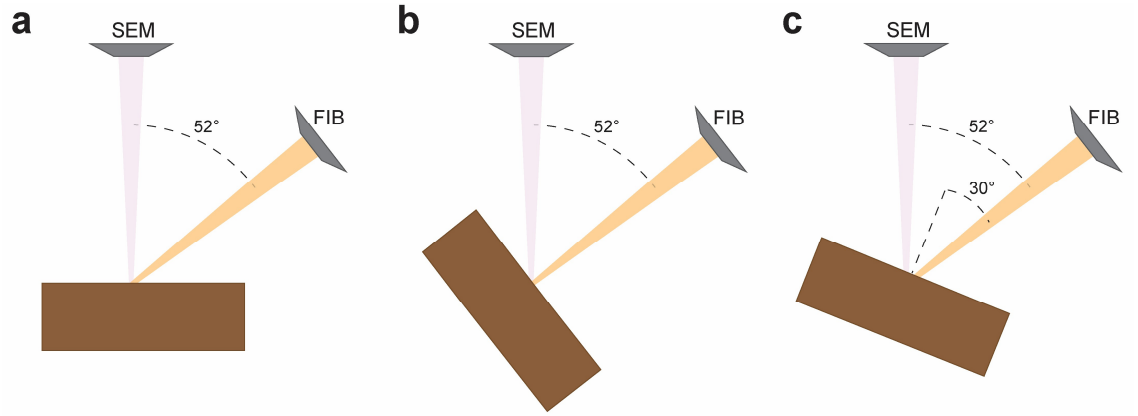


Figure 2.4: ***(a)*** *Schematic overview of the FIB/SEM set-up with the sample perpendicular to the electron beam.* ***(b)*** *The same setup with the sample surface perpendicular to the ion beam.* ***(c)*** *The same setup with the sample tilted to a position between the electron and ion beam.*

Transmission electron microscopy

The other main category of electron microscopes is the transmission electron microscope (TEM), in which the electron beam is accelerated using high voltages to be able to, as the name suggests, transmit through the sample [71]. This requires the sample to be sufficiently thin to be electron transparent, which usually is around 100 nm or thinner. In normal mode TEM, a broad, parallel electron beam is used to illuminate the sample and be detected on the other side of the sample. The electron beam can also be focused into a small probe converging on the sample and raster scanning over the sample is made to perform scanning TEM (STEM). In both cases, the micrograph obtained is a 2D projection of the 3D sample displayed on the screen or camera, further highlighting the importance of thin samples to reduce overlapping features in depth and improved resolution.

The electrons transmitted through the specimen can be divided into unscattered, elastically scattered, and inelastically scattered electrons. Electrons that are unscattered or scattered at very small angles can be collected with a detector at the optical axis below the sample, in what is referred to as bright-field imaging. The unscattered electrons can exclusively be detected by inserting an objective aperture around the transmitted beam in the back focal plane. The contrast in the obtained image is due to sample thickness and diffraction, as thicker parts of the sample will scatter more of the incident electrons and appear darker, as will atoms with a higher mass. By selecting the elastically scattered electrons to form the image, a dark-field (DF) image is obtained. This can be done by the use of an annular dark-field (ADF) detector, which is a circular detector that is open in the middle to exclude the unscattered electrons and exclusively

detect electrons scattered at angles between 10 and 50 mrad. To selectively study the electrons elastically scattered by for example a specific plane in the sample's crystal lattice, the objective aperture in the back focal plane can be centred around the corresponding diffraction spot. Using an ADF detector that collects electrons scattered at angles higher than 50 mrad is called high angle annular dark field (HAADF) and at such angles, electrons scattered by the Bragg conditions are excluded. This imaging mode is therefore more sensitive to atomic number contrast, and regions with higher mass atoms will appear bright in the obtained image. Figure 2.5 schematically illustrates the basic TEM instrumentation as well as the electron beam interaction with the same and the signals detected in TEM and STEM mode.

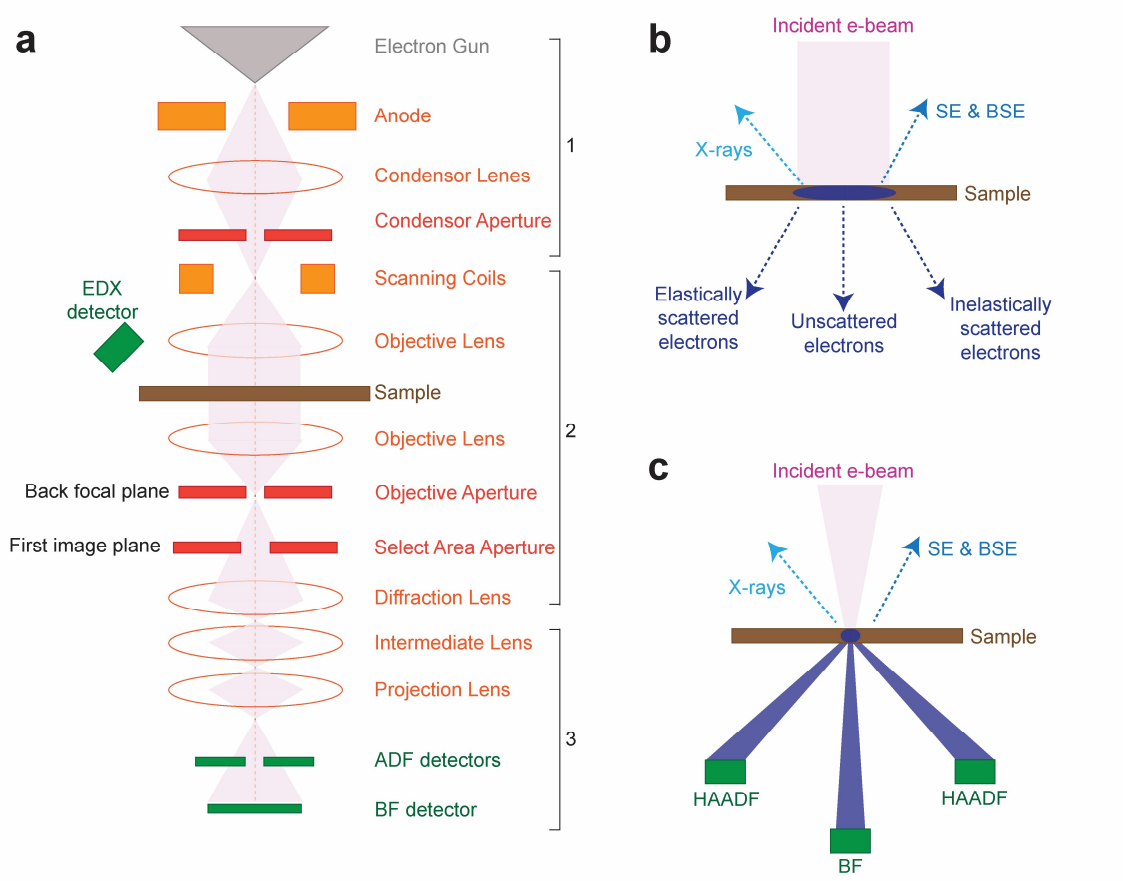


Figure 2.5: ***(a)*** *Simplified schematic overview of the TEM instrumentation and electron beam path when operated in TEM mode. Group 1: illumination system, group 2: image forming system, group 3: projection and image recording system.* ***(b)*** *Schematic overview of incident electron beam interaction with the sample and origin of the different types of signals that can be detected in TEM mode.* ***(c)*** *Schematic overview of incident electron beam interaction with the sample and origin of the different types of signals that can be detected in STEM mode.*

When a large or no objective aperture is used, phase contrast from the interference between the transmitted and diffracted beam can be used to obtain the highest possible

resolution to study atomic scale crystal structures. This mode can be referred to as high resolution TEM (HRTEM) and requires minimal lens aberrations, enabled by modern Cs correctors.

Similarly to SEM, characteristic X-rays are generated when the incident electrons interact with the sample and can be collected for chemical analysis. The inelastically scattered electrons have lost energy when passing through the sample and can also be used for chemical analysis by electron energy loss spectroscopy (EELS).

2.4.2. Atom Probe Tomography

APT is a powerful characterization technique that provides 3D information of the chemical composition of a material with near atomic resolution [8][76]. The technique is developed from the Field Ion Microscope (FIM), which was invented in the mid-20th century [77] and the first analytical technique that enabled the observation of individual atoms [78][79]. The FIM was further developed into the atom probe, giving information about the character of the individual atoms utilizing time-of-flight mass spectrometry [80].

APT has mainly been used to study metallic materials, providing insight into heterogeneities in the chemical composition in three dimensions at a sub-nanometer scale. While crystallographic lattice features in metals, such as vacancies, defects and boundaries are not as clearly observed as with TEM, they can be revealed by chemical segregation using APT. Examples of such features are the segregation of elements at grain boundaries and nanoscale precipitates in the microstructure of materials. As such, APT is a strong complementary technique to electron microscopy and other characterization methods. It fills a unique niche in terms of combining resolution and chemical sensitivity while also being inherently a 3D analysis method.

Fundamentals

APT is enabled by the physical phenomena of field evaporation, where surface atoms from a material can be desorbed and ionized at sufficiently high electrostatic fields at the surface. The electrostatic field, F, at the surface of a hemispherical sample with the radius R, at the applied voltage V, and with a field factor k, can be calculated using Eq. 2.1. The critical field strength required is called the evaporation field and is a material specific property, generally in the order of ~10 V/nm [81].

$$F = \frac{V}{k_f R} \qquad \text{(Eq. 2.1)}$$

Field evaporation is generally considered to be a thermal process [82], and the evaporation field has a temperature dependent component, meaning that at higher temperatures, the probability of field evaporation is higher. The temperature dependence of the evaporation field is illustrated schematically in Figure 2.6.

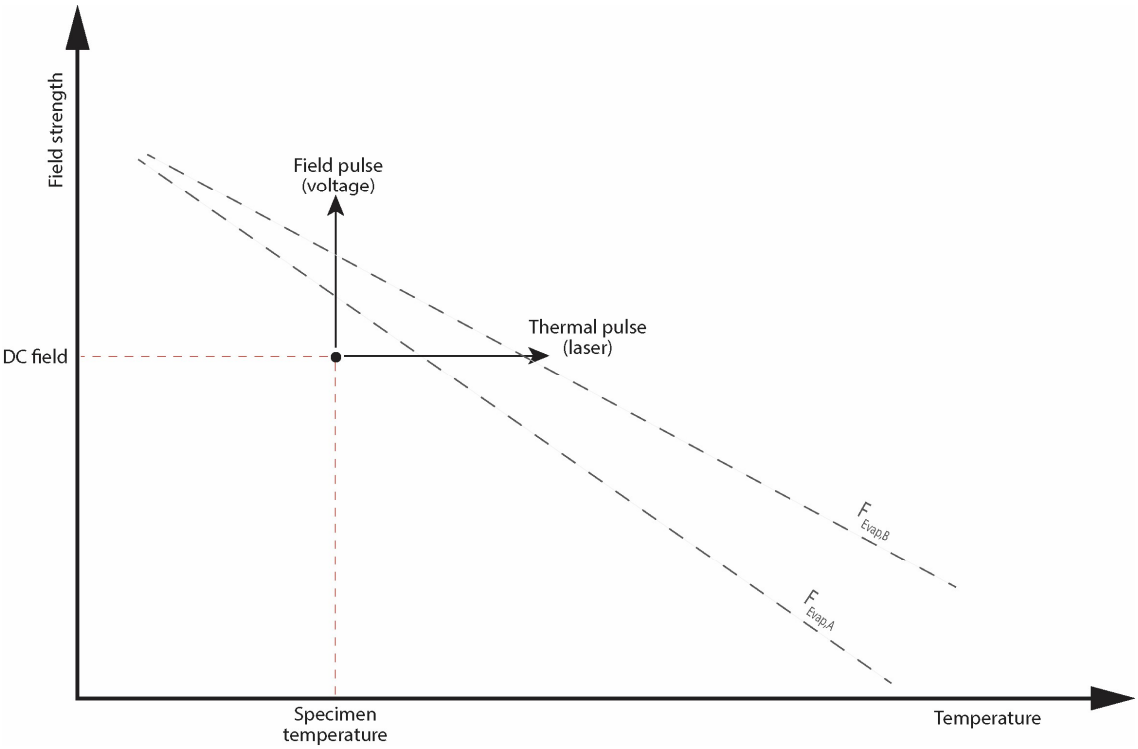


Figure 2.6: Schematic graph illustrating the temperature dependence of the evaporation field, Fevap, for two arbitrary materials A and B. The effect of voltage and laser pulsing to momentarily pass the energy barrier for field evaporation from a standing DC field and specimen temperature is shown.

The operational principle of pulsed APT is either the momentaneous increase of the electrostatic field at the specimen apex by pulsing the applied DC voltage or to use a laser pulse to reduce the evaporation field by increasing the temperature. In both cases, the probability of a surface atom to ionize is increased at a known point of time. Consequently, it is then possible to measure the time of flight as the time between the pulse and the detection of the ion.

The evaporated ions are initially single charged, but can by the process of post-ionization reach a higher charge state as one or more electrons tunnel back into the sample [83]. The probability of such events is related to the electrostatic field strength, and the ratio between ions detected with different charge states can be used to estimate the electrostatic field strength.

From Figure 2.6, a possible situation can be observed, where the electrostatic field between the pulses due to the applied voltage and specimen temperature is above the evaporation field for one phase in the sample, in order to maintain a desired evaporation rate of another phase of the sample. In this situation, ions from the lower evaporation field component will evaporate between the pulses, a phenomenon called preferential evaporation [84], which can cause biases in measurements of the material composition.

APT is one of few characterization techniques that also allows for studies of hydrogen, as hydrogen ions evaporated from the specimen will be detected with their corresponding mass-to-charge-state ratio similarly to other elements. However, it should be noted that hydrogen studies are associated with challenges as it is present in the analysis chamber as residual gases, despite the ultra-high vacuum, and will influence the measurement [85][86].

Instrumental development of APT is mainly directed towards utilizing new lasers to trigger field evaporation, with the latest commercially available instrument being equipped with a deep-UV laser (λ=257.5 nm) [87]. Reported development of instrumentation utilizes extreme UV laser (λ=29.6 nm), possibly opening up new pathways of field evaporation such as direct ionization rather than bulk thermal heating of the tip [88]. It has also been demonstrated that it is possible to utilize lasers with far longer wavelengths as well, in the THz-range, to achieve field evaporation from Aluminium samples with negligible thermal effects and crystallinity of the specimen observed in the reconstructed data [89].

Instrumentation and data analysis

The prerequisites for APT analysis require rather advanced instrumentation. The specimen to be analysed is mounted on a stage cooled to cryogenic temperatures, in the range of 20 – 80 K and is placed in an ultra-high vacuum chamber, with pressures in the range of 10^{-8} – 10^{-9} Pa. The stage and specimen are aligned to a counter electrode, and a standing high voltage is applied to the stage to reach electrostatic fields on the surface of the specimen sufficiently high to achieve field evaporation. Through an aperture in the counter electrode, the evaporated ions are traveling towards a position sensitive detector, that registers the location of an ion impact. The single ion is converted to a bunch of electrons through the microchannel plates and electrons are collected by an anode consisting of delay lines calculating the impact position [90][91]. The time of flight of the ion is recorded by the time between the pulse triggering evaporation and the time of impact on the detector. The counter electrode is replaced by a local electrode in the commonly used commercial local electrode atom probe (LEAP) instruments [92][93], which have the benefit of enabling subsequential analysis of several specimens and thus higher throughput. The working principle of APT is illustrated schematically in Figure 2.7.

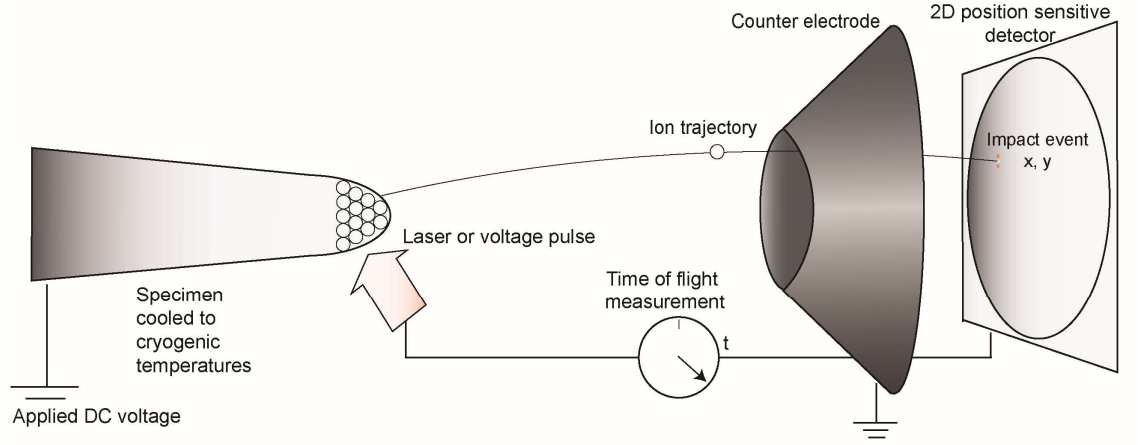


Figure 2.7: Schematical illustration of the working principle of APT and the instrument setup.

For each ion evaporated and detected during APT analysis, the x-y position on the detector, the time between the pulse and detector event (time-of-flight, t_{flight}), and the voltage applied to the specimen at the pulse, V, are recorded, together with other parameters, such as the constant distance between specimen and detector, l. Using this information, the structure of the specimen can be reconstructed. From the recorded time-of-flight for each detector event, the mass-to-charge state ratio (m/n) of the ion can be calculated using Eq. 2.2 and the distribution of the ions detected during the analysis can be ordered in a mass spectrum.

$$\frac{m}{n} = 2eV\left(\frac{t_{flight}}{l}\right)^2 \qquad \text{(Eq. 2.2)}$$

In the mass spectrum, it is important to note that the field evaporated ions can have different charge states which will affect their flight time, and consequently where they will end up in the mass spectrum. For example, a $^{28}Si^{++}$ ion will end up at 14 Da in the mass spectrum and can consequently overlap with other ions such as $^{14}N^{+}$. Molecular ions can also be evaporated and detected, causing additional complexity in the mass spectrum analysis. To correctly assign the peaks in the mass spectrum, the natural isotope abundance of each element is often helpful, as the sensitivity and mass resolving power of APT is sufficient to distinguish different isotopes in their relative amounts.

As each detected ion is associated with x-y coordinates on the detector, the analysed specimen can be reconstructed into a 3D atom map together with the number in the sequence of the detected ions giving the z-coordinate. To determine the original position on the specimen surface from the hit coordinates on the detector, models for ion trajectories are used, generally based on the assumption of evaporation from a hemispherical specimen. The evolution of the specimen radius, as it becomes increasingly blunt as material is removed by the evaporation, can be assessed by the increased voltage applied during the experiment to maintain the evaporation rate, using

Eq. 2.1, or by an approximated tip profile based on an electron microscopy image of the specimen.

Using the reconstructed data, a great amount of information about heterogeneities in the chemical composition of the material can be obtained. Variations in atomic concentration of different elements can be studied using 1D concentration profiles, which can be taken from the full or selected parts of the analysis. For example, 1D concentration profiles can be taken over interfaces, grain boundaries, layers, and precipitates or clusters to provide insight in variation of composition at the near atomic scale. Regions where the concentration of a specific element is higher can be visualized and studied by forming iso-concentration surfaces, defining 3D volumes inside which either the atomic concentration or the density of atoms is above a selected threshold for the ion type of choice. When using this type of volumes, variations in the concentration of different elements as a function of the distance from the surface can be studied using proximity histograms (proxigrams), for example revealing segregation of solute atoms at precipitate surfaces. Information can also be extracted from the reconstructed data by measurement of the interatomic distances. By measuring the distances between neighbouring solute atoms in the 3D atom map, and comparing with randomized systems, small clusters can be identified and studied. Radial distribution functions can also be used to reveal interactions between solutes in the reconstruction. Ions that are co-located in the 3D atom map can be identified and provide information about the nature of clusters, precipitates and particles in the material.

Specimen preparation

In order to succeed with APT analysis, the material studied needs to be formed into a needle-shaped specimen with a sharp apex, generally with a diameter below 100 nm. This is to obtain the necessary electrostatic fields at the surface to field evaporate the atoms at the surface, which are material dependent but generally above 1 volt per Ångström (0.1 nm).

Traditionally, APT specimens have been prepared by electropolishing, where the material to be formed into a sharp needle initially is in the form of a wire. This wire is then electropolished into a sharp needle by dipping in a thin layer of an electrolyte solution while a current is applied [94]. The wire will be electropolished by moving it through the electrolyte layer and gradually made thinner until it ruptures. The radius at the breaking point will generally be small enough to trigger field evaporation when a sufficient voltage is applied in an APT instrument.

Preparing APT specimens by electropolishing is not a selective process, and the degree of control of which part of the material ends up in the confined volume of the tip is low. For this reason, FIB/SEM dual beam systems have become popular for site specific lift-out and specimen preparation [95]. Electropolishing also requires the material to be

conductive, while FIB/SEM specimen preparation can be applied to a wider range of materials. The same constraints as required for a material to perform SEM analysis applies. In recent years, the development of cryo-FIBs, where the sample is kept at cryogenic temperatures during the entire procedure, together with vacuum- and cryo-transfer systems [96], even more materials, such as frozen liquids and liquid-solid interfaces can be formed in APT compatible needle shaped specimens [97].

APT studies on biomaterials and biomolecules

The introduction of laser assisted APT and the possibility to study non-metallic materials opened organic and biological materials as a new area for the analytical method to be applied to [6]. Considering the constraints APT analysis put on materials, the first biologically related materials to be studied using the technique were hard biological materials such as bone and enamel, and hard biomaterials such as implants [98]. In order to study soft organic and biological materials, they generally need to be placed in a matrix that can withstand ultra-high vacuum, cryogenic temperatures, and be shaped into the sharp needle-shaped specimen, normally by FIB/SEM. Examples of such pursuits include the embedding of ferritin in an organic polymer resin [99], using graphene to incapsulate a ferritin solution on a pre-sharpened tungsten tip [100], and depositing amyloid-beta fibrils to pre-sharpened aluminium tips [101]. Proteins have also been embedded in silicon oxide, specifically silica, through a sol-gel concept for the purpose of APT analysis [102]. This approach is further developed in this thesis, and the material preparation is explored in the next section of this chapter.

2.5. Silica

Silicates, such as silica, are the most abundant materials in the earth's crust [103][104]. Silica is found in nature in various forms, such as quartz, which is one of the silicon dioxide polymorphs [105][106]. It is also the main component of materials such as sand and glass. With occurring in different forms and polymorphs, silica is fundamentally consisting of silicon atoms tetrahedrally coordinated by four oxygen atoms surrounding. The oxygen is in turn bridging two silicon atoms and this structure forms a three-dimensional network. From this structure, silica can occur both as a crystalline material, such as quartz, and as an amorphous material, without long range order [107].

Silica is also a material with a large number of technical and industrial applications, often in the form of colloidal particles.

Amorphous silica is a material that generally displays a high degree of porosity and consequently a large surface area. This property can be studied by techniques such as physisorption by nitrogen sorption, which simplified can be described as an analysis where a controlled amount of nitrogen gas is exposed to a sample and the partial pressure is measured. By this analysis, the surface area of the sample can be calculated using the Brunauer-Emmett Teller (BET) method [108]. From the obtained data, the porosity can also be inferred by for example the Barrett-Joyner-Halenda (BJH) model [109] in the mesoporous range (2-50 nm) and the Horvath-Kawazoe model [110] to calculate micropores (>2 nm).

2.5.1. Synthesis

While found in abundance in nature, for more sophisticated industrial or technical applications, silica is generally synthesized to obtain the specific required properties. In industrial applications, silica is often used in the form of colloidal particles. They can be synthesized by various routes, out of which one of the most common is the Stöber process [111]. The synthesis is a two-step method, first a precursor, often an orthosilicate compound such as Tetraethyl orthosilicate (TEOS), is activated through hydrolysis as seen in Reaction 2.3. This is followed by a condensation polymerization reaction, shown in Reaction 2.4 and 2.5, that forms the oxygen bridges between the silicon atoms building up the silica network. During the condensation step of the process, either an alcohol (Reaction 2.4) or water (Reaction 2.5) is formed as a byproduct [112]. The Stöber process is pH sensitive and either acidic or basic conditions are used to catalyse the hydrolysis of the silicate precursor. The formation of the colloidal silica can be controlled by the choice of either acidic or basic conditions, as hydrolysis is faster at low pH while condensation is faster at high pH [113]. This causes the silica formed under basic conditions to be more porous than the one formed under acidic conditions. The type of pathways orthosilicic acids form silica are also known to be dependent on pH and presence of salts, affecting the characteristics of the gels obtained [114].

$$\equiv Si - OR + H_2O \leftrightarrow \equiv Si - OH + ROH \quad \text{(Eq. 2.3)}$$

$$\equiv Si - OR + OH - Si \equiv \leftrightarrow \equiv Si - O - Si \equiv + ROH \quad \text{(Eq. 2.4)}$$

$$\equiv Si - OH + OH - Si \equiv \leftrightarrow \equiv Si - O - Si \equiv + H_2O \quad \text{(Eq. 2.5)}$$

To avoid acidic or basic conditions, as well as the formation of alcohols as precursors, other methods for synthesis of amorphous silica are available. One example of such strategies is to use aqueous solutions of alkaline silicates, such as sodium silicate, which is commonly known as water glass. These solutions are soluble at basic conditions, but rapidly gels when the pH is decreased to neutral levels. The pH can be adjusted by addition of buffers, or by the use of a cation ion exchange, where the sodium ions are replaced by hydrogen ions. The pH of the silicate solution will then be lowered from basic and condensation polymerization initialized. Drying of the gel will form solid amorphous silica glasses. The shape of the materials synthesised by these sol-gel processes will generally be determined by the shape of the container upon drying, but thin films can be made by for example dip- or spin-coating of the solution [115].

2.5.2. Protein immobilization and encapsulation

While inorganic, silica is found in living organisms, such as silicified algae called diatoms [116]. Inspired by this, silica has been found to be a useful matrix material for encapsulation of biomolecules, improving activity and stability of enzymes [117][118]. Immobilization of proteins can be used in applications such as biosensing and biocatalysis. For successful immobilization, it is essential that it is performed at physiological conditions in terms of temperature, pH, and avoiding compounds that cause denaturation to ensure that the structure of the proteins is preserved [119]. For this reason, water glass have been used to perform immobilization in silica gels at neutral pH [120][121]. Computational molecular dynamic simulations of the interactions between proteins and orthosilicic acids when they replace the water have shown that the structure of stable folded proteins is retained [122].

3. Experimental Methods

In the following section, the experimental methods used for sample preparation and analysis in this thesis are described. For the biomaterials studied, emphasis is placed on the specimen preparation for TEM and APT analysis. Silica embedding of proteins is presented in some detail. APT specimen preparation is also described in depth.

3.1. Biomaterial specimen preparation and characterization

A number of different biomaterial systems has been studied in this work, and they were prepared and synthesized to various degrees prior to characterization.

For **Paper I**, a biomaterial with enhanced osseointegration, consisting of titanium nanostructured with hydroxyapatite nanoparticles (nanoHA) deposited on its surface, was provided by Promimic AB. These materials had been prepared by spinning of an aqueous dispersion containing hydroxyapatite nanoparticles, subsequently followed by heat treatment. Prior to preparation of TEM and APT specimens, the material was embedded by sputter coating of chromium, to protect the region of interest at the surface. TEM and APT specimens were then prepared by the conventional FIB/SEM lift-out protocol, described later in this section.

The possibility of preventing and treating bacterial infections was explored in **Paper II** by providing a biomaterial with antimicrobial properties through surface modification with photothermal gold nanorods (AuNR). The particles were synthesized by a seed-mediated synthesis [55], to obtain nanorods with specific aspect ratios. In the first step, a seed suspension was synthesized by reduction of a gold (III) chloride solution ($HAuCl_4$) with hexadecyltrimethylammonium (CTAB) and sodium borohydride under stirring at 30 °C. AuNR dispersions were obtained by addition of the seed solution to a growth solution consisting of hydrochloric acid (HCl), $HAuCl_4$, CTAB, silver nitrate ($AgNO_3$) and ascorbic acid. The aspect ratio was controlled by varying the amount of $AgNO_3$ and ascorbic acid in the growth solution.

The biomaterial studied in **Paper III** was the AS VEGA System® femoral component of a knee implant provided by Aesculap AG (Tuttlingen, Germany) after use in a patient for two years after removed after revisional surgery due to implant loosening. A similar, as-fabricated implant was also studied for comparison and determination of effects of *in vivo* use.

3.2. Silica synthesis and protein embedding

To analyse biomolecules, specifically proteins, using APT, a sample preparation strategy utilizing embedding in a solid silica matrix was employed in this work. This method is designed to preserve the proteins in their native state from an aqueous solution while the surrounding water is replaced by a silicon-oxide-network that is

condensed through the so-called sol-gel process. This process is commonly controlled by acid or base catalysis, but to avoid denaturation of the proteins due to such conditions, an ion-exchange is utilized where an alkaline silicate solution is neutralized to reduce the pH and initiate gelling.

Silica was synthesized from a sodium silicate solution which was diluted with Milli-Q water (Millipore, > 18.2 MΩcm) passed through an ion exchange column. The column was prepared by placing an ion exchange resin in a plastic syringe. For ion exchange of 2 - 3 ml sodium silicate solution (Supeclo), diluted 1:3 with Milli-Q water, an ion exchange column was prepared using 20 ml plastic syringes. In the bottom of a plastic syringe, about 0.5 – 1 cm of glass wool (approximately 1 g) was placed, followed by the rubber seal from the plunger of another syringe with a small hole cut in it. On this, approximately 2.5 g of cationic ion exchange resin (AmberChrom 50WX8) was placed. The resin was regenerated and stored in NaOH [4M] prior to use. For the ion exchange, the NaOH was passed through the syringe and the syringe was then rinsed with Milli-Q water at least twice. The resin was then activated by passing 10 ml HCl [1M] through the column. The column was then adjusted by passing small volumes of Milli-Q water through it until the water had a pH in the range 4 – 6, before 2.5 ml diluted sodium silicate was passed through the ion exchange column. The pH of the silicate solution typically reaches around 5-8 after preparation by this method. While gelling initiates rapidly, the process can be slowed by storing the solution in a vial kept on ice. The use of ion exchange for silica synthesis is schematically illustrated in Figure 3.1.

The pH of the alkaline silicate solution can be controlled by varying in the amount of water passed through the column after the activation with HCl, prior to the passing of silicate solution. Less water, and lower pH of the final water passed through, will yield lower pH of the silicate solution.

For encapsulation of biomolecules, with a desired concentration in the silica, addition of the biomolecules is done immediately after the silicate solution has been passed through the ion exchange column. The silicate solution was then placed in an oven at 37 °C for curing.

For the protein containing bulk silica samples studied in **Paper VII**, water was passed through the ion exchange column until the pH of the extrude was approximately 5. The final pH of the sodium silicate solution was 8 after being passed through the ion exchange column. To 250 µl silicate solution, 50 µl ^{13}C-labelled Green Fluorescent Protein solution (1 mg/ml) was added.

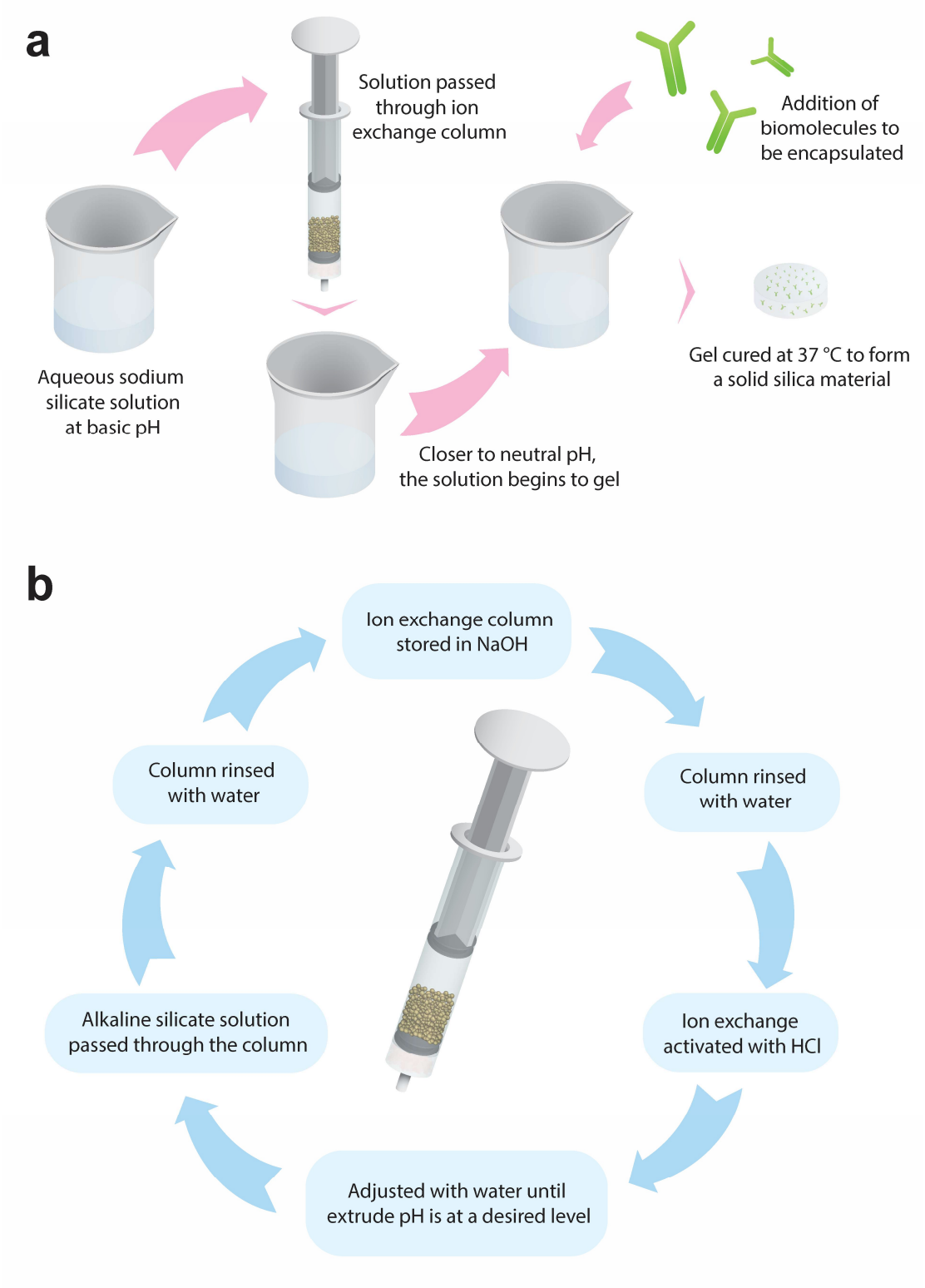


Figure 3.1: ***(a)*** *Schematical overview of the silica synthesis and protein embedding protocol used.* ***(b)*** *Schematic overview of the cyclical use of the ion exchange columns.*

3.3. Silica embedding of nanostructured surfaces with proteins

To circumvent the inherent challenges related for studying non-conductive materials using APT, with poor absorption of light in the visible range, as well as material porosity and poor heat conduction, it was suggested to reduce the protein containing silica region of the material to be analysed. In order to form such a material, the strategy used in **Paper IV** was to surface immobilize gold nanoparticles, followed by binding of proteins to the particles and the subsequent embedding in a thin silica film.

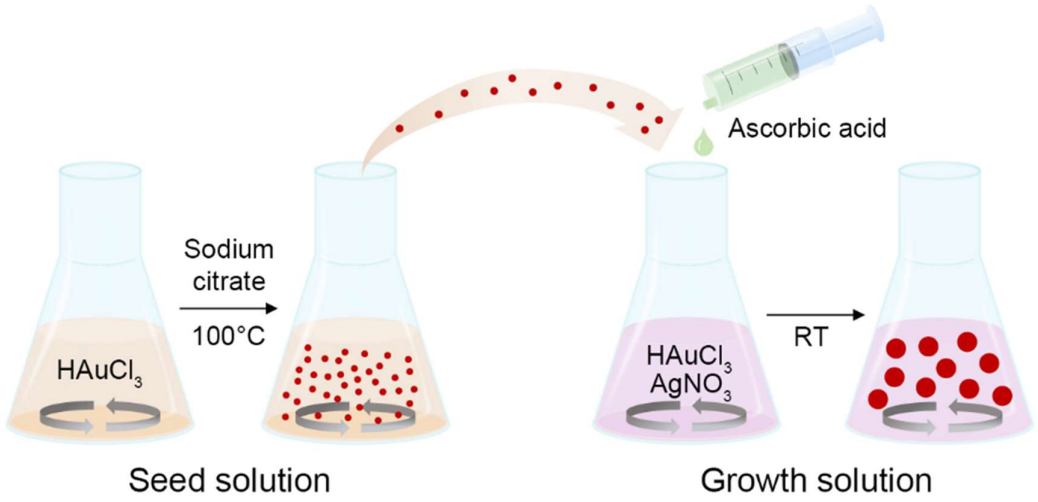


Figure 3.2: Schematic overview of the seed-growth synthesis protocol for gold nanoparticles. The seed solution is prepared by addition of sodium citrate to a boiling $HAuCl_3$ solution. Larger spherical gold nanoparticles are obtained by addition of seed particles to a $HAuCl_3$ and $AgNO_3$ solution followed by controlled addition of ascorbic acid.

Gold nanoparticles were synthesized by adopting a seed-growth procedure developed from the Turkevich method [123], schematically explained in Figure 3.2. A 100 ml 1.0 mM $HAuCl_4$ solution was added to 100 ml Milli-Q water and reduced at 100 C under stirring in order to prepare the gold seed solution. When the solution started boiling, 10 ml 38 mM sodium citrate was added, and kept at the boiling temperature for 80 min and then cooled down to room temperature. A growth solution was prepared by the addition of 20 ml 20 mM $HAuCl_4$ to 85 ml Milli-Q water under stirring, followed by addition of 200 µl 10 mM $AgNO_3$. All solutions containing silver nitrate were wrapped in foil. The final gold nanoparticles were grown to the desired size by addition of 7.5 ml of the previously prepared seed solution to the growth solution. The growth of the nanoparticles was controlled by addition of 15 ml 5.3 mM ascorbic acid at a rate of 0.6 ml/min. After completed synthesis, the final solution was left under stirring overnight.

Silicon wafers coated with a 10 nm thin chromium film were acquired from Substrata, Ångström Engineering, and heat treated at 600 °C to improve the adhesion between the layers and the silica film. The wafers were cleaned by ultrasonication in isopropanol followed by ethanol and after that, treated in a UV/O_3 oven. A self-assembled thiol-

terminated monolayer was then formed on the surface by emersion of the wafers in a 2% (3-mercaptopropyl) trimethoxysilane, $HS(CH_2)_3Si(OCH_3)_3$, (MPTMS), in toluene solution. The surface modified wafers were then emersed in a gold nanoparticle dispersion.

The gold nanoparticle modified wafers were embedded in a silica film by spin-coating a sodium silicate solution immediately after pH adjustment according to the previously described procedure. The procedure is schematically illustrated in Figure 3.3.

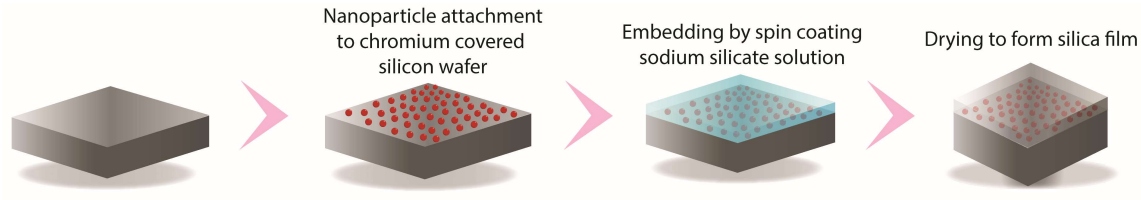


Figure 3.3: Schematic overview of binding of gold nanoparticles to chromium coated silicon wafers followed by silica embedding. The sodium silicate solution is adjusted to neutral pH by passing through an ion exchange column immediately before spin coating. The material is dried at 37 °C to form a glassy silica film.

In a separate experiment, it was attempted to bind proteins to the nanostructured wafer surface addition of thiol modified streptavidin followed by biotin modified gold nanoparticles with a diameter of 6 nm prior to silica embedding. The proposed material is illustrated in Figure 3.4.

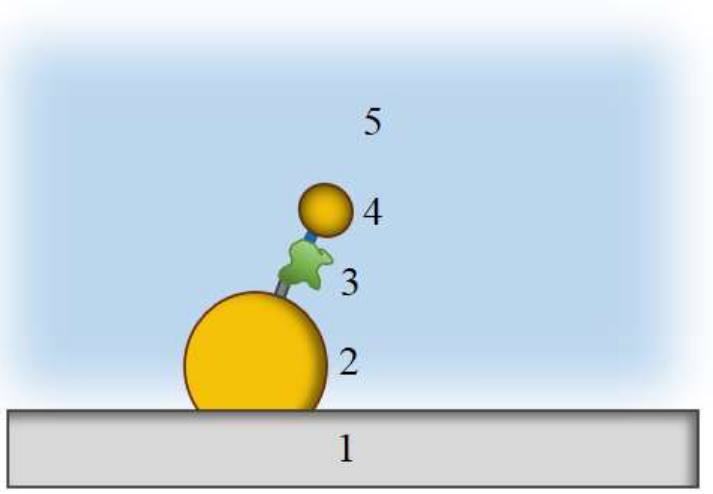


Figure 3.4: Schematic overview of the proposed material with proteins attached to gold nanostructured substrates and embedded in silica. 1: Silicon wafer with a 10 nm Cr-layer. 2: Gold nanoparticle attached to the surface. 3: Thiol modified streptavidin. 4: Biotin modified gold nanoparticle. 5: Silica film.

3.4. Specimen preparation

TEM and APT specimens were prepared by the conventional FIB/SEM lift-out procedure. The materials studied were generally coated with a protective layer to avoid beam damage to the region of interest during the lift-out and improve conductivity for SEM imaging. The layer was deposited by sputter coating using a Leica EM ACE600 (Leica Microsystems, Wetzlar, Germany). The titanium samples with nanoHA on the surface was coated with a 200 nm thick chromium layer to properly embed the region of interest. The ZrN explant and as manufactured implant were coated with platinum. The silica samples, both bulk sample and film on substrates, were coated with gold.

The lift-outs were performed using a FEI Versa3D dual beam FIB/SEM with a Ga ion beam (69 amu). The first step after introducing the sample was the deposition of a protective Pt-layer on the region of interest to be extracted from the sample surface using the gas injection system (GIS) in the instrument with a PT precursor. For preparation of APT specimens, the protective layer is usually a rectangular strip of 2 by 20 µm and a thickness of 1 – 2 µm. The stage with the sample was then tilted to 30° with regard to the ion beam and trenches were milled along the long sides of the Pt-rectangle. After the milling of the trenches is completed and they have freed the cantilever, the lift-out is released on one of the short sides by ion milling to leave it attached on only one side. The micromanipulator is then inserted and attached to the lift-out on the cut short side by Pt-deposition. Following this, the lift-out is cut free from the sample by ion milling on the remaining short side of the cantilever, and it can be extracted with the micromanipulator.

The lift-out is then placed in segments, approximately 2 µm long, on silicon flat top posts on pre-manufactured coupons (Cameca Scientific Instruments) and attached by Pt-deposition on the two angled sides. By this procedure, a normal 20 µm long lift-out is sufficient to make six APT specimens. To obtain sufficiently sharp specimens, the lift-out is polished by annular ion beam milling with gradually reduced inner diameters and ion currents with the stage perpendicular to the ion beam. Initial polishing is usually done at 30 kV, 1 nA, with an outer diameter of 6 µm and inner diameter of 2 µm until the specimen is sufficiently tall and it is ensured that no secondary tips will also be field evaporated during APT analysis. The final milling step at 30 kV is usually carried out at 10 pA with an inner diameter of 0.1 – 0.15 µm. The milling can then be carried out without an inner diameter at 5 kV and 48 – 16 pA until the protective Pt-layer is removed and the specimen is as sharp as possible. Final polishing can be carried out at lower currents, such as 2 kV, to remove Ga^+-ions that may have been implanted in the specimen during milling. The full lift-out and APT specimen preparation procedure as performed in the FIB/SEM system can be followed in Figure 3.5.

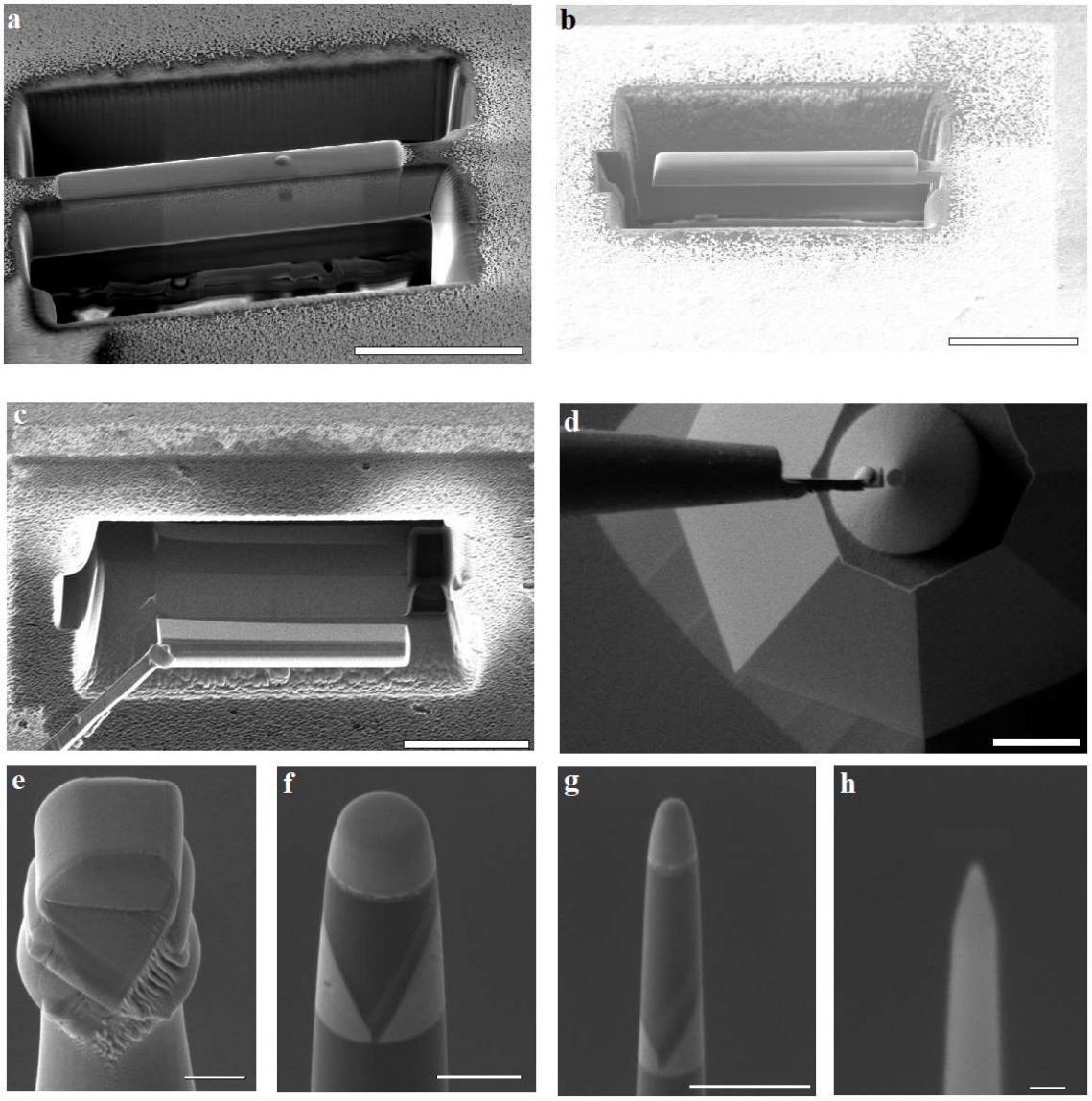


Figure 3.5: Procedure for preparation of APT specimens by FIB/SEM presented by SEM micrographs. ***(a)*** *Cantilever preparation for lift-out by milling of trenches along the long sides of the Pt-covered region of interest with the stage tilted to 30° with regard to the ion beam. Scale bar: 10 µm.* ***(b)*** *One short side of the lift-out milled away with the stage perpendicular to the ion beam. Scale bar: 10 µm.* ***(c)*** *Micromanipulator attached to the cantilever by Pt-deposition and remaining short side ion milled away. Step performed with the stage perpendicular to the electron beam. Scale bar: 10 µm.* ***(d)*** *~2 µm segments of the lift-out attached to flat-top micro-posts by Pt-deposition. Scale bar: 10 µm.* ***(e)*** *Segment of the lift-out after attachment to flat top post by Pt-deposition on both sides. Scale bar: 1 µm.* ***(f)*** *Specimen after initial annular ion milling has been performed. Scale bar: 1 µm.* ***(g)*** *APT specimen after further annular milling. The protective Pt-layer remains on the top. Underneath, the sputter coated gold layer can be observed, followed by the thin silica film region of interest. Scale bar: 1 µm.* ***(h)*** *Final APT specimen after finished preparation. Scale bar: 100 nm.*

TEM specimens were prepared similarly using a conventional FIB/SEM lift-out protocol [75]. A region of interest at the surface of the sample was covered by depositing a protective Pt-layer in a rectangular shape, usually with the dimensions 2 by 10 µm. The region of interest to be lifted out is separated from the rest of the sample by ion milling of two trenches along the long sides of the Pt-layer using a cross-section pattern with the sample oriented perpendicular to the ion beam. The sample is then tilted to a 52° and U-cut is made with the ion beam, leaving the lamella attached to the sample by only a small connect on one side. The micromanipulator is attached to the lamella by Pt-deposition and the lamella is cut free and lifted out. The lamella is then attached by Pt-deposition to a copper half grid (TED Pella) and made thinner by subsequent ion milling using a cleaning cross section pattern with decreasing ion currents until the protective Pt-layer is almost removed and the surface region of interest is sufficiently thin to be transparent for electrons at the energies used in TEM.

3.5. Characterization

TEM analysis was done using an FEI Titan 80-300 operating at 300 kV. Image analysis was performed with Gatan Digital Micrograph 3.

For chemical characterization with EDX, imaging was done in HAADF-STEM mode. EDX measurements were conducted with an Oxford X-sight detector (Oxford Instruments). Data analysis and quantification was performed using TEM Imaging & Analysis (TIA).

Image analysis was done using Gatan DigitalMicrograph and EDX analysis using TIA.

APT analysis was performed using several different instruments. The nanoHA covered titanium samples were analysed using a LEAP 5000 XS (CAMECA Scientific Instruments), with a UV laser operating at a wavelength of 355 nm. The laser pulse energy was varied between 65 and 95 pJ, calculated to have an effective pulse fraction of approximately 25%, according to the procedure where voltage required for a constant detection rate is measured as a function of the laser pulse energy [124][125]. The specimen temperature was set to 60 K and the target detection rate to 0.01 – 0.02 ions per pulse.

The femoral component of a knee explant and an as fabricated implant were analysed using a LEAP 6000 XR, with laser pulse energy of 100 pJ, specimen temperature at 50 K, pulse frequency up to 200 kHz, and a target detection rate of 0.005 to 0.01 ions per pulse. The instrument is equipped with a UV laser operating at a wavelength of 257.5 nm.

The silica embedded surfaces modified with AuNPs were analysed using a LEAP 3000X HR, equipped with a green laser operating at $\lambda = 532$ nm, and a LEAP 6000. In the LEAP 3000X HR system, the laser pulse energy was set to 0.2 – 0.3 nJ, the specimen temperature at 55 K and target evaporation rate at 0.002 ions per pulse. The pulse

frequency was set to 100 kHz. In the LEAP 6000 XR system, the pulse energy was set to 0.1 nJ, specimen temperature to 50 K, and target evaporation rate to 0.002 ions per pulse. In this system, the pulse frequency was automatically varied depending on the DC voltage, with the rate control set to 250 Da, to ensure that ions with that mass-to-charge-state ratio were properly detected before the next pulse.

The bulk silica samples with and without proteins were studied in **Paper V** and **Paper VII**, respectively, using the LEAP 6000 system over a range of analysis conditions. The laser pulse energy was varied between 0.25 pJ and 250 pJ, and the specimen temperature was mainly kept at 50 K. A specimen temperature range between 35 and 60 K was also explored. The detection rate was generally set to 0.005 ions per pulse and the pulse frequency was varied using the automated rate control to always allow ions with a mass-to-charge-state ratio of 250 to be detected before the next pulse, regardless of applied voltage.

The raw data acquired using LEAP 3000 and 5000 systems were reconstructed and analysed using IVAS 3.6.8 – 3.6.12 software (Cameca). The data obtained using the LEAP 6000 system was reconstructed and analysed with AP Suite 6.3 (Cameca).

In **Paper VI**, bulk silica samples were studied in a THz-laser assisted APT system developed at Groupe de Physique des Matériaux (GPM), Université Rouen Normandie. The THz pulses have an estimated maximum field amplitude between 5 and 20 V/nm and a repetition rate of 1 kHz. The comparatively lower pulse rate was compensated by adjusting the DC voltage to maintain a detection rate of 8% (0.08 ions per pulse).

4. Results and Discussion

In the following chapter, a summary of the results from the experimental work is presented.

4.1. Biomaterial characterization

4.1.1. Interfacial analysis of nanoHA on titanium

The nanoHA coated titanium samples were analysed using TEM and APT after chromium embedding and specimen preparation. From TEM, it was observed that the nanoHA layer was approximately 10 nm thick on top of the titanium surface oxide, as seen in Figure 4.1 a and b.

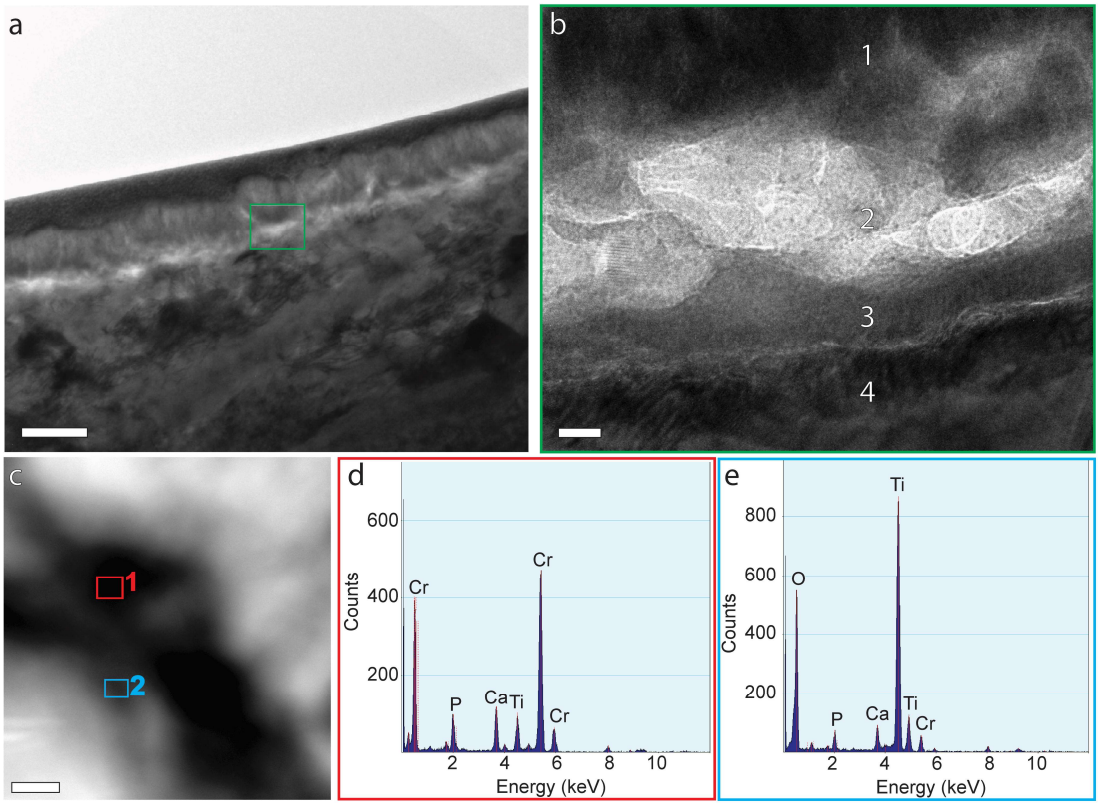


Figure 4.1: ***(a)*** *TEM overview obtained from a lift-out made from nanoHA-modified titanium substrate. The surface is covered with a sputter-coated protective chromium layer and a platinum layer deposited using GIS during specimen preparation. The green box highlights a part of the nanoHA coated surface. Scale bar: 200 nm.* ***(b)*** *TEM micrograph of area highlighted in (a). The labelled regions are 1: sputter-coated chromium layer, 2: nanoHA, 3: titanium surface oxide, 4: titanium substrate. Scale bar: 10 nm.* ***(c)*** *HAADF-STEM micrograph of an area similar to (b). The boxes indicate regions from which characteristic X-rays were collected for EDX analysis. Scale bar: 20 nm.* ***(d)*** *EDX spectrum obtained from region 1 in (c) with the major peaks labelled.* ***(e)*** *EDX spectrum obtained from region 2 in (c) with the major peaks labelled.*

The chemical composition of the different layers was assessed by collecting the characteristic X-rays generated in HAADF-STEM, see Figure 4.1 c. In the collected EDX spectra, signals corresponding to Ca and P are observed in both the chromium embedded nanoHA region and in the underlying titanium oxide, illustrated in Figure 4.1 d and e. In the APT analysis of the same material, the sputter chromium layer was found to be oxidized and at the interface between the chromium and titanium oxide, a thin layer of ions at 71 Da were detected which was identified as CaP. Inside the titanium oxide, small amounts of ions identified as hydroxyapatite related were detected. The reconstructed data from one such APT analysis is shown in Figure 4.2.

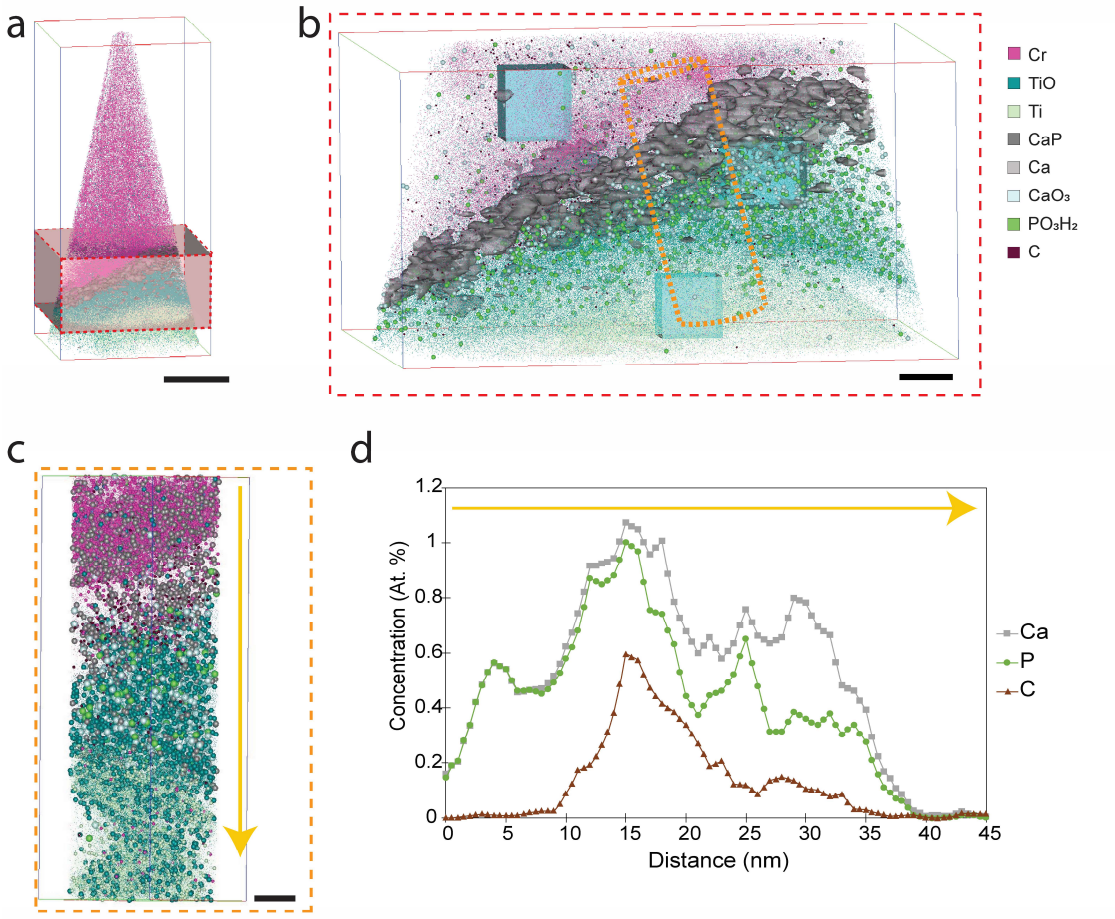


Figure 4.2: ***(a)*** *Reconstructed APT data from nanoHA coated titanium substrate embedded in chromium. The interface region is highlighted with a red box. Scale bar: 50 nm.* ***(b)*** *Analysis of the region highlighted in (a). An iso concentration surface set at 2% CaP (71 Da) is seen in grey. The three ROI-boxes were used to analyse the composition of the chromium, titanium oxide, and titanium regions, respectively. The orange cylinder was used to define a region for interfacial analysis. Scale bar: 10 nm.* ***(c)*** *Content of the region highlighted with an orange cylinder in (b) Scale bar: 5 nm.* ***(d)*** *1D concentration profile of the Ca, P, and C content in (d).*

The three regions, chromium, titanium oxide, and titanium were analysed by individual ranging of the mass spectra to avoid problems with overlaps in the mass spectra. In the

titanium oxide, ions were detected in the range 39-46 Da that could not be attributed to any titanium originating species, and were identifies as nanoHA related molecular ions such as PO_3^{++}, CaO_3^{++}, and similar with one or more H added. In other studies of nanoHA and chemically similar bone, detection of a variety of molecular ions are reported [126][127]. There are also possible overlaps in other parts of the mass spectrum, such as TiO_2^+ and $PO_3H_2^+$ at 81 Da, making quantification challenging. Overall, less calcium and phosphorous were detected using APT compared to EDX, possibly due to preferential evaporation and overlaps in the mass spectrum. 1D-concentration profiles were used to study the diffusion profile of calcium and phosphorous throughout the oxide layer. The Ca:P-ratio varied between analyses at different laser pulse energies, being lower at lower LPEs suggesting various degrees of preferential evaporation at the various electrostatic fields. The Ca:P-ratio measured using APT varies between analyses below and above the ratio obtained by EDX (1.3-1.47) and the theoretical stochiometric composition of hydroxyapatite. In bone, the mineral is often calcium deficient [128], and similar deficiencies can be expected for synthetic rod-shaped nanoHA [64]. In the 1D-concentration profile, carbon is found in a similar trend as calcium and phosphorous, since nanoHA prepared in solution forms carbonated hydroxyapatite, it some of the phosphate substituted with carbonate [129]. As carbon is not detected in comparable amounts in the chromium layer or underlying titanium, it is not attributed to APT specimen preparation.

Table 1: Measured bulk composition (atomic %) of the different regions highlighted in Figure 6.2 b, obtained by mass spectrum analysis of the reconstructed APT data.

Region	Cr (At. %)	Ti (At. %)	O (At. %)	Ca (At. %)	P (At. %)	C (At. %)
Chromium	71	-	28	0.2	0.2	0.01
Titanium oxide	-	45	53	0.6	0.3	0.1
Titanium	-	86	13	0.01	0.01	0.01

In a previous study on the interface between bone and a titanium implant, a calcium-enriched region was observed on the outer surface of the implant [130]. This tendency was not observed in the nanoHA coated titanium, and it is suspected that the heat treatment during material manufacturing provides enough energy for both calcium and phosphorous to diffuse through the entire oxide layer. While quantification of calcium and phosphorous at these low concentrations at the nanoscale are associated with challenges both using EDX and APT, the analyses confirm the presence of these elements throughout the titanium oxide and that this material already show resemblance of osseointegration prior to use in an implanted medical device.

4.1.2. Photothermal gold nanorods

For the photothermal biomaterial system, the AuNRs were characterized using TEM, to determine the size distribution of the rods as well as the orientation of the crystal lattice with regard to the nanorod aspect.

High resolution TEM (HRTEM), as seen in Figure 4.3, confirms that the nanorods are single-crystalline with the characteristic fcc gold lattice. The observed lattice spacing along as well as perpendicular to the long axis of the nanorods corresponds well to the expected distance of 2.03 Å in (200)-type planes.

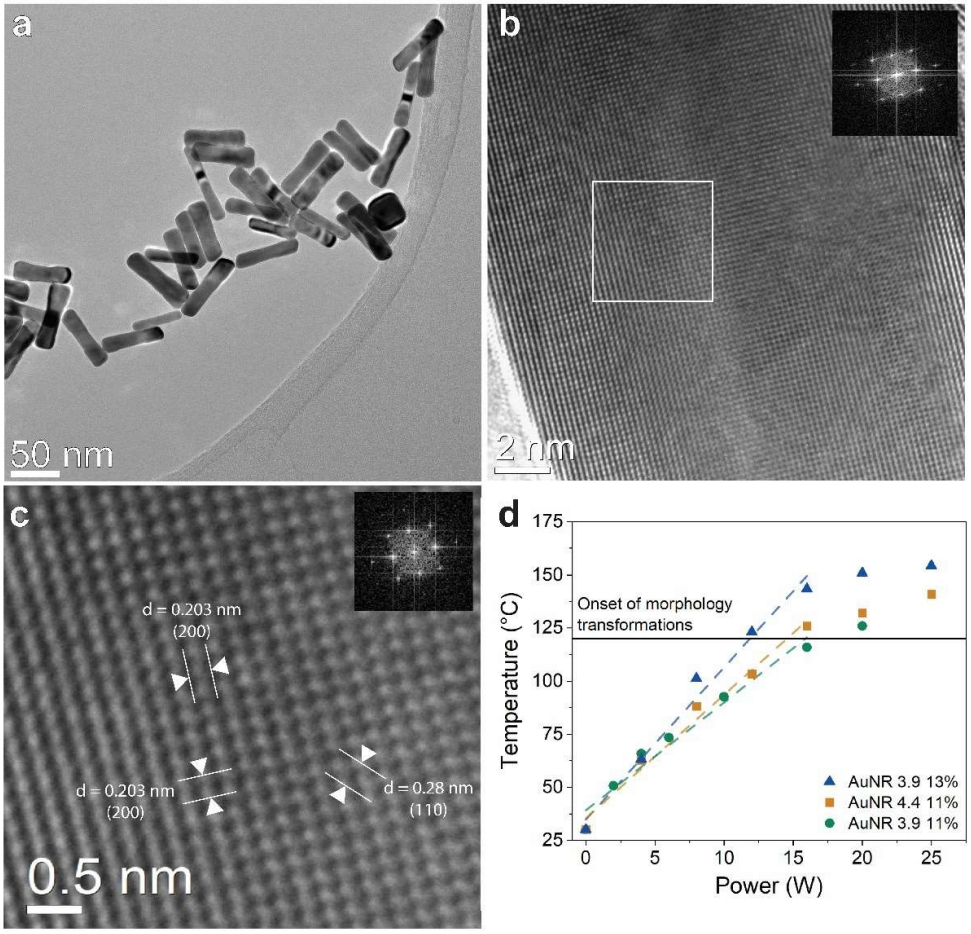


Figure 4.3: ***(a)*** *TEM micrograph showing an overview of gold nanorods, used for determination of particle size and shape distribution. Scale bar: 50 nm.* ***(b)*** *Higher magnification TEM micrograph of a single gold nanorod. FFT insert indicate the single crystal nature of the nanorods. Scale bar: 2 nm.* ***(c)*** *HRTEM micrograph of the region highlighted with in (b). Lattice fringes in parallel and perpendicular to the long axis of the nanorod show good agreement with the (200) planes in gold. Scale bar: 0.5 nm.* ***(d)*** *Temperature as a function of laser power determined from comparison of lattice parameter with thermal expansion of gold for three AuNR samples with varying aspect ratios and surface coverage.*

The photothermal effect was demonstrated using *in-situ* XRD heating experiments, in which the AuNR immobilized on glass substrates were NIR heated under constant illumination of an 808 nm laser. By following the shift of (200) peak, the temperature increase could be studied, caused by the thermal expansion of the material and increase of the lattice parameter. Using a calibration curve obtained by heating identical samples in an oven while following the shift of the (200) peak, a linear correlation between the increase in temperature and the NIR laser power was observed. This trend last up until 120 °C, at which an onset of morphological changes of the nanorods was observed.

4.1.3. Oxide formation on ZrN multilayered implant material

The femoral component of the knee explant and an as-fabricated implant were compared to study the effect on the surface of two years of use, and how this differs between the articulating area, meaning in contact with the polyethylene gliding surface, and non-articulating area. The surface features and underlying multilayer structure of the samples were studied using TEM. Between the samples, no difference was observed in the top ZrN layer, intermediate CrCN/CrN layers or the Co base metal. However, differences were observed in the thickness of the surface oxide. In Figure 4.4, the overview and differences in the surface oxide layer are presented.

In the as-fabricated implant, the surface oxide layer is a few nanometres thin, which is consistent with other reports in literature on native oxide formed on ZrN [131][132]. In the explant, the oxide layer in the articulating area was observed to be formed of patchy regions, up to 25 nm thick, connected by a few nm thin layer. In the non-articulating area on the other hand, the oxide layer was a 30-50 nm film that appeared comparatively more continuous.

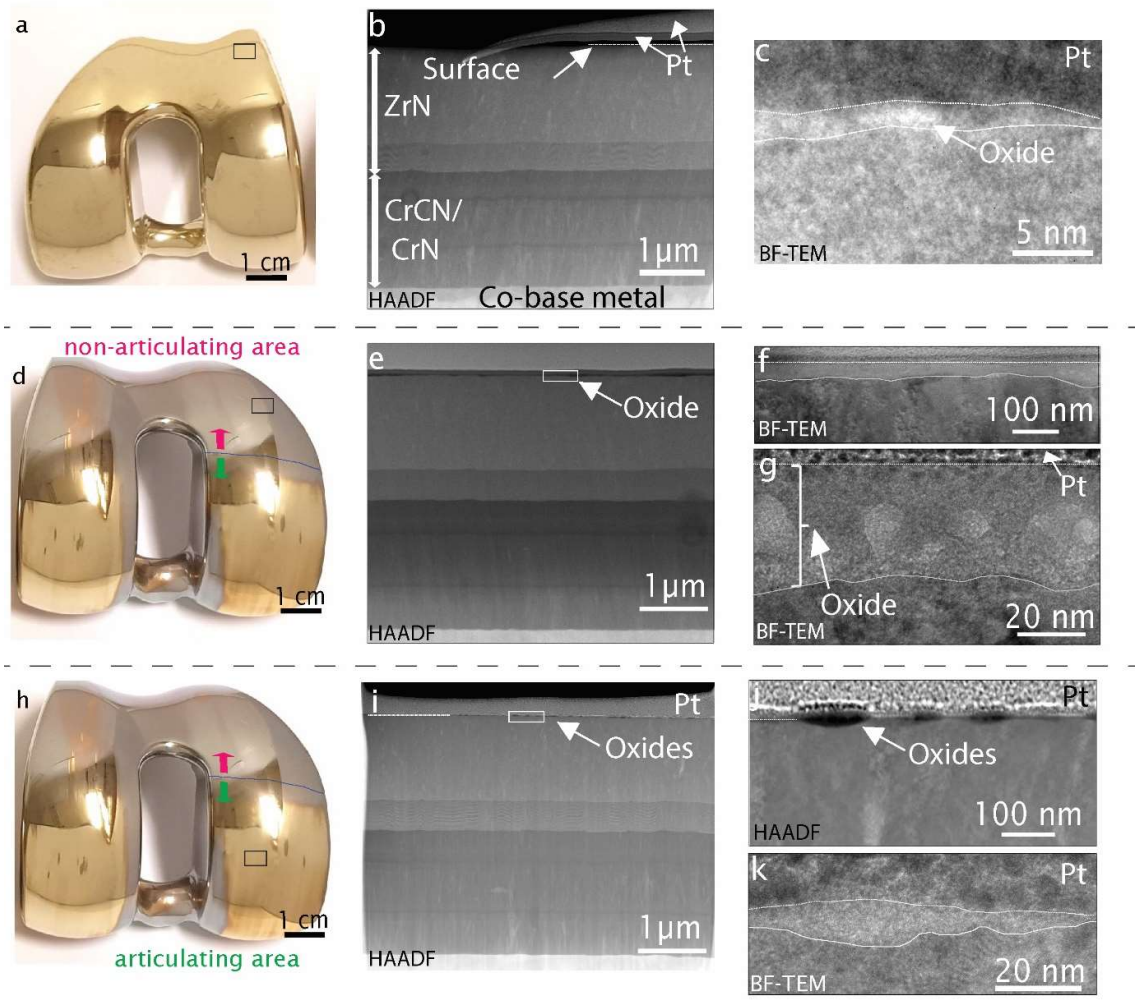


Figure 4.4: ***(a)*** *Photograph of as-fabricated implant. Black box indicates area used for TEM and APT lift-outs.* ***(b)*** *TEM overview of the multi-layered surface of the as-fabricated implant.* ***(c)*** *Close of the surface oxide of the as-fabricated implant.* ***(d)*** *Photograph of explant. Black box indicates region from the non-articulating area used for TEM and APT lift-outs.* ***(e)*** *TEM overview of the multi-layered surface of the non-articulating area of the explant.* ***(f)*** *and* ***(g)*** *Close up of the surface oxide in the non-articulating area of the explant.* ***(h)*** *Photograph of explant. Black box indicates the region from the articulating area used for TEM and APT lift-outs.* ***(i)*** *TEM overview of the multi-layered surface of the articulating area of the explant.* ***(j)*** *and* ***(k)*** *Close up of the surface oxide in the articulating area of the explant.*

By EDX, the composition of the oxide was estimated, shown in Figure 4.5. Elemental mapping of the oxide layer in the non-articulating area indicated that the oxygen concentration in the layer was approximately 40-50 atomic %, while closer to zero in the underlying ZrN layer. The decrease of oxygen was compensated by a corresponding increase in Zr, while the N concentration appeared rather consistent between the oxide and ZrN layer. However, it should be noted that EDX quantification of light elements is challenging and prone to underestimation [72], and the results taken as a more qualitative indication of the relative presence of elements in different regions. From the TEM analysis, the microstructure of the oxide layers was also investigated. Within the

oxide on the explant, fast Fourier transforms (FFTs) were used to study the nature of the oxide. Ring-like patterns were observed, indicating amorphous regions of the oxide, together with some regions where diffraction spots were observed in the FFTs, suggesting the presence of some nanocrystalline regions. The nanocrystalline areas appear to generally be closer to the ZrN-oxide interface rather than the surface.

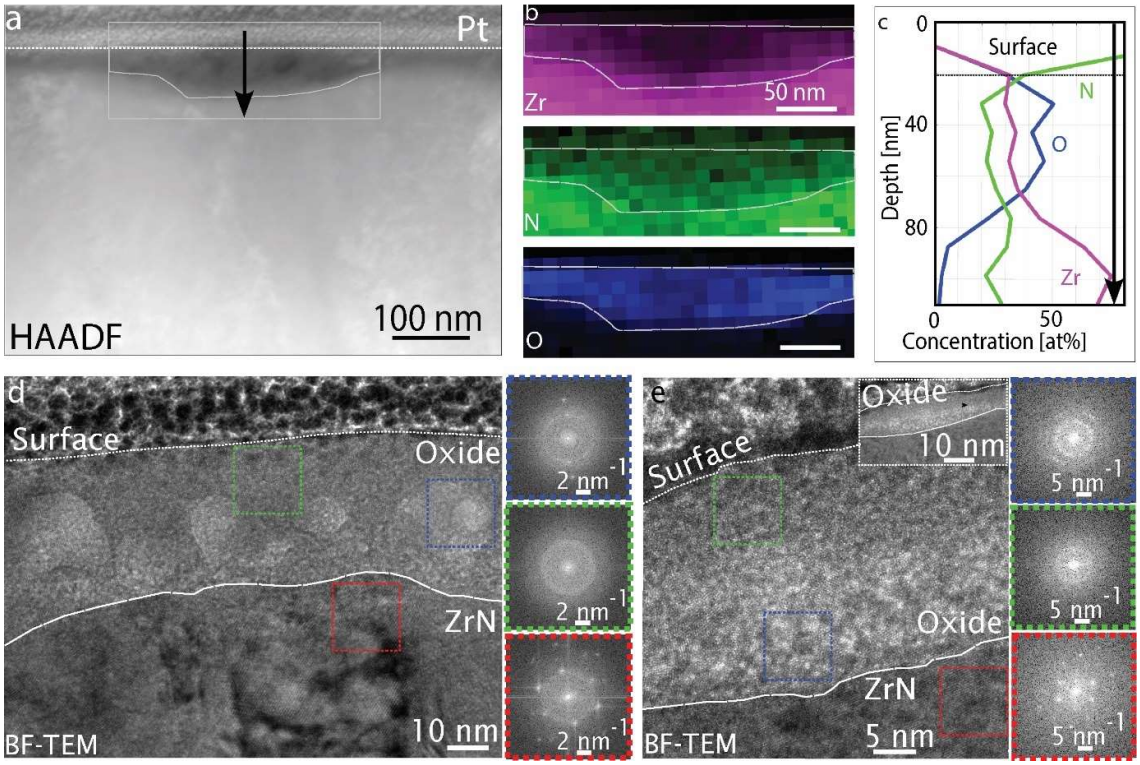


Figure 4.5: ***(a)*** *HAADF-STEM overview of the non-articulating area of the explant. The white box hightlights the region used for EDX-mapping and the black arrow for the line scan.* ***(b)*** *EDX-map from the area marked in (a) for Zr, N, and O.* ***(c)*** *Element concentration profile of Zr, N, and O following the black arrow in (a).* ***(d)*** *TEM micrograph of the surface oxide in the non-articulating area. Boxes indicate areas used for the FFT inserts.* ***(e)*** *TEM micrograph of the surface oxide in the articulating area. Boxes indicated regions areas used for the FFT inserts.*

APT analyses of the as-fabricated implant and articulating area of the explant were performed to study the oxide layer, shown in Figure 4.6 a-c, and d-g, respectively. In the as-fabricated implant with the thin oxide layer, oxygen was detected at the sample surface at up to 5 atomic %. As the oxide was only a few nm thin, However, it should be noted that oxide stoichiometry is unreliable to measure with APT, due to losses of oxygen, especially at lower electrostatic fields [133][134]. It was found that the oxygen containing region extended from the surface into the bulk with finger-like structures, which can indicate the presence of a grain boundary with dislocation pipes decorated with oxygen [135][136]. While the thickness of the oxide layer and the quantitative oxygen

content can be challenging to assess with APT, the presence of such finger-like features would not be detected with other techniques.

In the reconstruction of the articulating area of the explant, the surface oxide appeared be approximately 20 nm thick and up to 50 atomic % oxygen was detected. Challenges were associated with the quantification of oxygen due to overlaps in the mass spectrum of the various ZrN and ZrO isotopes.

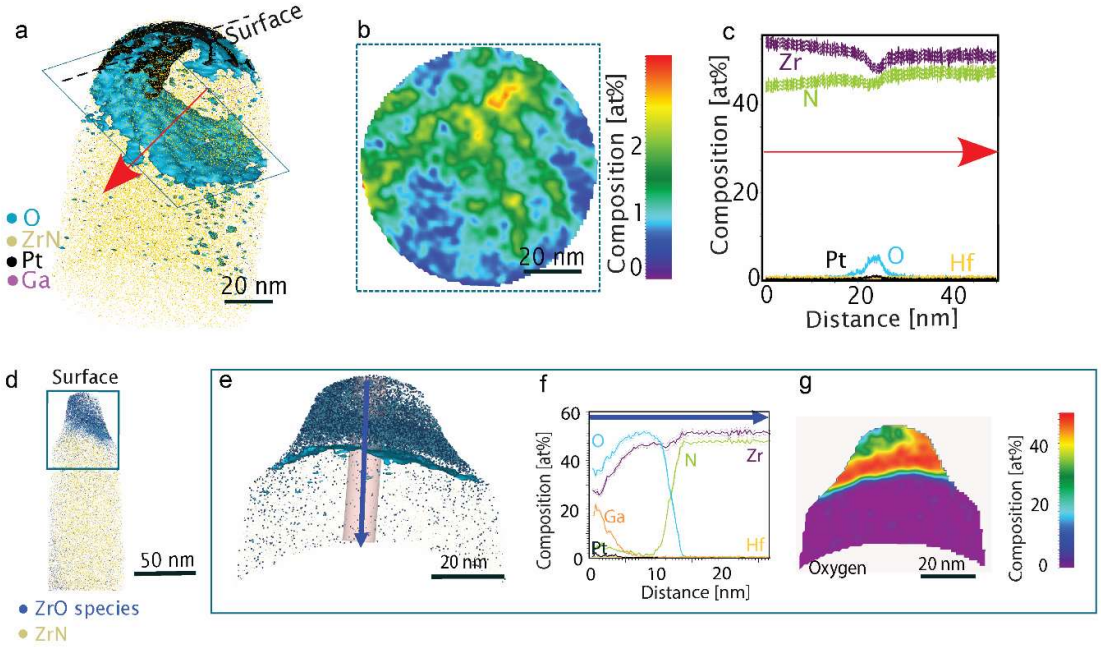


Figure 4.6: ***(a)*** *Reconstructed APT data obtained from the as-fabricated implant. The surface covered by a Pt capping layer is indicated with a black dashed line. The surface oxide is visualized by a 2 atomic% oxygen iso concentration surface in blue with finger like features perpendicular to the surface.* ***(b)*** *2D oxygen composition map of the region indicated by the blue rectangle in (a). The finger-like surface oxide features are clearly visible.* ***(c)*** *1D concentration profile along the red arrow in (a), intersecting the surface oxide features.* ***(d)*** *Reconstructed APT data from the explant's articulating area.* ***(e)*** *5 nm thin slide of the first 2 million ions from the APT data in (d).* ***(f)*** *1D concentration profile along the cylinder ROI shown in (e), following the direction shown by the blue arrow.* ***(g)*** *2D oxygen composition map of the atom map slice in (e).*

The APT analysis of the non-articulating area was not reliable due to high degree of Ga contamination. The reason for Ga damage is suspected to be the poor adhesion of the sputter coated protective layers to the sample surface, as it was prone to spall off during APT specimen preparation. The capping layer itself was not detected in any APT analysis of the explant, beam damage appeared to be significant based on the Ga implementation, and the specimens were prone to microfractures in the oxide. Based on this, the entirety of the oxide from either the articulating or non-articulating area of the explant was likely not captured.

All in all, the explant was shown to have an oxide layer very different from the as-fabricated implant and different than expected from native oxidation. The differences in the oxide's nature between the articulating and non-articulating area of the explant suggests different origins. The oxide in the non-articulating area is suspected to be due to static oxidation from the corrosive environment without mechanical influence, giving the continuous ~50 nm thick oxide layer. In the articulating area, the patchy nature of the oxide is suspected to be of tribological origin, as the oxide can grow faster through this process [135]. As the articulating area is in contact with the gliding surface, particles embedded in the surface can remove the formed oxide on the ZrN, introducing new defects, which will allow for continued oxidation. This can explain the patchy nature of the oxide, while the thin oxide film between the patches can be the result of native oxidation after the removal of the implant.

4.2. Silica embedded gold nanostructured surfaces

Gold nanoparticles were attached to the surface of chromium coated silicon wafers and the surface coverage assessed by SEM prior to silica embedding, illustrated in Figure 4.7 a. After silica embedding, the material was studied by TEM, revealing the proper embedding of the nanostructured surface in an approximately 200 nm thick amorphous silica film, as seen in Figure 4.7 b. The surface coverage of AuNP with an average distance between the particles of approximately 60 nm proved to be sufficient for a reasonably high likelihood of having a nanoparticle within any given APT specimen.

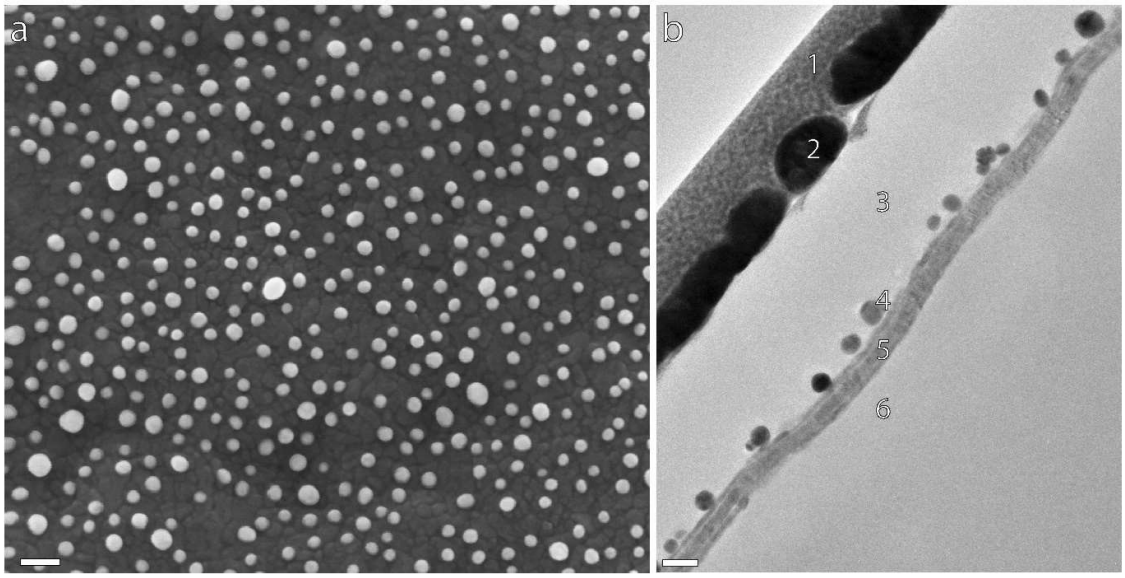


Figure 4.7: ***(a)*** *SEM micrograph of a chromium coated silicon wafer covered with gold nanoparticles. Scale bar: 100 nm.* ***(b)*** *TEM micrograph of a lift-out from the material in (a) spin-coated with a silica film. Labelled regions are 1: GIS-deposited protective platinum layer, 2: sputter-coated protective gold layer, 3: spin-coated silica film, 4: Gold nanoparticle, 5: Chromium layer, 6: Silicon substrate. Scale bar: 50 nm.*

The AuNPs embedded silica film in a silica film provided a clear region to target during APT specimen preparation, making it possible to prepare tips with the NP containing region of interest close to the apex.

APT analyses generally gave a modest number of silica originating ions before gold was detected, often together with chromia related ions. The dielectric nature of silica, exhibiting a relatively high evaporation field and effective k factor [137], can explain the lack of silica originating ions detected. The magnification in APT analysis is higher for such a material, causing relatively more ions to be lost outside the field of view. The poor conductivity will also cause the electrostatic field to be the highest at the highest at the base of the silica film, making it a weak spot where the specimen could be prone to fracture. The interface between the silica and gold nanoparticles is presumably weak and may delaminate upon the application of the required standing voltage to reach field evaporation. This is consistent with the observations as silica is absent in the analyses, and the gold nanoparticles appear early on, often after a burst of ions. In the analysed gold nanoparticles, silver was detected at around 2 – 4 atomic % of gold evenly distributed in the particles, as seen in Figure 4.8 b. This is lower than the theoretical maximum amount based on the synthesis protocol, suggesting that some silver is lost during NP synthesis, or by preferential evaporation due to the lower evaporation field of silver compared to gold [81].

The nanoparticle shape often appeared distorted in the reconstructions, deformed (squeezed) and surrounded by chromium oxide. This shape is reminiscent of reports on particles and precipitates surrounded by a material with a higher evaporation field [138], but could be adjusted to obtain a more spherical particle shape by reduction of the reconstruction factor, k. None of the detected AuNPs had the number of gold atoms corresponding to nanoparticles of the average diameter determined by SEM. This suggests that only parts of the nanoparticles were captured within the APT specimens and the field of view of APT analysis. The reconstructed AuNPs were also smaller than expected, however it should be noted that the size of different features in APT reconstructions is also determined by the reconstruction parameters used. The density of collected ions were higher in the regions corresponding to AuNPs and this can contribute to the smaller than expected size by the local magnification effect [139], were the magnification is reduced in region with lower evaporation fields compared to the surrounding.

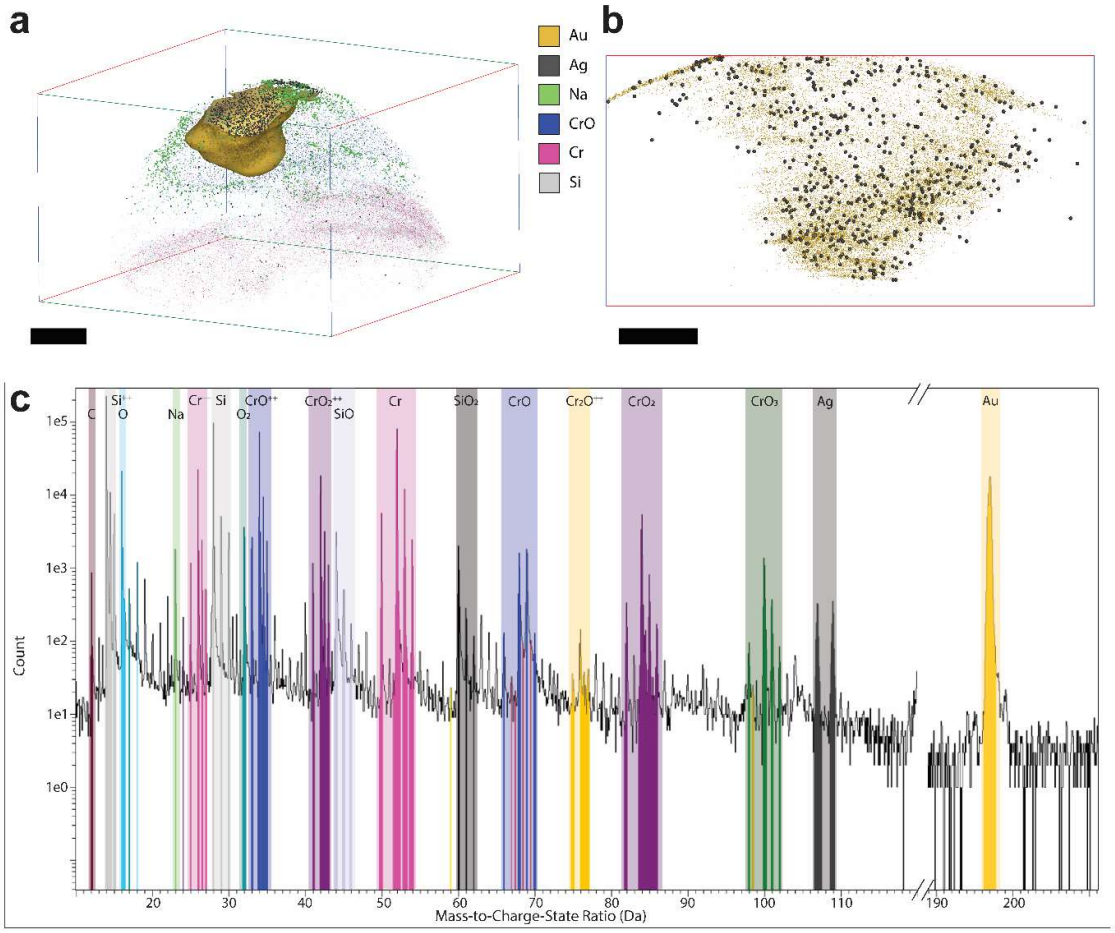


Figure 4.8: ***(a)*** *Reconstructed APT analysis of silica embedded AuNP with the reconstruction factor k set to 3.0. Gold iso-concentration surface set to 15 atomic %. Scale bar: 10 nm.* ***(b)*** *Cross section of the gold nanoparticle in (a), silver ions highlighted as spheres. Scale bar: 5 nm.* ***(c)*** *Mass spectrum from the APT analysis with the major peaks highlighted. Ions without a specified charge are in the first charge state.*

On the surface of the nanoparticles, sodium was detected at a mass-to-charge-state ratio of 23 Da. This indicates that it can be possible to study ligands on nanoparticles using this method, as sodium nitrate was used in the synthesis to stabilize the nanoparticles. However, the origin of the sodium is uncertain as it was also present in the sol-gel used for silica embedding. The reason for the gold nanoparticles appearing to be embedded in chromia in the APT results can be explained by the suspected delamination of the silica film, as this would leave the chromium layer exposed. At the edges of this layer, the local field may be sufficiently high to cause field evaporation simultaneously as the evaporation of the AuNP. The molecular ions detected from the chromia, predominantly CrO^{++} and CrO_2^{++} is consistent with previously reported findings [140], and suggests a rather high local electrostatic field. In deep-UV laser assisted APT analysis of these samples, similar results were obtained. Interestingly, carbon was detected in the vicinity

of the AuNPs and sodium, also suggesting that the stabilizing sodium citrate ligands could be studied.

Samples were also prepared where proteins were attempted to be bound to the nanoparticles using thiol modified streptavidin and biotin-tagged gold nanoparticles with a diameter of 6 nm. SEM imaging prior to silica embedding and TEM imaging after the embedding showed the smaller nanoparticles next to the larger, surface bound, nanoparticles with a distance between in good agreement with the size of the streptavidin-biotin bond [141], show in Figure 4.9. However, in APT analysis of these samples, no two gold nanoparticles with a protein link between them were observed. Nevertheless, the studies of silica embedded AuNP modified surfaces indicate that nanostructured surfaces can be studied using APT, possibly with stabilizing ligands retained in their hydrated state as silica formed by a sol-gel process replaces the water.

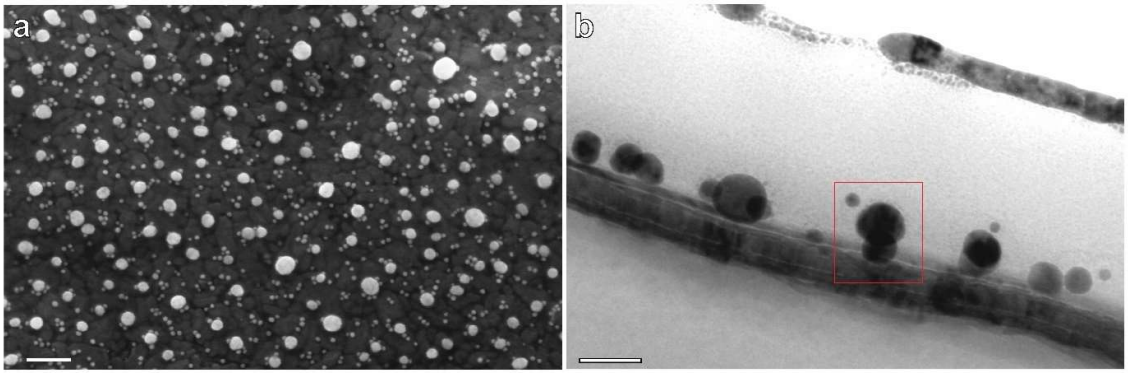


Figure 4.9: ***(a)*** *SEM micrograph of a chromium coated silicon wafer, nanostructured with AuNPs with a diameter of approximately 30 nm, subsequently modified with thiol-tagged streptavidin and biotinylated AuNPs with a diameter of 6 nm. Scale bar: 100 nm.* ***(b)*** *TEM micrograph of a lift-out from the surface in (a) spin-coated with a silica film. In the highlighted region, the distance between the larger and smaller nanoparticles is in good agreement with the size of the streptavidin-biotin complex. Scale bar: 50 nm.*

4.3. Deep-UV and THz laser assisted analysis of bulk silica

The properties, mainly determined by the porosity, of the silica samples synthesized from alkaline silicate precursors could be tuned by adjusting the pH of the solution as well as the concentration. The porosity of the material was assessed by specific surface area measurements using nitrogen physisorption. The general trend seems to be that silica prepared with the solution adjusted to a pH close to physiological levels has larger pores and lower specific surface area, while when the pH is adjusted to lower levels, the pores are smaller and the specific surface area higher. This is illustrated in Figure 4.10. The trends for different sodium silicate concentrations are not as clear but lower concentrations appear to give even smaller pores and higher surface area. This is thought to be due to higher concentrations and pH closer to 7 causes the solution to gel quicker, and the silica network formed will not be as dense but can also be related to

other effects of the pH dependent nature of the condensation polymerization. The results also follow previously established behaviour, where amorphous silica synthesised from alkoxysilanes such as TEOS forms denser glasses when hydrolysed under acidic conditions due to the formation of Si-OH monomers that polymerize in more linear polymers [113].

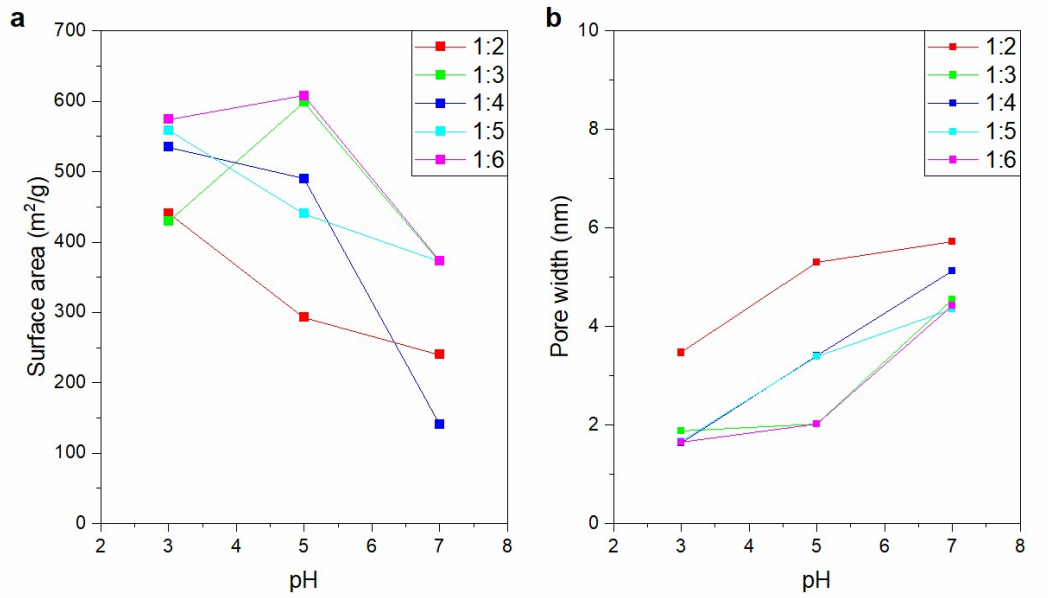


Figure 4.10: ***(a)*** *Specific surface area measured by nitrogen physisorption and calculated by the BET method for silica samples synthesised at various pH levels and with various sodium silicate stock solution to water ratios.* ***(b)*** *Pore width measured by BJH adsorption for the samples in (a).*

The isotherms for surface area measurements show characteristic features materials with both micropores and mesopores. Hysteresis loops are present, as can be seen in Figure 4.11 a, typical for silica gels and porous glasses, which can be interpreted as originating from pores with narrow necks and wide bodies, however network effects should also be considered for this behaviour [142][143]. The average micropore width of a typical silica sample was around 7 Å, shown in Figure 4.11 b.

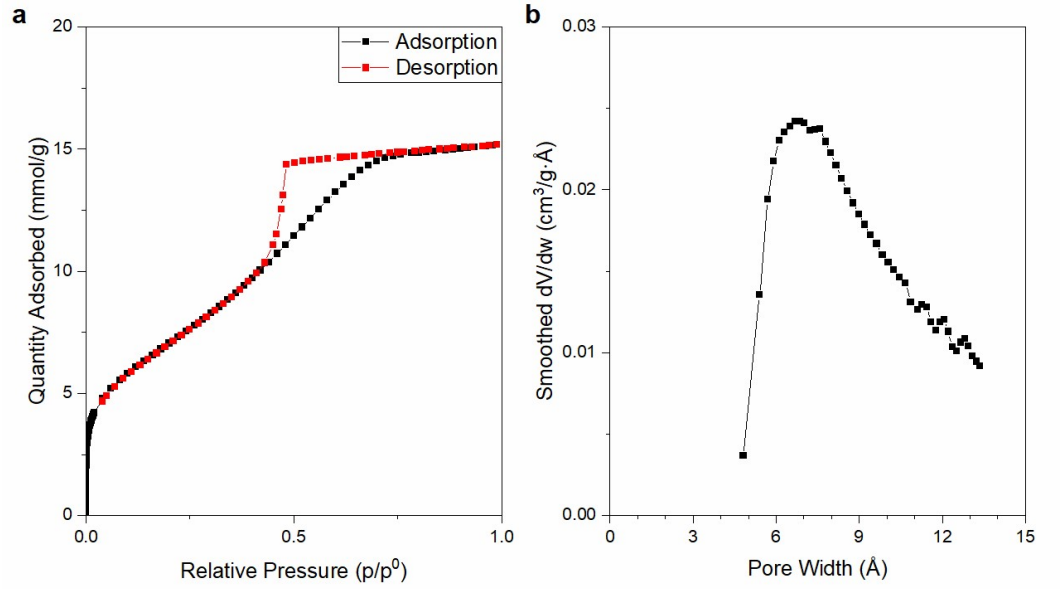


Figure 4.11: ***(a)*** *Full isotherm from nitrogen physisorption measurement of a representative silica sample.* ***(b)*** *Micropore width distribution demonstrated by differential pore volume obtained by the Horvath-Kawazoe method.*

Bulk silica samples have proven to be challenging to study by APT as the analyses would often end by premature specimen fracture early on in the measurements, after collection of only a few hundred thousand of ions. This issue has persisted over several generations of laser assisted APT instruments, equipped with lasers using wavelengths from green to UV. But eventually, bulk silica was successfully analysed using the deep-UV laser assisted APT of the LEAP 6000 system, in which several tens of millions of ions could be collected in one single analysis before specimen fracture. Measurements were performed over a range of analysis conditions, with specimen temperatures ranging from 35 to 60 K and laser pulse energy from 0.5 to 250 pJ. The improved yield is attributed to the silica's higher absorption of the laser at these wavelengths compared to longer ones. This increases the temperature of the specimen more effectively, reducing the required voltage to reach the evaporation field, and consequently allows for more ions to be collected before the specimen fracture from voltage induced mechanical stresses.

In general, during measurements with a LEAP instrument, a target detection rate is set, by which the system is programmed to adjust the applied voltage to maintain a certain detection rate of for example one ion detected every 200rd pulse. Despite this, the actual detection rate proved to be uneven in the analyses of bulk silica, often instantaneously increasing above five times the target rate and occasionally to above ten or twenty times the target rate. Such spikes in evaporation rate and bursts of collected ions can be attributed to microfractures in the specimen during analysis, when a piece of the tip breaks off due to mechanical stresses caused by the strong electrostatic fields. They can

also be, at least partly, explained by the presence of micropores in the material. As a pore is encountered in the specimen during analysis, the electrostatic field experienced by the surface atoms surrounding the pore will increase, as the effective specimen radius decreases, causing a burst of field evaporated ions. As the system automatically adjusts the applied voltage to maintain the set target evaporation rate, such a burst of ions will cause a decrease in the applied voltage as a response. This causes an uneven voltage profile during analysis, preventing the use of the voltage profile to correctly define the specimen radius during data reconstruction.

Mass spectrum analysis of silica samples showed that the major peaks are Si^{++} at 14 Da and O^{+} at 16 Da. The signal at 16 Da is identified as O^{+} rather than O_2^{++} [144]. Other silica originating ions detected in lower amounts include Si^{+}, O_2^{+}, SiO^{+} and SiO_2^{+}. Ga, Pt, and C originating from the FIB/SEM specimen preparation process were also detected throughout all silica analyses and appear as clusters in the reconstructed data. This suggests that the platinum mixture used to weld the lift-out to the flat-top posts can fill the micropores of the silica during specimen preparation. Platinum and carbon can be detected on the side of the specimen during analysis, indicating that the weld can be heated by the laser and diffuses up to the surface of the tip and gets evaporated there. Sodium is detected as well, which is to be expected given the sodium silicate precursor used to form the silica. However, the spatial distribution of sodium in APT measurements is unreliable, as redistribution due to the electrostatic field of easily ionized and mobile alkaline atoms is a known phenomenon [145]. An atom map reconstructed from an APT analysis of bulk silica is shown in Figure 4.12, together with the corresponding mass spectrum.

The measured silica composition varies with the electrostatic field indicated by the charge-state-ratio (CSR) of ^{28}Si in the first and second charge state. It has previously been established that the detected amount of oxygen increases with higher electrostatic fields [133], and this trend is observed between different analyses of specimens from the same lift-out at various LPEs. As the evaporation field is temperature dependent, a higher DC voltage is required to maintain a desired evaporation rate at lower specimen temperatures and LPEs. For the studied silica samples, this effect is clear regarding the LPE as the measured O/Si-ratio decreases with increasing LPE, but not as obvious when comparing specimen base temperature.

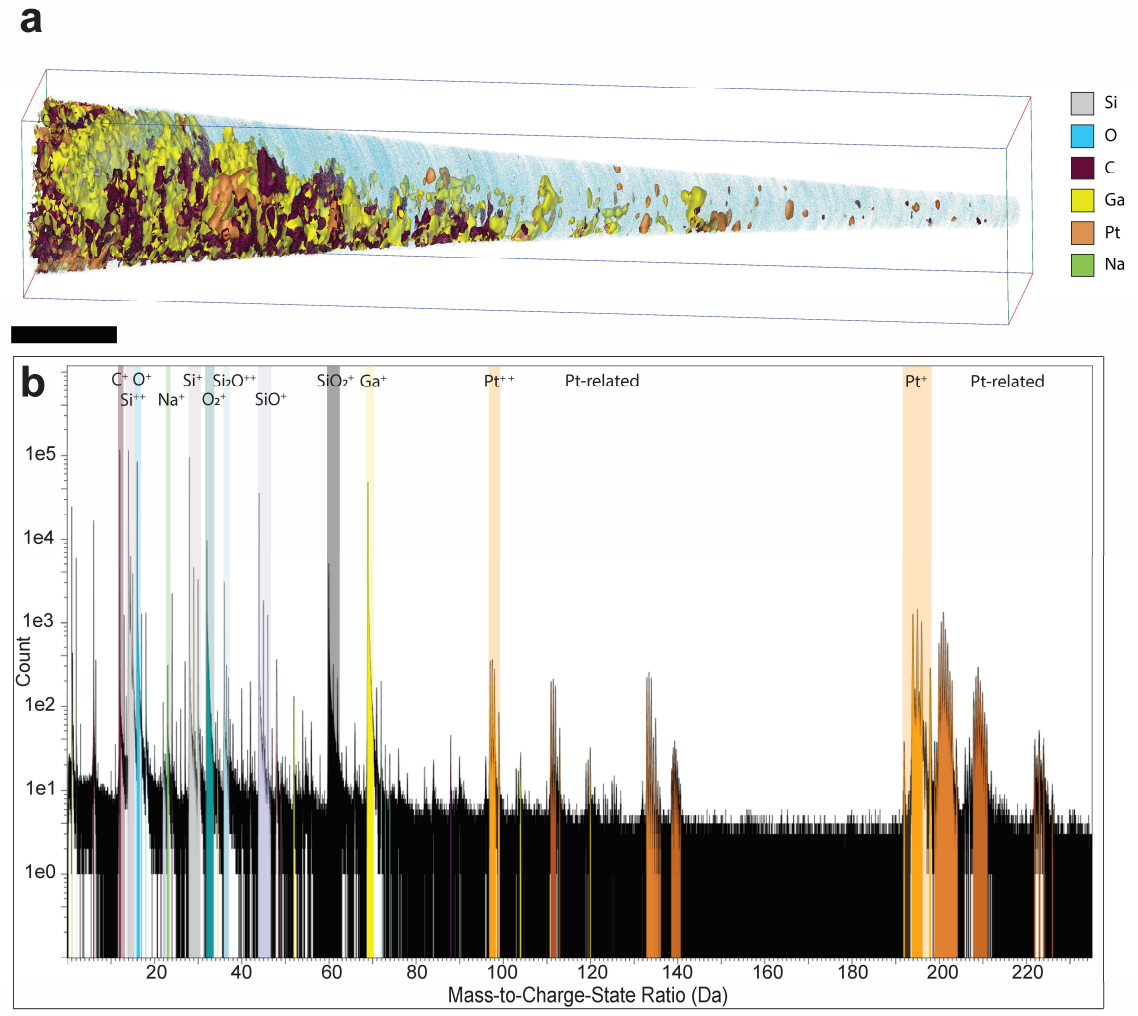


Figure 4.12: ***(a)*** *Atom map reconstructed from APT analysis of bulk silica. Silica originating species displayed as points. C, Ga, and Pt originating from the FIB/SEM specimen preparation are shown as iso-concentration surfaces set to 20, 13, and 16 atomic %, respectively. Scale bar: 50 nm.* ***(b)*** *Mass spectrum obtained from the APT analysis used for the reconstruction in (a) with the identification of the major peaks shown.*

It seems that the heating effect of the laser pulses is stronger than that of the specimen stage, given the isolating properties of silica. When the specimen temperature is higher, there is an increased probability of ions evaporating slightly after the laser pulse before the specimen has cooled down, causing the increased time between the pulse and detection to give a higher measured mass-to-charge-state ratio. This effect gives so called thermal tails in the mass spectrum. As seen in Figure 4.13, the thermal tails are expected more prominent at higher LPEs. However, the peaks are still clearly distinguishable and the mass resolving power measured as the full-width-half-maximum is constant over the explored range of LPEs, while the background is higher at lower LPEs. Comparisons of data between different APT analyses should be done with some caution, as the specimen tip shape is also known to influence the results of

APT measurements [146]. For example, the somewhat outlaying behaviour of the specimen analysed at 150 pJ and 50 K could be explained by a different tip shape or a different degree of specimen damage during FIB/SEM preparation.

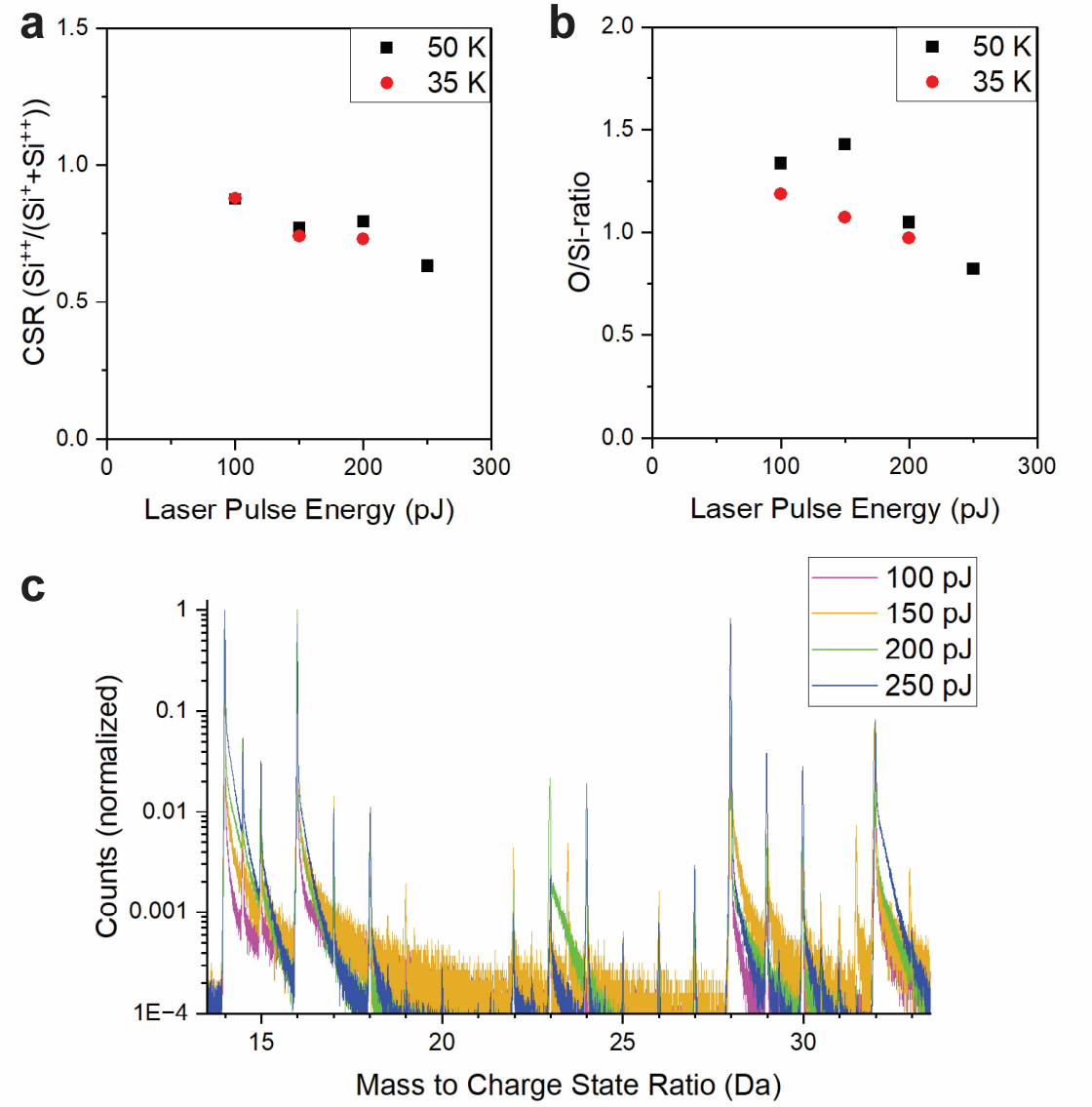


Figure 4.13: ***(a)*** *The measured charge-state-ratios of $^{14}Si^{++}$ and $^{28}Si^{+}$ from different APT analyses at various laser pulse energies and specimen temperatures.* ***(b)*** *The measured oxygen to silicon ratio in the APT analyses.* ***(c)*** *Comparison of the normalized mass spectra between 13.5 and 33.5 Da, obtained from the APT analyses in (a) with the specimen temperature set to 50 K.*

When using deep-UV laser assisted APT to study metallic materials, such as steels, LPEs below 25 pJ are generally not usable as the signal-to-noise ratio gets too low. However, the silica specimens were successfully analysed with LPEs as low as 0.5 pJ, indicating that the absorbance of the laser is better than for other materials with higher reflectivity. In the obtained data at the lowest LPEs, no Ga and Pt was detected, and the

specimens fractured earlier. This suggests that the laser pulse is insufficient to heat Ga and Pt enough to achieve field evaporation while the silica absorbs the photons more efficiently. Comparing the obtained data at LPEs between 25 and 0.5 pJ, similar trends regarding increasing CSR of Si, O/Si-ratio, and reduced thermal tails when decreasing the pulse energy were observed as at higher LPEs.

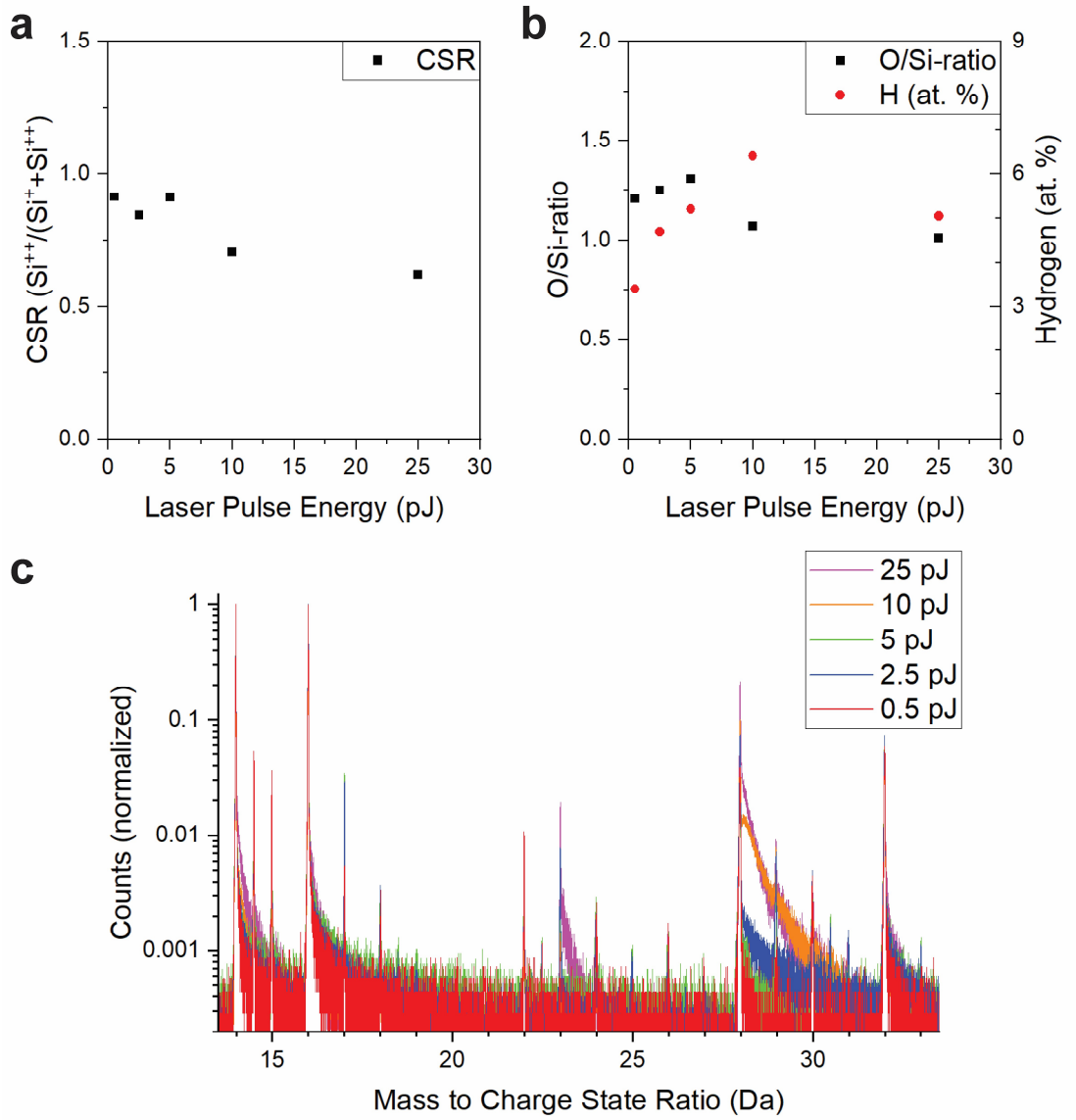


Figure 4.14: ***(a)*** *The measured charge-state-ratios of* $^{14}Si^{++}$ *and* $^{28}Si^{+}$ *from different APT analyses at various low laser pulse energies.* ***(b)*** *The measured oxygen to silicon ratio and detected amount of hydrogen from the APT analyses in (a).* ***(c)*** *Comparison of the normalized mass spectra between 13.5 and 33.5 Da, obtained from the APT analyses in (a).*

At the lowest LPEs, the thermal tails disappear almost completely and the CSR as well as the O/Si-ratio and detected amount of hydrogen stabilizes somewhat, as seen in Figure 4.14. The detected amount of hydrogen can also be indicative of the electrostatic field at the specimen apex [85][86]. It can be speculated that field evaporation of silica in

deep-UV laser assisted APT at these photon energies, 4.8 eV, is not only a thermal effect, but also that the photon energy can excite the surface atoms to a higher energy state from which they field ionize or are directly photoionized.

Silica samples synthesised from sodium silicate precursors were also analysed using an experimental APT setup equipped with a laser in the THz range. The lower pulse frequency caused a higher amount of hydrogen detected, as residual gases in the chamber will adsorb to the specimen to a higher degree between pulses. The THz system allows for selection of pulses with positive or negative polarity to be focused on the sample. Using negative pulses, the same silica originating ion species were detected as with the deep-UV laser assisted system, Si^{++}, O^+, Si^+, O_2^+, SiO^+, Si_2^+, and SiO_2^+. Carbon was detected in the first and second charge state, as well as sodium. With positive THz pulses, only hydrogen and Si^{++} was detected above the higher background level. At positive pulses, it seems that mainly static evaporation from the applied voltage and thermally assisted evaporation occur and that the direct interactions between the THz pulse and the specimen are negligible. The comparison of the obtained data is shown in Figure 4.15.

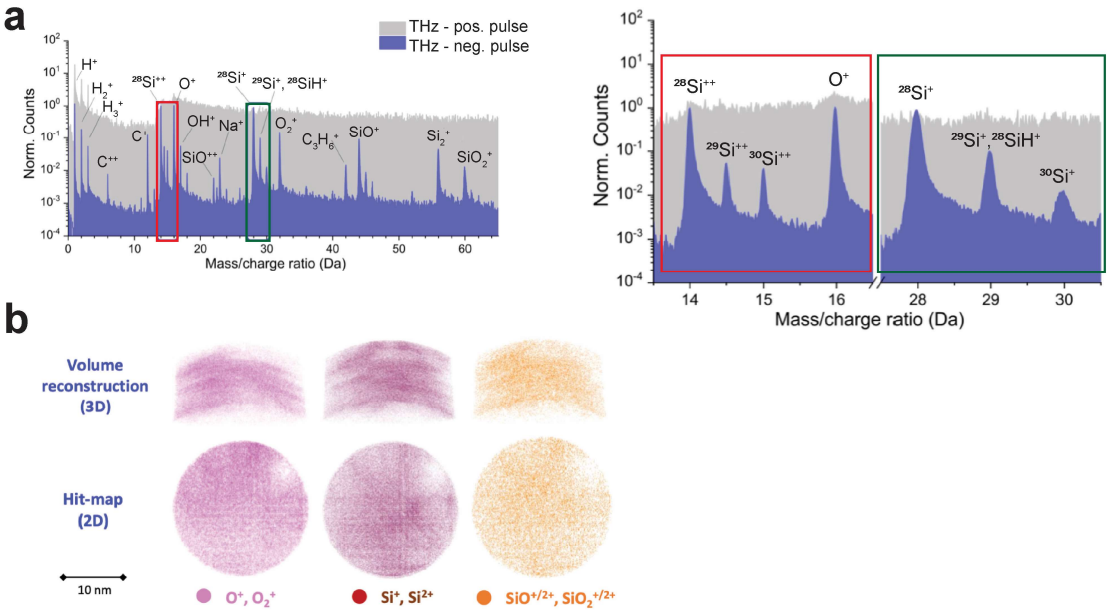


Figure 4.15: ***(a)*** *Mass spectra obtained from analysis of bulk silica using THz-laser assisted APT. The mass spectrum obtained using the positive THz pulse are in grey and using the negative THz pulse in blue.* ***(b)*** *Reconstructed atom maps from the data obtained with the negative THz pulse.*

The results show that negative THz pulses enable evaporation of cations from dielectric specimens, opening for further development of new types of APT instrumentation.

4.4. APT analysis of silica embedded proteins

Proteins were embedded in bulk silica samples by addition of ^{13}C-isotope labelled GFP after pH adjustment, prior to the onset of gelling. Similarly to the bulk silica samples, they were analysed using a LEAP 6000XR instrument equipped with a 257.5 nm deep-UV laser. In samples where the silica synthesis was carried out at pH levels slightly above neutral, it was found that the proteins were concentrated in a distinct region at the top of the glass piece, indicated by a yellow colour, from which lift-outs were made.

The silica matrix in the analyses behave similarly to the empty bulk silica samples analysed with deep-UV laser APT, and ^{13}C is detected at a ten times higher level than ^{12}C, as seen in the mass spectrum in Figure 4.16 a, unambiguously confirming the presence of the proteins within the specimens. In the analysis in Figure 4.16, containing a total of 11.5 million ions, the number of detected ^{13}C atoms is above 600 000, which given the detection efficiency of 52% and the composition of GFP, corresponds to over 1000 proteins in a single measurement. The ^{13}C is found to be clustered in the homogeneous silica matrix and can be highlighted using iso-concentration surfaces with thresholds up to 50 atomic % depending on the voxel size of the 3D grid. Regions can be found where ^{13}C clusters can be isolated and the number of detected ions suspected to be of organic origin is in good agreement with the expected number from GFP. The protein structure contains 1134 carbon atoms, and the ROI in Figure 4.16 c contains 470 ^{13}C. Including other organic originating ions, the number of detected carbon atoms approaches the expected number of 590 given the detection efficiency of the APT instrument. The shape of the ^{13}C cluster also resembles somewhat the known barrel shaped structure of GFP with the dimensions 2 x 4 nm [147][148][149]. However, in most ^{13}C rich regions of the APT data, distortions such as surface diffusion are observed, which are related to the electrostatic field or specimen temperature.

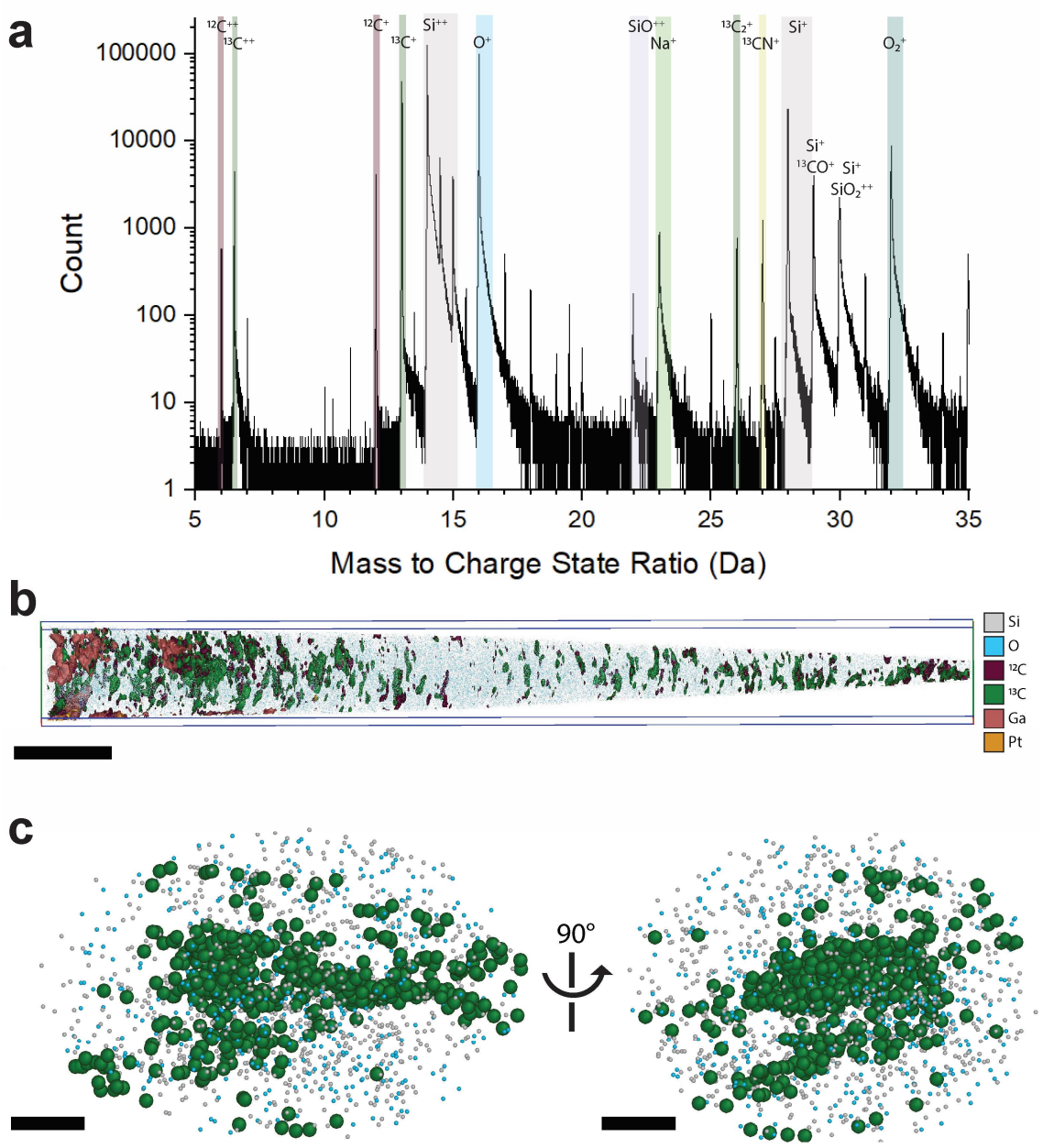


Figure 4.16: ***(a)*** *Mass spectrum obtained from APT analysis of ^{13}C-labelled GFP embedded in silica. Identity of major peaks are labelled. At 29 and 30 Da, overlaps are observed, with both ion species noted.* ***(b)*** *Reconstructed atom map of APT analysis in (a). Silicon and oxygen shown as dots. ^{12}C, ^{13}C, Ga, and Pt shown as iso-concentration surface set to 2, 20, 5, and 2 atomic %, respectively. Scale bar: 50 nm.* ***(c)*** *"spherical" ROI with dimensions 5x4x7 nm from the atom map in (b), isolating ^{13}C cluster which can be identified as a single GFP molecule. Scale bars: 1 nm.*

While previous studies of proteins using APT have detected the organic components as molecular fragment ions, such as CO_2^+ at 44 Da and CNH_2^+ at 28 Da [102], the organic matter here is mainly detected as elementary ^{13}C. Some molecular fragment ions of carbon are also detected, namely $^{13}C_2$, $^{13}C_3$, and $^{13}C_4$ in low amounts. These are

confirmed to be correlated with atomic ^{13}C by radial distribution function (RDF) analysis, as seen in Figure 4.17. Given the molecular structure of the protein, nitrogen and oxygen are expected at roughly 25 and 30 atomic % of carbon, respectively. Nitrogen in the first charge state overlaps with the most abundant isotope of Si^{++} in the mass spectrum, but no deviation from the naturally occurring isotopic distribution of Si is observed in the second charge state. N^{++} is only detected in very low amounts. The signal at 27 Da can be identified as ^{13}CN but is not strongly correlated with ^{13}C in the RDF. The detected oxygen at 16 and 32 Da is not correlated with carbon and consequently attributed to the silica matrix. A signal is detected at 29 Da which cannot only be attributed to Si due to the number of ions being larger than what would be expected given the naturally occurring isotopic distribution. This signal could also be identified as $^{13}CO^{+}$, but it is not correlated with ^{13}C in the RDF. As the isotopic labelling of proteins is imperfect, ^{12}C is detected correlated with ^{13}C, at up to 10 at. % of ^{13}C.

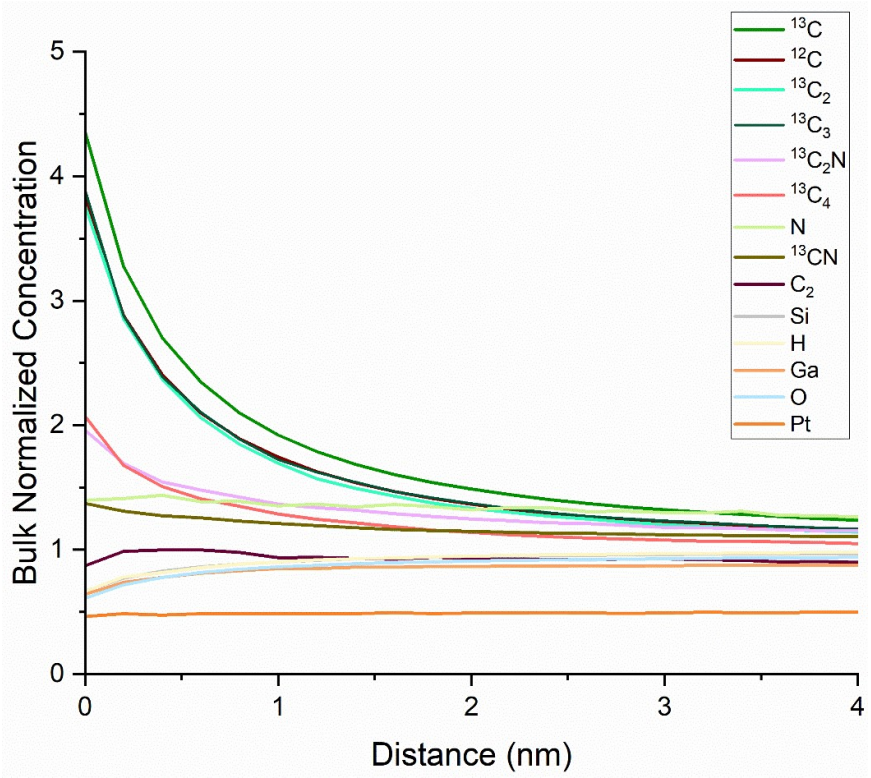


Figure 4.17: Radial Distribution Function analysis of ^{13}C showing bulk normalized concentration of ion species above 0.5 atomic % of ^{13}C.

Table 2: The atomic % relative to ^{13}C for detected ion species found to be correlated with ^{13}C in the RDF analysis.

Ion type	^{12}C	$^{13}C_2$	$^{13}C_3$	$^{13}C_2N$	$^{13}C_4$	N	^{13}CN
At. % of ^{13}C	8.1	3.3	2.1	0.6	1.3	0.13	5.0

The protein containing silica specimens were studied over a range of LPEs, and it was found that the detected amount of ^{13}C decreased with lower pulse energies, as shown in Figure 4.18 c. This is indicative of preferential evaporation of organic material when the voltage and consequently electrostatic field is increased to maintain the evaporation rate as the heating effect of the laser pulses decrease. At higher LPEs, when more of the ^{13}C is detected, it is however observed in the reconstructions that the ions are in layers, following the estimated hemispherical shape of the specimen, clearly seen in Figure 4.18 a. This effect can be attributed to surface diffusion of the carbon atoms caused by the heating from pulse laser irradiation. If the evaporation field is lower of the organic matter than the silica matrix, this can also contribute to aberrations in the measurement by flattening the reconstructed shape of the proteins. Due to losses of carbon at lower LPEs, the higher concentration regions which can indicate the proteins are less prominent, and the potential resolution of protein analysis also gets reduced. The choice of LPE for analysis of the silica embedded proteins thus seems to be a trade-off between factors that can negatively influence the obtained data. The high concentration of proteins in the analysed volumes suggests a risk of protein aggregation, which would cause difficulties in properly identifying individual proteins for 3D structure analysis.

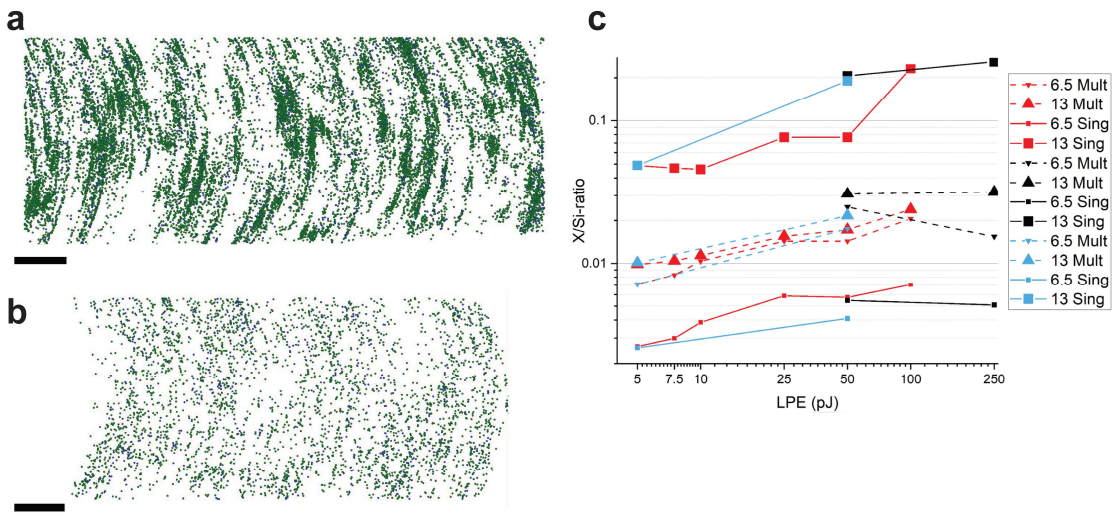


Figure 4.18: ***(a)*** *Segment of reconstructed atom map from APT analysis with laser pulse energy set to 250 pJ. Segment dimensions are 20 x 10 x 50 nm. Scale bar: 5 nm.* ***(b)*** *Segment of reconstructed atom map from APT analysis with laser pulse energy set to 10 pJ. Segment dimensions are 20 x 10 x 50 nm. Scale bar: 5 nm.* ***(c)*** *Detected amounts of ^{13}C related ions as singles and multiples relative to Si at different LPEs over several APT analyses.*

Despite not yet overcoming challenges with obtaining individual proteins with the known structure without any distortions in the reconstructed data, the possibility to obtain data from a larger number of proteins within one single measurement is a significant step towards enabling APT as a technique for structural biological purposes.

5. Conclusions

Advanced characterization techniques can be used to obtain insights into the structure of biomaterials at near atomic scale, as demonstrated in this work. As the structure at this scale is the foundation of the eventual functionality of the material, obtained information can be used to design products with desired features. A titanium surface modified with bone-like hydroxyapatite nanoparticles was analysed by TEM and APT following chromium embedding of the surface, revealing the interface between the substrate and nanoparticles. It was found that calcium and phosphorous had diffused into the surface oxide of titanium during the manufacturing process of the material. Gold nanorods were characterized by TEM and the lattice expansion of solid-supported particles was measured by XRD during in-situ irradiation with a NIR-laser, determining the relationship between laser power and temperature of the gold nanorods up until the onset of morphological changes. These findings provide a basis for the use of such solid-supported gold nanorods for photothermal therapeutic purposes, such as antibacterial surfaces. Examination of the oxide on a zirconium nitride multilayer knee implant revealed a thin native oxide layer on top of the as fabricated material was performed. An explant, after two years in clinical use, had a patchy and comparatively thinner oxide in the articulating area compared to a thicker continuous oxide in the non-articulating area. This demonstrates the ability of high-resolution characterization techniques, such as TEM and APT, to obtain knowledge about material's properties and functionality, which can be used in the design of new biomaterials with improved performance.

It was found that gold nanoparticles with a diameter around 30 nm can be analysed with APT after immobilization on a surface and embedding in silica. The multilayered structure of the material makes the successful analysis of the silica film challenging, as the adhesion between the silica and gold nanoparticles is not sufficient and specimens rupture in this weak interface when the voltage is applied. However, the demonstrated strategy can potentially be used to study surface ligands on the nanoparticles in their hydrated state as the silica film is made by a sol-gel process. An attempt was made to study proteins by binding thiol modified streptavidin to the surface immobilized gold nanoparticles and while successful binding was suggested by TEM, no proteins were detected in APT analyses.

Using deep-UV laser assisted APT, specimens prepared from bulk silica were successfully analysed with yields far exceeding the ones obtained with APT systems using longer wavelength lasers. This type of material has previously been challenging to study due to its dielectric nature, porosity, and poor absorption of visible light. Specimens were analysed over a wide range of laser pulse energies, demonstrating that the electrostatic field required to maintain the evaporation rate is lower at higher pulse energies, typical of thermally assisted field evaporation. In the obtained data, significant

contamination from the FIB/SEM specimen preparation are observed in the form of Ga, as well as Pt and C. Low laser pulse energies were successfully used to analyse the silica samples, at which the estimated electrostatic field was more constant with no clear thermal tails in the mass spectrum. Bulk silica samples were also successfully analysed using the negative pulses in a THz laser assisted APT instrument, indicating the possibility to use a new type of instrumentation to study previously challenging materials with APT.

Bulk silica samples containing ^{13}C-isotope labelled green fluorescent protein were also successfully analysed using deep-UV laser assisted APT. Owing to the possibility to study larger volumes of material, analyses of specimens prepared by lift-outs from high protein concentration regions of the sample yielded far larger numbers of proteins within a single measurement than were previously obtained. Isotope labelled proteins made identification of the biomolecules possible without ambiguities caused by carbon contamination. It was observed that the number of detected ions from the proteins depends on the laser pulse energies and that lower LPEs cause losses of organic matter. On the other hand, at higher LPEs, the structure of the proteins was more distorted due to surface diffusion caused by the laser heating the APT specimen.

These findings show that the potential to use silica matrixes formed by sol-gel processes to replace water and obtain samples that allow for studies of materials in the hydrated state at the near-atomic scale using APT is enabled by advancements in instrumentation. This is exemplified by nanostructured surfaces embedded in silica films and proteins embedded in bulk silica material.

5.1. Future perspectives

Based on results from the studies on different biomaterials in this work, several new questions arise for future research. Based on the observations of calcium and phosphorous from synthetic hydroxyapatite nanoparticles integrating with the surface oxide of titanium during material synthesis, it is of interest for future studies to investigate the osseointegration of bone on this type of material. Especially in comparison with previous studies of osseointegration of bone on titanium that has not been modified with nanoHA.

The temperature increase of gold nanorods irradiated with NIR light is demonstrated and can in future work be used on surfaces of materials suitable for implanted medical devices. Such materials should be designed to allow for very localized heating at the surface to eliminate bacterial infections without damaging surrounding areas, with performance evaluated under conditions similar to clinical applications.

Using the insights into oxide formation on ZrN surfaces of the femoral component of a knee implant, the material design can be improved to make implants with reduced risk of mechanical failure.

From the observations of successful bulk silica APT measurements, especially with a deep-UV laser at low pulse energies as well as THz laser assisted, future work to understand the possibility of non-thermal mechanisms of field evaporation is of interest. This could be of use to enable APT studies of new materials and improve the quality of the obtained data by avoiding aberrations in conventional APT analysis. Such advancements can be of special interest for studies of high band gap materials, materials with low thermal conductivity, and biological materials.

While it has been demonstrated in this work that protein can be analysed using deep-UV laser assisted APT to a previously unachieved degree, the process needs to be developed and optimized for the technique to be beneficial for structural biological purposes. The desired protein distribution in the silica should allow the individual molecules to be clearly separated and distinguishable, while still allowing for a high number of proteins to be detected within a single APT measurement. Ideally, the protein distribution should be homogenous throughout the material, so that lift-outs from any region of the sample will contain the biomolecules of interest. The silica synthesis should also be tuned to the best possible extent to ensure proper retention of the protein's native structure while having optimal properties for APT analysis.

Further investigations should explore other proteins, preferably with larger dimensions and characteristic structures that the method can be optimized with regard to. Current outstanding questions in structural biology that APT can contribute to solve include studies of intrinsically disordered or dynamic proteins, with domains that are not resolvable with the data analysis used in cryo-EM methods. Here, APT could fill an important role as the information potentially obtained from every single protein molecule is much larger. The sample preparation technique used could also prove suitable for proteins that do not crystallize for XRD analysis. Transmembrane proteins are often such proteins and are also of importance for pharmaceutical development. Therefore, it would be of interest to attempt to embed such proteins, possibly situated in lipid nanodiscs or vesicles, in silica for APT analysis. Furthermore, the potential of the silica embedding technique for proteins in more physiologically relevant solutions, along with interactions with other proteins or compounds are of great interest, especially as such information is more challenging to predict with the current computational methods and more training data is required.

As larger datasets are obtained, including information from many protein molecules, data analysis becomes increasingly important, and there is potential to use single particle analysis protocols developed for cryo-EM to obtain higher resolution

characterizations. The current reconstruction protocol may need to be adapted or tuned to obtain the correct protein structure given by established techniques to eventually allow for studies of uncharacterized proteins with better confidence. As many proteins of practical interest are not easily isotope-labelled, the field evaporation behaviour of proteins should be studied more carefully to allow for distinguishing organic ions originating from the biomolecules of interest from contamination.

In conclusion, the APT study of proteins is an exciting research area with many interesting questions and significant potential, made possible by advancements in instrumentation.

Acknowledgements

This work has been funded by the Knut and Alice Wallenberg Foundation (KAW) and the European Union under the Horizon Europe EIC Pathfinder Programme (grant agreement 101046651 - MIMOSA).

The greatest of thanks to my supervisor, Martin Andersson, for the possibility to do this work as well as your guidance and encouragement throughout the entire project. I would also like to give my warm thanks to my co-supervisors Mats Hulander and Mattias Thuvander for their support, insight, and interesting discussions. A special thank you also to my examiner Per-Anders Carlsson.

Thank you to everyone in the MA research group throughout the years, my fellow PhD-student colleagues Maja, Annija, and Edvin, for the company and fun times, both in the lab and at conference trips. Thank you to my master students, August, Saieesh, and Eliz, for your contributions to this project, engagement and curiosity.

Thank you to current and past members of the APT user group, for sharing your knowledge and expertise, interesting and fun discussions, and company on conference trips. A special thank you to David Mayweg for great collaboration on the analysis of embedded proteins.

A special thanks to Chalmers Material Analysis Laboratory, CMAL, where the majority of material characterisation was performed, for their hard work with maintaining the lab and the instruments. Thank you to Paraskevas Kontis and Constantinos Hatzoglou at the Norwegian University of Science and Technology (NTNU) in Trondheim and Torben Boll at the Karlsruhe Institute of Technology (KIT) for opportunity for me to visit and carry out APT experiments at their facilities.

Thank you to everyone in the MIMOSA project for fruitful collaborations and interesting discussions, Matteo De Tullio and Angela Vella at the Groupe Physique de Materialux at the University of Rouen, as well as Giovanni Novi Inverardi, Francesco Carnovale, Tommaso Morresi at FBK-ECT* in Trento.

A warm thank you to all my colleagues at Applied Chemistry, for making the division such a great place to work at. The friendly and helpful atmosphere, and all the breaks in the lunchroom have made these years much more enjoyable.

Finally, I would like to thank all my friends and family for their support.

References

1. Ratner BD, Zhang G. 1.1.2 - A History of Biomaterials. In: Wagner WR, Sakiyama-Elbert SE, Zhang G, Yaszemski MJBTBS (Fourth E, editors. Academic Press; 2020. p. 21–34.
2. Kremers HM, Larson DR, Crowson CS, Kremers WK, Washington RE, Steiner CA, et al. Prevalence of total hip and knee replacement in the United States. JBJS. 2015;97(17):1386–97.
3. Høiby N, Bjarnsholt T, Givskov M, Molin S, Ciofu O. Antibiotic resistance of bacterial biofilms. Int J Antimicrob Agents. 2010;35(4):322–32.
4. Murray CJL, Ikuta KS, Sharara F, Swetschinski L, Aguilar GR, Gray A, et al. Global burden of bacterial antimicrobial resistance in 2019: a systematic analysis. Lancet. 2022;399(10325):629–55.
5. Crick F. Central Dogma of Molecular Biology. Nature. 1970;227:561–3.
6. Kelly TF, Nishikawa O, Panitz JA, Prosa TJ. Prospects for nanobiology with atom-probe tomography. MRS Bull. 2009;34(10):744–9.
7. De Geuser F, Gault B. Metrology of small particles and solute clusters by atom probe tomography. Acta Mater [Internet]. 2020;188:406–15.
8. Gault B, Chiaramonti A, Cojocaru-Mirédin O, Stender P, Dubosq R, Freysoldt C, et al. Atom probe tomography. Nat Rev Methods Prim. 2021;1(1).
9. Vert M, Doi Y, Hellwich KH, Hess M, Hodge P, Kubisa P, et al. Terminology for biorelated polymers and applications (IUPAC Recommendations 2012). 2012;84(2):377–410.
10. Sastri VR. Introduction. In: Sastri VR, editor. Plastics in Medical Devices. Third Edit. Oxford: William Andrew Publishing; 2022. p. 1–11.
11. Stewart PS, Bjarnsholt T. Risk factors for chronic biofilm-related infection associated with implanted medical devices. Clin Microbiol Infect. 2020;26(8):1034–8.
12. Kenney C, Dick S, Lea J, Liu J, Ebraheim NA. A systematic review of the causes of failure of Revision Total Hip Arthroplasty. J Orthop. 2019;16(5):393–5.
13. Zimmerli W. Clinical presentation and treatment of orthopaedic implant-associated infection. J Intern Med. 2014;276(2):111–9.
14. Branemark PI. Osseointegration and its experimental background. J Prosthet Dent. 1983 Sep 1;50(3):399–410.
15. Tambasco De Oliveira P, Nanci A. Nanotexturing of titanium-based surfaces upregulates expression of bone sialoprotein and osteopontin by cultured osteogenic cells. Biomaterials. 2004;25(3):403–13.

16. Meirelles L, Arvidsson A, Andersson M, Kjellin P, Albrektsson T, Wennerberg A. Nano hydroxyapatite structures influence early bone formation. J Biomed Mater Res Part A. 2008 Nov 1;87A(2):299–307.

17. Junqueira LC, Carneiro J. Basic Histology, Text & Atlas. 10th ed. Foltin J, Lebowitz H, Boyle PJ, editors. McGraw-Hill Companies; 2003.

18. Schönweger F, Sprecher CM, Milz S, Dommann-Scherrer C, Meier C, Dommann A, et al. New insights into osteointegration and delamination from a multidisciplinary investigation of a failed hydroxyapatite-coated hip joint replacement. Materials (Basel). 2020;13(21):1–17.

19. Graziani G, Berni M, Gambardella A, De Carolis M, Maltarello MC, Boi M, et al. Fabrication and characterization of biomimetic hydroxyapatite thin films for bone implants by direct ablation of a biogenic source. Mater Sci Eng C. 2019;99(June 2018):853–62.

20. Huang X, Jain PK, El-Sayed IH, El-Sayed MA. Plasmonic photothermal therapy (PPTT) using gold nanoparticles. Lasers Med Sci. 2008;23:217–28.

21. Weissleder R. A clearer vision for in vivo imaging. Nat Biotechnol. 2001;19(4):316–7.

22. Evans JT, Walker RW, Evans JP, Blom AW, Sayers A, Whitehouse MR. How long does a knee replacement last? A systematic review and meta-analysis of case series and national registry reports with more than 15 years of follow-up. Lancet. 2019 Feb 16;393(10172):655–63.

23. Peter T, Thomas W, Gabriele R, Burkhard S, Marc T. Influence of Surface Coating on Metal Ion Release: Evaluation in Patients With Metal Allergy. Orthopedics. 2016 May 1;39(3):S24–30.

24. Reyna ALP, Fritz B, Schwiesau J, Schilling C, Summer B, Thomas P, et al. Metal ion release barrier function and biotribological evaluation of a zirconium nitride multilayer coated knee implant under highly demanding activities wear simulation. J Biomech. 2018;79:88–96.

25. Puente Reyna AL, Lützner J, Altermann B, Grupp TM. Analysis of the In Vivo Oxidation and Integrity of a Zirconium Nitride Multilayer Coated Knee Implant and Possible Effect of Oxidation on the Implant-Cement-Bone Interface Fixation Strength. Int Case Reports J. 2023;3(1):1–16.

26. Cui W, Cheng J, Liu Z. Bio-tribocorrosion behavior of a nanocrystalline TiZrN coating on biomedical titanium alloy. Surf Coatings Technol. 2019;369:79–86.

27. Marth JD. A unified vision of the building blocks of life. Nat Cell Biol. 2008;10(9):1015.

28. Milo R. What is the total number of protein molecules per cell volume? A call to rethink some published values. Bioessays. 2013;35(12):1050–5.

29. Branden CI, Tooze J. Introduction to protein structure. Garland Science; 2012.

30. Brooks-Bartlett JC, Garman EF. The nobel science: One hundred years of crystallography. Interdiscip Sci Rev. 2015;40(3):244–64.

31. Chapman HN, Fromme P, Barty A, White TA, Kirian RA, Aquila A, et al. Femtosecond X-ray protein nanocrystallography. Nature. 2011;470(7332):73–8.

32. Drenth J. Principles of Protein X-Ray Crystallography. Springer New York; 2007. (SpringerLink: Springer e-Books).

33. Henzler-Wildman K, Kern D. Dynamic personalities of proteins. Nature. 2007;450(7172):964–72.

34. Wüthrich K. Protein structure determination in solution by nuclear magnetic resonance spectroscopy. Science (80-). 1989;243(4887):45–50.

35. Patching SG. NMR-active nuclei for biological and biomedical applications. J Diagnostic Imaging Ther. 2016;3(1):7–48.

36. Callaway E. The revolution will not be crystallized: a new method sweeps through structural biology. Nature. 2015;525(7568):172–4.

37. Jumper J, Evans R, Pritzel A, Green T, Figurnov M, Ronneberger O, et al. Highly accurate protein structure prediction with AlphaFold. Nature. 2021;596(7873):583–9.

38. Abramson J, Adler J, Dunger J, Evans R, Green T, Pritzel A, et al. Accurate structure prediction of biomolecular interactions with AlphaFold 3. Nature. 2024;630(8016):493–500.

39. Lundstrom K. Structural genomics for membrane proteins. Cell Mol Life Sci. 2006;63(22):2597–607.

40. Kermani AA. A guide to membrane protein X-ray crystallography. FEBS J. 2021;288(20):5788–804.

41. Günsel U, Hagn F. Lipid Nanodiscs for High-Resolution NMR Studies of Membrane Proteins. Chem Rev. 2022 May 25;122(10):9395–421.

42. Hagn F, Nasr ML, Wagner G. Assembly of phospholipid nanodiscs of controlled size for structural studies of membrane proteins by NMR. Nat Protoc. 2018;13(1):79–98.

43. Thonghin N, Kargas V, Clews J, Ford RC. Cryo-electron microscopy of membrane proteins. Methods. 2018;147:176–86.

44. Autzen HE, Julius D, Cheng Y. Membrane mimetic systems in CryoEM: keeping membrane proteins in their native environment. Curr Opin Struct Biol. 2019;58:259–68.

45. Ealias AM, Saravanakumar MP. A review on the classification, characterisation, synthesis of nanoparticles and their application. IOP Conf Ser Mater Sci Eng. 2017;263(3).

46. Montanarella F, Kovalenko M V. Three Millennia of Nanocrystals. ACS Nano.

2022 Apr 26;16(4):5085–102.

47. Herizchi R, Abbasi E, Milani M, Akbarzadeh A. Current methods for synthesis of gold nanoparticles. Artif Cells, Nanomedicine Biotechnol. 2016;44(2):596–602.

48. Kumar D, Meenan BJ, Mutreja I, D'Sa R, Dixon D. Controlling the size and size distribution of gold nanoparticles: A design of experiment study. Int J Nanosci. 2012;11(2).

49. Zhao P, Li N, Astruc D. State of the art in gold nanoparticle synthesis. Coord Chem Rev. 2013;257(3–4):638–65.

50. Personick ML, Langille MR, Zhang J, Mirkin CA. Shape control of gold nanoparticles by silver underpotential deposition. Nano Lett. 2011;11(8):3394–8.

51. Faraday M. X. The Bakerian Lecture.—Experimental relations of gold (and other metals) to light. Philos Trans R Soc London. 1857;(147):145–81.

52. Amendola V, Pilot R, Frasconi M, Maragò OM, Iatì MA. Surface plasmon resonance in gold nanoparticles: a review. J Phys Condens Matter. 2017;29(20):203002.

53. Jain PK, Huang X, El-Sayed IH, El-Sayed MA. Noble metals on the nanoscale: optical and photothermal properties and some applications in imaging, sensing, biology, and medicine. Acc Chem Res. 2008;41(12):1578–86.

54. Huang X, Neretina S, El-Sayed MA. Gold Nanorods: From Synthesis and Properties to Biological and Biomedical Applications. Adv Mater. 2009 Dec 28;21(48):4880–910.

55. Scarabelli L, Sánchez-Iglesias A, Pérez-Juste J, Liz-Marzán LM. A "Tips and Tricks" Practical Guide to the Synthesis of Gold Nanorods. J Phys Chem Lett. 2015 Nov 5;6(21):4270–9.

56. Hsieh S, Chao WJ, Hsieh CW. Improved performance of aminopropylsilatrane over aminopropyltriethoxysilane as an adhesive film for anchoring gold nanoparticles on silicon surfaces. J Nanosci Nanotechnol. 2009;9(5):2894–901.

57. Chen WH, Tseng YT, Hsieh S, Liu WC, Hsieh CW, Wu CW, et al. Silanization of solid surfaces via mercaptopropylsilatrane: A new approach of constructing gold colloid monolayers. RSC Adv. 2014;4(87):46527–35.

58. Dobrovolskaia MA, McNeil SE. Immunological properties of engineered nanomaterials: An introduction. Handb Immunol Prop Eng Nanomater Second Ed. 2016;1:1–24.

59. Mendes BB, Conniot J, Avital A, Yao D, Jiang X, Zhou X, et al. Nanodelivery of nucleic acids. Nat Rev Methods Prim. 2022;2(1).

60. Ferrari E. Gold nanoparticle-based plasmonic biosensors. Biosensors. 2023;13(3):411.

61. Huang X, El-Sayed IH, Qian W, El-Sayed MA. Cancer cell imaging and photothermal therapy in the near-infrared region by using gold nanorods. J Am Chem Soc. 2006;128(6):2115–20.

62. Zharov VP, Mercer KE, Galitovskaya EN, Smeltzer MS. Photothermal nanotherapeutics and nanodiagnostics for selective killing of bacteria targeted with gold nanoparticles. Biophys J. 2006;90(2):619–27.

63. Hou X, Zaks T, Langer R, Dong Y. Lipid nanoparticles for mRNA delivery. Nat Rev Mater. 2021;6(12):1078–94.

64. Westas E, Gillstedt M, Lönn-Stensrud J, Bruzell E, Andersson M. Biofilm formation on nanostructured hydroxyapatite-coated titanium. J Biomed Mater Res - Part A. 2014;102(4):1063–70.

65. LeGeros RZ. Calcium phosphate-based osteoinductive materials. Chem Rev. 2008;108(11):4742–53.

66. Suchanek W, Yoshimura M. Processing and properties of hydroxyapatite-based biomaterials for use as hard tissue replacement implants. J Mater Res. 1998;13(1):94–117.

67. Yang W, Wang L, Mettenbrink EM, Deangelis PL, Wilhelm S. Nanoparticle Toxicology. Annu Rev Pharmacol Toxicol. 2021;61:269–89.

68. Sukhanova A, Bozrova S, Sokolov P, Berestovoy M, Karaulov A, Nabiev I. Dependence of nanoparticle toxicity on their physical and chemical properties. Nanoscale Res Lett. 2018;13:1–21.

69. Knoll M, Ruska E. Das elektronenmikroskop. Zeitschrift für Phys. 1932;78:318–39.

70. Ruska E. The development of the electron microscope and of electron microscopy. Rev Mod Phys. 1987;59(3):627.

71. Williams DB, Carter CB. Tranmission Electron Microscopy. Second edi. New York: Springer Science+Business Media; 2009.

72. Goldstein JI, Newbury DE, Michael JR, Ritchie NWM, Scott JHJ, Joy DC. Scanning Electron Microscopy and X-Ray Microanalysis. Fourth edi. New York: Springer Science+Business Media; 2018.

73. T J Shaffner, R D Van Veld. “Charging” effects in the scanning electron microscope. J Phys E [Internet]. 1971;4(9):633.

74. Giannuzzi LA, Stevie FA. Introduction to Focused Ion Beams: Instrumentation, Theory, Techniques and Practice. First Edit. New York: Springer Science+Business Media; 2005.

75. Giannuzzi LA, Stevie FA. A review of focused ion beam milling techniques for TEM specimen preparation. Micron. 1999;30(3):197–204.

76. Lefebvre-Ulrikson W, Vurpillot F, Sauvage X. Atom Probe Tomography: Put

Theory Into Practice. Edition 1st, editor. Academic Press; 2016.

77. Müller EW. Das Feldionenmikroskop. Zeitschrift für Phys. 1951;131(1):136–42.

78. Melmed AJ. Recollections of Erwin Müller's laboratory: the development of FIM (1951–1956). Appl Surf Sci. 1996;94–95:17–25.

79. Müller EW. Resolution of the Atomic Structure of a Metal Surface by the Field Ion Microscope. J Appl Phys. 1956 May 1;27(5):474–6.

80. Kelly TF, Miller MK. Atom probe tomography. Rev Sci Instrum. 2007 Mar 30;78(3):31101.

81. Tsong TT. Field ion image formation. Surf Sci. 1978 Jan 1;70(1):211–33.

82. Wada M. On the thermally activated field evaporation of surface atoms. Surf Sci. 1984;145(2):451–65.

83. Kingham DR. The post-ionization of field evaporated ions: A theoretical explanation of multiple charge states. Surf Sci. 1982;116(2):273–301.

84. Hatzoglou C, Rouland S, Radiguet B, Etienne A, Costa G Da, Sauvage X, et al. Preferential Evaporation in Atom Probe Tomography: An Analytical Approach. Microsc Microanal. 2020;26(4):689–98.

85. Gault B, Saksena A, Sauvage X, Bagot P, Aota LS, Arlt J, et al. Towards Establishing Best Practice in the Analysis of Hydrogen and Deuterium by Atom Probe Tomography. Microsc Microanal. 2024 Sep 3;ozae081.

86. Sundell G, Thuvander M, Andrén HO. Hydrogen analysis in APT: Methods to control adsorption and dissociation of H2. Ultramicroscopy. 2013;132:285–9.

87. Ulfig R, Lenz D, Groth G, Bunton JH, Martin I, Prosa TJ, et al. New Product Announcement – LEAP 6000XR, New Applications, New Performance. Microsc Microanal. 2022/07/22. 2022;28(S1):3190–1.

88. Chiaramonti AN, Miaja-Avila L, Caplins BW, Blanchard PT, Diercks DR, Gorman BP, et al. Field Ion Emission in an Atom Probe Microscope Triggered by Femtosecond-Pulsed Coherent Extreme Ultraviolet Light. Microsc Microanal. 2020 Apr 1;26(2):258–66.

89. Vella A, Houard J, Arnoldi L, Tang M, Boudant M, Ayoub A, et al. High-resolution terahertz-driven atom probe tomography. Sci Adv. 2021;7(7):eabd7259.

90. Deconihout B, Gerard P, Bouet M, Bostel A. Improvement of the detection efficiency of channel plate electron multiplier for atom probe application. Appl Surf Sci. 1996;94:422–7.

91. Jagutzki O, Cerezo A, Czasch A, Dorner R, Hattas M, Huang M, et al. Multiple hit readout of a microchannel plate detector with a three-layer delay-line anode. IEEE Trans Nucl Sci. 2002;49(5):2477–83.

92. Miller MK. Atom probe tomography and the local electrode atom probe. Vol. 10, Microscopy and Microanalysis. 2004. 150–151 p.

93. Larson DJ, Prosa TJ, Ulfig RM, Geiser BP, Kelly TF. Local Electrode Atom Probe Tomography. Local Electrode Atom Probe Tomography. New York: Springer Science+Business Media; 2013.

94. Melmed AJ. The art and science and other aspects of making sharp tips. J Vac Sci Technol B Microelectron Nanom Struct. 1991;9(2):601.

95. Thompson K, Lawrence D, Larson DJ, Olson JD, Kelly TF, Gorman B. In situ site-specific specimen preparation for atom probe tomography. Ultramicroscopy. 2007;107(2–3):131–9.

96. McCarroll IE, Bagot PAJ, Devaraj A, Perea DE, Cairney JM. New frontiers in atom probe tomography: a review of research enabled by cryo and/or vacuum transfer systems. Mater Today Adv. 2020;7:100090.

97. Perea DE, Gerstl SSA, Chin J, Hirschi B, Evans JE. An environmental transfer hub for multimodal atom probe tomography. Adv Struct Chem Imaging. 2017;3(1).

98. Grandfield K, Micheletti C, Deering J, Arcuri G, Tang T, Langelier B. Atom probe tomography for biomaterials and biomineralization. Acta Biomater. 2022 Aug 1;148:44–60.

99. Perea DE, Liu J, Bartrand J, Dicken Q, Thevuthasan ST, Browning ND, et al. Atom probe tomographic mapping directly reveals the atomic distribution of phosphorus in resin embedded ferritin. Sci Rep. 2016;6(October 2015):1–9.

100. Qiu S, Zheng C, Garg V, Chen Y, Gervinskas G, Li J, et al. Three-Dimensional Chemical Mapping of a Single Protein in the Hydrated State with Atom Probe Tomography. Anal Chem. 2020;92(7):5168–77.

101. Rusitzka KAK, Stephenson LT, Szczepaniak A, Gremer L, Raabe D, Willbold D, et al. A near atomic-scale view at the composition of amyloid-beta fibrils by atom probe tomography. Sci Rep. 2018;8(1):1–10.

102. Sundell G, Hulander M, Pihl A, Andersson M. Atom Probe Tomography for 3D Structural and Chemical Analysis of Individual Proteins. Small. 2019;15(24):1–6.

103. Hans Wedepohl K. The composition of the continental crust. Geochim Cosmochim Acta. 1995;59(7):1217–32.

104. Anderson RS, Anderson SP. Geomorphology: The Mechanics and Chemistry of Landscapes. Cambridge University Press; 2010. 187 p.

105. Götze J, Pan Y, Müller A. Mineralogy and mineral chemistry of quartz: A review. Mineral Mag. 2021/09/28. 2021;85(5):639–64.

106. Flörke OW, Graetsch HA, Brunk F, Benda L, Paschen S, Bergna HE, et al. Silica. In: Ullmann's Encyclopedia of Industrial Chemistry. 2008.

107. Elliott SR. The structure of amorphous materials. In: Properties and Applications of Amorphous Materials. Dordrecht: Springer; 2001. p. 1–11.

108. Brunauer S, Emmett PH, Teller E. Adsorption of Gases in Multimolecular Layers. J AmChemSoc. 1938;60(2):309–19.

109. Barrett EP, Joyner LG, Halenda PP. The Determination of Pore Volume and Area Distributions in Porous Substances. I. Computations from Nitrogen Isotherms. J Am Chem Soc. 1951;73(1):373–80.

110. Horvath G, Kawazoe K. Method for calclualtion effective pore size distribution in molecular sieve carbon. J Chem Eng Japan. 1983;16(12):470.

111. Stöber W, Fink A, Bohn E. Controlled Growth of Monodisperse Silica Spheres in the Micron Size Range. J Colloid Interface Sci. 1968;26(1):62–9.

112. Bogush GH, Tracy MA, Zukoski CF. Preparation of monodisperse silica particles: Control of size and mass fraction. J Non Cryst Solids. 1988;104(1):95–106.

113. Chang SY, Ring TA. Map of gel times for three phase region tetraethoxysilane, ethanol and water. J Non Cryst Solids. 1992;147–148:56–61.

114. Belton DJ, Deschaume O, Perry CC. An overview of the fundamentals of the chemistry of silica with relevance to biosilicification and technological advances. FEBS J. 2012;279(10):1710–20.

115. Brinker CJ, Hurd AJ, Schunk PR, Frye GC, Ashley CS. Review of sol-gel thin film formation. J Non Cryst Solids. 1992;147–148(C):424–36.

116. Sumper M, Brunner E. Learning from diatoms: Nature's tools for the production of nanostructured silica. Adv Funct Mater. 2006;16(1):17–26.

117. Nassif N, Livage J. From diatoms to silica-based biohybrids. Chem Soc Rev. 2011;40(2):849–59.

118. Ravindra R, Zhao S, Gies H, Winter R. Protein encapsulation in mesoporous silicate: The effects of confinement on protein stability, hydration, and volumetric properties. J Am Chem Soc. 2004;126(39):12224–5.

119. Ellerby LM, Nishida CR, Nishida F, Yamanaka SA, Dunn B, Valentine JS, et al. Encapsulation of proteins in transparent porous silicate glasses prepared by the sol-gel method. Science (80-). 1992;255(5048):1113–5.

120. Bhatia RB, Brinker CJ, Gupta AK, Singh AK. Aqueous sol-gel process for protein encapsulation. Chem Mater. 2000;12(8):2434–41.

121. Liu DM, Chen IW. Encapsulation of protein molecules in transparent porous silica matrices via an aqueous colloidal sol-gel process. Acta Mater. 1999;47(18):4535–44.

122. Novi Inverardi G, Carnovale F, Petrolli L, Taioli S, Lattanzi G. Silica In Silico: A Molecular Dynamics Characterization of the Early Stages of Protein

Embedding for Atom Probe Tomography. Biophysica. 2023;3(2):276–87.

123. Park YK, Park S. Directing close-packing of midnanosized gold nanoparticles at a water/hexane interface. Chem Mater. 2008;20(6):2388–93.

124. Bunton JH, Olson JD, Lenz DR, Kelly TF. Advances in pulsed-laser atom probe: Instrument and specimen design for optimum performance. Microsc Microanal. 2007;13(6):418–27.

125. Gault B, Müller M, La Fontaine A, Moody MP, Shariq A, Cerezo A, et al. Influence of surface migration on the spatial resolution of pulsed laser atom probe tomography. J Appl Phys. 2010 Aug 17;108(4):44904.

126. Mosiman DS, Chen YS, Yang L, Hawkett B, Ringer SP, Mariñas BJ, et al. Atom Probe Tomography of Encapsulated Hydroxyapatite Nanoparticles. Small Methods. 2021;5(2):1–8.

127. Langelier B, Wang X, Grandfield K. Atomic scale chemical tomography of human bone. Sci Rep. 2017;7(1):39958.

128. Glimcher M. Bone: Nature of the Calcium Phosphate Crystals and Cellular, Structural, and Physical Chemical Mechanisms in Their Formation. Rev Mineral Geochemistry. 2006 Jan 1;64(1):223–82.

129. Landi E, Celotti G, Logroscino G, Tampieri A. Carbonated hydroxyapatite as bone substitute. J Eur Ceram Soc. 2003;23(15):2931–7.

130. Karlsson J, Sundell G, Thuvander M, Andersson M. Atomically resolved tissue integration. Nano Lett. 2014;14(8):4220–3.

131. Muneshwar T, Cadien K. Comparing XPS on bare and capped ZrN films grown by plasma enhanced ALD: Effect of ambient oxidation. Appl Surf Sci. 2018;435:367–76.

132. Milošev I, Strehblow HH, Navinšek B. Comparison of TiN, ZrN and CrN hard nitride coatings: Electrochemical and thermal oxidation. Thin Solid Films. 1997;303(1–2):246–54.

133. Amirifar N, Lardé R, Talbot E, Pareige P, Rigutti L, Mancini L, et al. Quantitative analysis of doped/undoped ZnO nanomaterials using laser assisted atom probe tomography: Influence of the analysis parameters. J Appl Phys. 2015;118(21).

134. Devaraj A, Colby R, Hess WP, Perea DE, Thevuthasan S. Role of Photoexcitation and Field Ionization in the Measurement of Accurate Oxide Stoichiometry by Laser-Assisted Atom Probe Tomography. J Phys Chem Lett. 2013 Mar 21;4(6):993–8.

135. Rau JS, Balachandran S, Schneider R, Gumbsch P, Gault B, Greiner C. High diffusivity pathways govern massively enhanced oxidation during tribological sliding. Acta Mater. 2021;221:117353.

136. Stiller K, Viskari L, Sundell G, Liu F, Thuvander M, Andrén HO, et al. Atom

Probe Tomography of Oxide Scales. Oxid Met. 2013;79(3):227–38.

137. Zhang Q, Klein B, Sanford NA, Chiaramonti AN. Comparative Apex Electrostatics of Atom Probe Tomography Specimens. J Electron Mater. 2021;50(6):3022–9.

138. Jun H, Jang K, Jung C, Choi PP. Atom Probe Tomography Investigations of Ag Nanoparticles Embedded in Pulse-Electrodeposited Ni Films. Microsc Microanal. 2021;27(5):1007–16.

139. Vurpillot F, Bostel A, Blavette D. Trajectory overlaps and local magnification in three-dimensional atom probe. Appl Phys Lett. 2000;76(21):3127–9.

140. La Fontaine A, Yen HW, Felfer PJ, Ringer SP, Cairney JM. Atom probe study of chromium oxide spinels formed during intergranular corrosion. Scr Mater. 2015;99:1–4.

141. Kuzuya A, Numajiri K, Kimura M, Komiyama M. Single-Molecule Accommodation of Streptavidin in Nanometer-Scale Wells Formed in DNA Nanostructures. Nucleic Acids Symp Ser. 2008 Sep 1;52(1):681–2.

142. Sing KSW. Reporting physisorption data for gas/solid systems with special reference to the determination of surface area and porosity (Recommendations 1984). Pure Appl Chem. 1985;57(4):603–19.

143. Thommes M, Kaneko K, Neimark A V., Olivier JP, Rodriguez-Reinoso F, Rouquerol J, et al. Physisorption of gases, with special reference to the evaluation of surface area and pore size distribution (IUPAC Technical Report). Pure Appl Chem. 2015;87(9–10):1051–69.

144. Bachhav M, Danoix F, Hannoyer B, Bassat JM, Danoix R. Investigation of O-18 enriched hematite (α-Fe2O 3) by laser assisted atom probe tomography. Int J Mass Spectrom. 2013;335:57–60.

145. Greiwe GH, Balogh Z, Schmitz G. Atom probe tomography of lithium-doped network glasses. Ultramicroscopy. 2014;141:51–5.

146. Arnoldi L, Vella A, Houard J, Deconihout B. Antenna effect in laser assisted atom probe tomography: How the field emitter aspect ratio can enhance atomic scale imaging. Appl Phys Lett. 2012;101(15).

147. Ormö M, Cubitt AB, Kallio K, Gross LA, Tsien RY, Remington SJ. Crystal structure of the Aequorea victoria green fluorescent protein. Science (80-). 1996 Sep 6;273(5280):1392–5.

148. Liu Y, Huynh DT, Yeates TO. A 3.8 Å resolution cryo-EM structure of a small protein bound to an imaging scaffold. Nat Commun. 2019;10(1):1–7.

149. Yang F, Moss LG, Phillips GN. The molecular structure of green fluorescent protein. Nat Biotechnol. 1996;14(10):1246–51.